DISSERTATION

Electrochemical Properties of Anodically Polarized Thin Film Electrodes in Solid Oxide Cells

ausgeführt zum Zwecke der Erlangung des akademischen Grades
eines Doktors der technischen Wissenschaften unter der Leitung von

Univ.-Prof. Dipl.-Phys. Dr. Jürgen Fleig
E164 - Institute of Chemical Technologies and Analytics

eingereicht an der Technischen Universität Wien
Fakultät für Technische Chemie

von

Dipl. Ing. Martin Krammer, BSc.
Mat-Nr.: 01129566

Wien, 31. Januar 2023

Martin Krammer

Funding Acknowledgements:

This work was supported by the European Union's Horizon 2020 research and innovation programme under grant agreement No. 824072 ("Harvestore").

Eidesstattliche Erklärung:

Ich erkläre an Eides statt, dass die vorliegende Arbeit nach den anerkannten Grundsätzen für wissenschaftliche Abhandlungen von mir selbstständig erstellt wurde. Alle verwendeten Hilfsmittel, insbesondere die zugrunde gelegte Literatur, sind in dieser Arbeit genannt und aufgelistet. Die aus den Quellen wörtlich entnommenen Stellen sind als solche kenntlich gemacht. Das Thema dieser Arbeit wurde von mir bisher weder im In- noch Ausland einer Beurteilerin/einem Beurteiler zur Begutachtung in irgendeiner Form als Prüfungsarbeit vorgelegt. Diese Arbeit stimmt mit der von den Begutachterinnen/Begutachtern beurteilten Arbeit überein.

Ich nehme zur Kenntnis, dass die vorgelegte Arbeit mit geeigneten und dem derzeitigen Stand der Technik entsprechenden Mitteln (Plagiat-Erkennungssoftware) elektronisch-technisch überprüft wird. Dies stellt einerseits sicher, dass bei der Erstellung der vorgelegten Arbeit die hohen Qualitätsvorgaben im Rahmen der geltenden Regeln zur Sicherung guter wissenschaftlicher Praxis "Code of Conduct" an der TU Wien eingehalten wurden. Zum anderen werden durch einen Abgleich mit anderen studentischen Abschlussarbeiten Verletzungen meines persönlichen Urheberrechts vermieden.

Martin Krammer

Abstract

In the face of human-induced climate change, major reductions of global greenhouse gas emissions are required to limit global warming in the coming decades. A significant emission reduction will be certainly accompanied with a high share of renewable electricity production. However, power systems relying heavily on renewable electricity production are prone to fluctuating supply on different timelines. Therefore, energy storage and sector coupling may play a key role in future energy systems. Solid oxide electrolysis cells (SOECs) provide promising solutions for both of these purposes as they enable highly efficient production of hydrogen, carbon monoxide or syngas from electrical energy. Although many studies reported promising results regarding the application of SOECs, stability problems and performance deterioration pose major challenges for this technology.

Severe degradation phenomena are often related to the oxygen electrode side of SOECs. There, O_2 may form inside the cell, possibly leading to destructive mechanical stress. In this thesis, the electrochemical behavior of the mixed conducting oxide $La_{0.6}Sr_{0.4}CoO_{3-\delta}$ (LSC) was studied under anodic polarization, resembling the operating conditions of oxygen electrodes in SOECs. For this purpose, thin film LSC electrodes with different microstructures were prepared on yttria-stabilzed zirconia (YSZ) single crystals using pulsed laser deposition (PLD). Impedance spectroscopy measurements of these films were conducted under varying anodic DC bias voltages in synthetic air. In particular, the chemical capacitance of LSC electrodes was investigated, which was obtained from fitting impedance spectra with a suitable equivalent circuit. For dense electrodes and electrodes with open pores, a decrease of the chemical capacitance with increasing electrode overpotential was observed. Such a behavior is expected from defect chemical considerations. However, electrodes with intentionally built-in closed pores exhibit a completely different and unexpected behavior. In this case, a capacitance increase with extremely high peak values in the range of 10^4 F/cm^3 was obtained. It is demonstrated that calculated chemical capacitances deduced from a real gas equation excellently predict this capacitance increase. Thus, it is concluded that the formation of highly pressurized O_2 (in the range of 10^4 bar) in closed pores of LSC electrodes is responsible for the observed chemical capacitance peaks. The presented method may thus be used to detect and quantify the buildup of O_2 gas pressures in closed pores at the oxygen electrode side of SOECs.

This electrochemical method was then used to investigate dense electrodes and electrodes with open pores or cracks following different pre-treatments. While all those LSC electrodes again exhibit a decreasing chemical capacitance with increasing anodic overpotential in their pristine state, annealing for several hours as well as bias voltage treatments were found to induce chemical capacitance peaks. It turned out that both pre-treatments cause the development of closed pores. Several surface sensitive analytical techniques were used to show that Sr segregates to the surface of LSC thin films upon annealing. In addition, it was found that these Sr surface species react with minute traces of sulfur present in high purity measurement gases and form a $SrSO_4$ phase, which closes the initially open pores or cracks. Moreover, transmission electron microscopy measurements revealed that applying high anodic bias voltages of $\geq$750 mV to dense electrodes leads to morphological changes and thus also to closed pores. Hence, closed pores may develop in LSC electrodes due to different degradation phenomena. Upon anodic polarization, highly pressurized O_2 forms in those closed pores, which in turn causes the chemical capacitance increase. Model calculations revealed that the degradation-induced closed porosity of the studied thin films is in the range of 1 %. Hence, analyzing the chemical capacitance of oxygen electrodes in SOECs may provide a tool to identify the development of closed pores and O_2 accumulation therein at an early stage, thus possibly preventing destructive loads.

Finally, the potential application of porous LSC electrodes in rechargeable oxygen ion batteries was exemplified using impedance spectroscopy and galvanostatic cycling. A dense ZrO_2 blocking layer was prepared on top of these electrodes, thus inhibiting oxygen exchange with the measurement atmosphere. Half cell measurements revealed discharge capacities up to 135 mAh/cm^3 with reasonable cycling behavior. In order to gain insights regarding the underlying charge storage mechanisms, measured charge/discharge curves were compared with those reconstructed from chemical capacitance values as well as with model calculations. Thereby, it was found that filling oxygen vacancies is the dominant mechanism at low potentials (*i.e.*, <50 mV vs. 1 bar O_2), whereas O_2 formation in closed pores determines the charging behavior at high potentials. Furthermore, also full oxygen ion batteries consisting of porous LSC cathodes and dense $La_{0.9}Sr_{0.1}CrO_{3-\delta}$ (LSCr) anodes were tested. Cell voltages as high as 1.2 V were obtained, owing to the much lower reducibility of LSCr compared to LSC, and reasonable cycling performance was found.

Kurzfassung

Angesichts des vom Menschen verursachten Klimawandels ist eine erhebliche Verringerung der weltweiten Treibhausgasemissionen erforderlich, um die globale Erwärmung in den kommenden Jahrzenten zu begrenzen. Eine deutliche Emissionsreduktion wird zweifellos mit einem hohen Anteil an erneuerbarer Stromerzeugung einhergehen. Allerdings sind Stromnetze, die in hohem Maße auf der Erzeugung aus erneuerbaren Quellen basieren anfällig für Versorgungsschwankungen. Daher werden Energiespeichertechnologien und der Kopplung verschiedener Sektoren oft eine Schlüsselrolle in zukünftigen Energiesystemen zugeschrieben. Festoxidelektrolysezellen bieten vielversprechende Lösungen für diese beiden Bereiche, da sie eine hocheffiziente Umwandlung von elektrischer Energie in Wasserstoff, Kohlenmonoxid oder Synthesegas ermöglichen. Obwohl in einigen Studien bereits vielversprechende Resultate erzielt wurden, stellen sowohl Stabilitätsprobleme als auch Leistungsverluste noch eine Herausforderung für diese Technologie dar.

Gravierende Degradationsphänomene treten oft auf der Seite der Sauerstoffelektrode in Fextoxidelektrolysezellen auf. Dabei ist es möglich, dass sich O_2 im Inneren der Zelle bildet und es dadurch zu Zerstörungen aufgrund mechanischer Belastungen kommt. In dieser Arbeit wurde das elektrochemische Verhalten des gemischtleitenden Oxids $La_{0.6}Sr_{0.4}CoO_{3-\delta}$ (LSC) unter anodischer Polarisierung untersucht, entsprechend den Betriebsbedingungen von Sauerstoffelektroden in Festoxidelektrolysezellen. Zu diesem Zweck wurden Dünnschichtelektroden mit unterschiedlichen Mikrostrukturen auf Einkristallen aus Yttriumoxid-stabilisiertem Zirkoniumdioxid (YSZ) mittels gepulster Laserdeposition hergestellt. Diese Dünnschichtelektroden wurden mit Hilfe von Impedanzspektroskopie bei variierenden anodischen DC Spannungen in synthetischer Luft charakterisiert. Insbesondere wurde die chemische Kapazität dieser LSC-Elektroden untersucht, welche durch die Analyse der Impedanzspektren anhand eines Äquivalentschaltkreises bestimmt wurde. Dichte Elektroden und Elektroden mit offenen Poren weisen eine Abnahme dieser chemischen Kapazität bei steigender Elektrodenüberspannung auf. Ein solches Verhalten ist aufgrund der defektchemischen Eigenschaften von LSC auch erwartbar. Allerdings stellte sich heraus, dass Elektroden mit bewusst eingebrachten geschlossenen Poren ein völlig anderes und unerwartetes Verhalten zeigen. Dabei wurde ein Kapazitätsanstieg mit Maximalwerten im Bereich von 10^4 F/cm^3 festgestellt. Es wird gezeigt, dass der beobachtete Kapazitätsanstieg sehr gut mit berechneten Kapazitätskurven übereinstimmt, welche mit Hilfe einer Realgasgleichung ermittelt wurden. Daraus wird geschlossen, dass die Bildung von stark verdichtetem O_2 (im Bereich von 10^4 bar) in geschlossenen Poren von LSC-Elektroden für die beobachteten Kapazitätsmaxima verantwortlich ist. Die vorgestellte Methode eignet sich daher zur Detektion und Quantifizierung bei der Entstehung von hohen Sauerstoffdrücken in geschlossenen Poren auf der Sauerstoffelektrodenseite von Festoxidelektrolysezellen.

Diese elektrochemische Methode wurde anschließend eingesetzt, um dichte Elektroden und Elektroden mit offenen Poren oder Rissen nach verschiedenen Vorbehandlungen zu untersuchen. All diese LSC-Elektroden weisen direkt nach ihrer Herstellung eine abnehmende chemische Kapazität bei zunehmender Elektrodenüberspannung auf. Mehrstündiges Tempern oder die Behandlung mit anodischer Gleichspannung ruft jedoch Kapazitätsmaxima hervor. Es zeigte sich, dass beide Vorbehandlungsmethoden die Entwicklung von geschlossenen Poren verursachen. Mit Hilfe verschiedener oberflächensensitiver Analyseverfahren konnte dargelegt werden, dass Sr während des Tempervorgangs an die Oberfläche der LSC-Dünnschichten segregiert. Wie sich herausstellte, reagiert diese Sr-haltige Oberflächenspezies mit geringen Mengen an Schwefelverunreinigungen, die selbst in hochreinen Messgasen vorhanden sind, und bildet eine $SrSO_4$-Phase. Dieses $SrSO_4$ verschließt in weiterer Folge die ursprünglich offenen Poren und Risse. Darüber hinaus ergaben Untersuchungen mittels Transmissionselektronenmikroskopie, dass das Anlegen hoher anodischer Gleichspannungen (≥750 mV) an dichte Elektroden zu morphologischen Veränderungen und dabei auch zu geschlossenen Poren führt. Demnach können sich also geschlossene Poren in LSC-Elektroden aufgrund verschiedener Degradationsphänomene bilden. Unter anodischer Polarisierung entsteht stark verdichtetes O_2 in diesen Poren, was wiederum den Anstieg der chemischen Kapazität verursacht. Modellrechnungen zeigten außerdem, dass die degradationsbedingte geschlossene Porosität der untersuchten dünnen Schichten im Bereich von 1 % liegt. Somit könnte die Analyse der chemischen Kapazität von Sauerstoffelektroden in Festoxidelektrolysezellen zur frühzeitigen Erkennung von Porenentstehung und damit verbundener Anreicherung von O_2 verwendet werden. Dadurch ließen sich möglicherweise mechanische Zerstörungen der Zellen verhindern.

Schließlich wurde das Einsatzpotenzial poröser LSC-Elektroden in wiederaufladbaren Sauerstoff-Ionen-Batterien mit Hilfe von Impedanzspektroskopie und galvanostatischer Zyklierung untersucht. Um den Sauerstoffaustausch mit der Messatmosphäre zu verhindern, wurde eine dichte ZrO_2-Schicht auf diese Elektroden aufgebracht. Halbzellen zeigten ein gutes Zyklierverhalten mit Entladekapazitäten von bis zu 135 mAh/cm^3. Um Erkenntnisse über die zugrundeliegenden Ladungsspeichermechanismen zu gewinnen, wurden gemessene Lade- und Entladekurven mit jenen Kurven verglichen, die auf Modellrechnungen basieren bzw. aus Kapazitätsmessungen ermittelt wurden. Dabei stellte sich heraus, dass bei niedrigen Potentialen (<50 mV vs. 1 bar O_2) das Füllen von Sauerstoffleerstellen der maßgebliche Speichermechanismus ist. Die Bildung von O_2 in geschlossenen Poren bestimmt hingegen

das Ladeverhalten bei hohen Potentialen. Darüber hinaus wurden auch ganze Sauerstoff-Ionen-Batterien, bestehend aus porösen LSC-Kathoden und dichten $La_{0.9}Sr_{0.1}CrO_{3-\delta}$ (LSCr)-Anoden, getestet. Aufgrund der wesentlich geringeren Reduzierbarkeit von LSCr im Vergleich zu LSC wurden dabei Zellspannungen von bis zu 1.2 V erreicht und zudem ein gutes Zyklierverhalten festgestellt.

Contents

1 Introduction

1.1 Motivation

The most recent assessment report of the Intergovernmental Panel on Climate Change (IPCC)[1] elaborates clearly that human-induced climate change has already various adverse impacts on nature and people. These observed effects include for example heat-related human mortality, extinction of species, increased occurrence of food-borne and water-borne diseases, retreat of glaciers, food and water insecurity or coral mortality. Such phenomena have been attributed to human-induced climate change effects such as increases in frequency and intensity of climate and weather extremes, sea level rise, permafrost thaw or ocean warming and ocean acidification.[1]

Global warming exceeding 1.5 °C is expected to cause additional severe risks with possible impacts that cause the release of additional greenhouse gases or may be irreversible, even if global warming is reduced.[1] The need to mitigate global warming is succinctly summarized by the IPCC report[1]: 'The cumulative scientific evidence is unequivocal: climate change is a threat to human well being and planetary health. Any further delay in concerted anticipatory global action on adaptation and mitigation will miss a brief and rapidly closing window of opportunity to secure a livable and sustainable future for all.' Thus, a rapid and drastic reduction of greenhouse gas emissions is required since the remaining carbon budget to limit global warming to 1.5 °C is about the same size as cumulative net CO_2 emissions over the last decade (2010-2019). Even a global warming limit of 2 °C would require immediate and rigorous action as this requires a reduction of net CO_2 emissions by 27 % in 2030 (compared to emissions in 2019). This particularly applies to the energy, industry and transport sectors, which were responsible for 34, 24 and 15 % of the global greenhouse gas emissions in 2019, respectively.[2] In order to achieve significant emission reductions, it requires major transitions to zero- or low-emission technologies in these sectors. Such a transition of the energy sector will certainly include a high share of renewable electricity production from wind and solar power. Consequently, an increased coupling between the energy sector and other sectors via electrification of various applications would further reduce emissions. However, power systems with high shares from renewable sources suffer from fluctuating supply on various timelines (on the minute, hourly, overnight and seasonal scale).[3–7] In this regard, hydrogen as energy carrier may play an important role in terms of energy storage and additional sector coupling.[3–5,7–9]

Solid oxide electrolysis cells (SOECs) may have a significant impact for both energy storage and sector coupling purposes as they enable highly efficient production of hydrogen (H_2), carbon monoxide (CO) or syngas (H_2 and CO) from electrical energy.[10–13] When using electrical energy from renewable sources, H_2 and/or CO from SOECs may enable zero- or low-emission pathways for steelmaking, in the chemical industry for ammonia and methanol production or for the aviation, maritime and heavy-duty vehicle transport sectors by means of synthetic fuel production.[7,14] The produced H_2 may also be used for storage purposes in the energy sector to cope with supply and demand issues. Combining SOECs with solid oxide fuel cells (SOFCs) results in high electricity-to-hydrogen-to-electricity round-trip efficiencies up to about 44 % (assumung 10 % energy loss by compressing hydrogen for storage purposes[15]).[11,16] Compared to polymer electrolyte membrane or alkaline electrolysis, solid oxide electrolysis is the only technology enabling CO or syngas production and exhibits the highest conversion efficiency. Furthermore, SOECs can be operated reversibly, *i.e.* in the fuel cell mode.[11,17] Consequently, solid oxide electrolysis is a very promising technology which has the potential to play a key role in the development of zero- or low-emission technologies for various sectors.

1.2 Working principle of solid oxide electrolysis cells

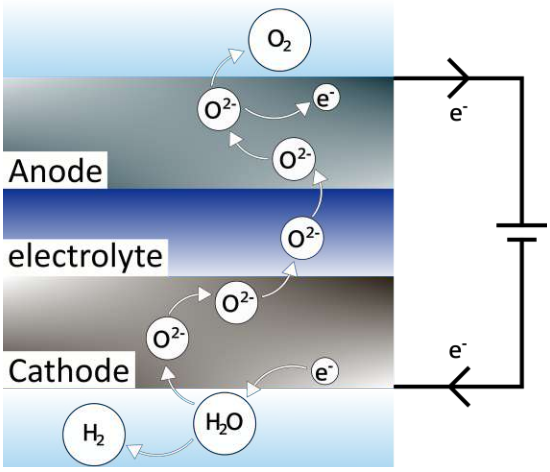

FIGURE 1.1: Working principle of a solid oxide electrolysis cell.

The sketch in Figure 1.1 illustrates the working principle for hydrogen production as well as the main parts [*i.e.*, oxygen electrode (anode), fuel electrode (cathode) and electrolyte] of a solid oxide electrolysis cell (SOEC). At the fuel electrode, water steam is reduced to hydrogen and oxygen ions:

$$2\,H_2O + 4\,e^- \longrightarrow 2\,H_2 + 2\,O^{2-} \quad . \tag{1.1}$$

The oxygen ions get incorporated into the fuel electrode and transported through the electrolyte to the oxygen electrode. There, the oxidation reaction takes place:

$$2\,O^{2-} \longrightarrow O_2 + 4\,e^- \quad , \tag{1.2}$$

thus resulting in the following overall net reaction:

$$2\,H_2O \longrightarrow 2\,H_2 + O_2 \quad . \tag{1.3}$$

Moreover, SOECs can be used to produce CO from CO_2 or syngas (H_2 and CO) via co-electrolysis of water steam and CO_2 according to the following overall net reaction:

$$H_2O + CO_2 \longrightarrow H_2 + CO + O_2 \quad . \tag{1.4}$$

In this case, also CO_2 gets reduced at the fuel electrode:

$$CO_2 + 2\,e^- \longrightarrow CO + O^{2-} \quad . \tag{1.5}$$

It was shown that co-electrolysis and the production of CH_4 via Fischer-Tropsch synthesis can be realized in a single tubular unit.[13] The reverse reactions of Equations (1.1) to (1.5) correspond to the operation mode of a solid oxide fuel cell (SOFC). In terms of structural design, SOECs can be electrolyte-supported, metal-supported as well as fuel electrode-supported. Several cells are connected in parallel or in series to a stack via a metallic or ceramic interconnect material. High operating temperatures are required to ensure sufficient ionic conductivity of the solid electrolyte and commonly range between 650 and 900 °C.[11,18,19]

1.3 Common materials and degradation phenomena in solid oxide electrolysis cells

The materials used in SOECs are essentially similar to those used in SOFCs. However, due to the inverse operating conditions, degradation phenomena can be quite different. A composite comprised of nickel and yttria-stabilized zirconia (YSZ) is most commonly employed as fuel electrode.[20–22] Nickel is an electronic conductor and is known to be highly active for the hydrogen evolution as well as for the CO_2 reduction reaction.[23] The addition of YSZ limits (but does not prevent) the agglomeration of nickel[24], provides a thermal expansion coefficient closer to that of the YSZ electrolyte[25] and extends the reaction zone of the fuel electrode[23].

However, nickel-based electrodes suffer from various degradation phenomena including Ni depletion and agglomeration[26], impurity contamination (Si,Al) of active sites[27,28] and carbon deposition in the case of co-electrolysis or electrolysis of CO_2[29]. Oxides with fluorite- or perovskite-type structures such as Gd-doped CeO_2[30], $La_{0.75}Sr_{0.25}Cr_{0.5}Mn_{0.5}O_3$[31] or $(La,Sr)TiO_3$[32] were also investigated and are considered as fuel electrode materials for SOECs.

Important requirements regarding the electrolyte material for SOEC operation are high conductivity for oxygen ions, chemical stability in oxidizing and reducing conditions, mechanical strength, high gas-tightness, negligible electronic conductivity and chemical as well as mechanical compatibility with the selected electrode materials.[10,33,34] The most common electrolyte material to date is yttria-stabilized zirconia (YSZ), which exhibits reasonable ionic conductivity and chemical stability.[18,34] Scandia-stabilized zirconia (ScSZ) was also suggested as electrolyte material due to its higher ionic conductivity compared to YSZ[18,35], though the major drawback of ScSZ is its high cost[18,19]. Ceria-based electrolytes such as Gd or Sm-doped CeO_2 have also been considered as electrolyte materials as they exhibit a higher ionic conductivity than YSZ[36]. However, the reduction of Ce^{4+} to Ce^{3+} under reducing conditions leads to electronic conduction as well as chemical expansion possibly inducing microcracks.[34,37] Hence, ceria-based electrolytes may be regarded as inapplicable for SOEC operation. The most common use of Gd-doped CeO_2 (GDC) in SOEC applications is as a barrier layer between the electrolyte and the oxygen electrode to prevent secondary phase formation at this interface.[38] $La_{1-x}Sr_xGa_yMg_{1-y}O_{3-\delta}$ (LSGM) related electrolytes also received attention due to their superior ionic conductivity in comparison to YSZ[39]. However, the major drawback of this material is its reactivity with the Ni-based fuel electrode resulting in the formation of lanthanum nickelates.[40]

The most frequently reported and most substantial degradation phenomena regarding the YSZ electrolyte are related to the oxygen electrode/electrolyte interface or to the electrolyte region near to that interface. Specifically, issues of mechanical nature were reported: Post-operation analyses observed the formation of cracks and pores in the YSZ electrolyte[28,41,42], in the oxygen electrode[21] or at the oxygen electrode/electrolyte interface[43–46] as well as delamination of the oxygen electrode from the electrolyte[21,41,42,44,46–49] or the GDC barrier layer[46]. These degradation effects were reported for cells using the perovskite-type oxides $La_{1-x}Sr_xMnO_{3-\delta}$ (LSM)[21,41,42,44,47,50] or $La_{1-x}Sr_xCo_yFe_{1-y}O_{3-\delta}$ (LSCF)[46,48,49], which are the most commonly used oxygen electrode materials in SOECs. Several studies suggested that these degradation phenomena are caused by internal O_2 formation leading to high gas pressures and thus to mechanical stress.[44,46,47,50–52] These oxygen gas pressures p_{O_2} have been estimated via the corresponding overpotential η and Nernst's relation[28,46,51–53] according to

$$p_{O_2} = p_{O_2}^{at} \cdot \exp\left(\frac{4F\eta}{RT}\right) \quad , \tag{1.6}$$

where $p_{O_2}^{at}$ is the ambient oxygen partial pressure, F denotes Faraday's constant, T is the temperature and R stands for the universal gas constant. However, this relation assumes ideal gas behavior since the fugacity coefficient was neglected, which accounts for the occupied space of gas molecules and their interaction under high pressure. Accordingly, neither models nor the exact conditions of O_2-induced degradation are well established.

In this thesis, the electrochemical behavior of $La_{0.6}Sr_{0.4}CoO_{3-\delta}$ (LSC) thin film electrodes was studied under SOEC operating conditions with special emphasis on phenomena associated with internal O_2 gas formation. For this purpose, the chemical capacitance of such electrodes was investigated under varying anodic DC bias voltages. This capacitance can be determined from impedance spectroscopy measurements and is typically used to obtain information about the defect chemistry of mixed ionic and electronic conductors (MIECs) such as LSC.[54–56] In Chapter 2, this method is applied to electrodes with intentionally built-in closed pores. Such electrodes were fabricated on YSZ single crystals via pulsed laser deposition (PLD). Closed porosity was obtained by varying parameters during the PLD process, thus depositing a dense capping film on top of a porous one. Under anodic polarization in synthetic air, a very unusual increase of the chemical capacitance with extremely high peak values was observed. By employing a real gas model this capacitance increase could be ascribed to the formation of highly pressurized O_2 ($\sim 10^4$ bar) in closed pores of the electrode.

Chapter 3 discusses how the electrochemical method introduced in Chapter 2 can be used to investigate the degradation behavior of dense electrodes and electrodes with open pores. It turned out that electrodes with initially open pores exhibit a chemical capacitance peak under anodic polarization after several hours of annealing in synthetic air. Moreover, a similar capacitance behavior was found for dense electrodes after applying high anodic DC voltages of $\geq$750 mV. By employing several surface sensitive analytical techniques and transmission electron microscopy (TEM) it was shown that the formation of closed pores is caused by the annealing as well as the voltage treatment. Under anodic polarization these closed pores get filled with high-pressure O_2, which leads to the chemical capacitance increase. It is demonstrated that model calculations allow to estimate the amount of closed porosity induced by the described degradation phenomena.

In Chapter 4, it is demonstrated how the formation of high-pressure O_2 in closed pores can be utilized in rechargeable oxygen ion batteries. LSC electrodes were prepared with a dense ZrO_2 blocking layer on top to prevent oxygen exchange with the atmosphere. Half cells were investigated by impedance spectroscopy as well as galvanostatic cycling. It was shown that such half cells could be charged and discharged repeatedly without losing significant capacity. By comparing data from galvanostatic cycling with reconstructed charge/discharge curves from chemical capacitance values as well as with model calculations, two different charge storage mechanisms were identified. The first mechanism dominates at rather low potentials (*i.e.*, <0.05 V) and was ascribed to the gradual filling of oxygen vacancies comparable to the Li intercalation in lithium ion batteries. At higher potentials, O_2 gas formation in closed pores comes into play and is responsible for the majority of the electrode's capacity. Furthermore, full oxygen ion batteries were tested with porous LSC cathodes and dense $La_{0.9}Sr_{0.1}CrO_{3-\delta}$ (LSCr) anodes, thereby using the lower reducibility of $La_{1-x}Sr_xCrO_{3-\delta}$ compared to $La_{1-x}Sr_xCoO_{3-\delta}$.

2 Formation and detection of high pressure oxygen in closed pores of $La_{0.6}Sr_{0.4}CoO_{3-\delta}$ solid oxide electrolysis anodes

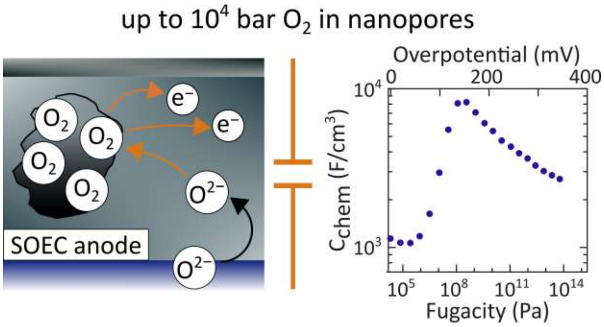

The study presented in this chapter was published in the following article:
Krammer, M.; Schmid, A.; Siebenhofer, M.; Bumberger, A. E.; Herzig, C.; Limbeck, A.; Kubicek, M.; Fleig, J. Formation and Detection of High-Pressure Oxygen in Closed Pores of $La_{0.6}Sr_{0.4}CoO_{3-\delta}$ Solid Oxide Electrolysis Anodes. *ACS Applied Energy Materials* **2022**, *5*, 8324–8335. DOI: 10.1021/acsaem.2c00888.

2.1 Introduction

In literature, it is often suggested that the buildup of high internal gas pressures in closed pores of the electrolyte, the anode or at the anode/electrolyte interface causes mechanical stress and is thus responsible for degradation phenomena in SOECs.[44,46,47,50–52] So far, the values of these gas pressures have been estimated based on the corresponding overpotential.[28,46,51–53] However considering their potentially detrimental effects, a method for direct quantification of these pressures would be highly desirable.

Here, we propose a novel approach to determine these internal gas pressures which includes the analysis of the oxygen electrode's chemical capacitance. The chemical capacitance C_{chem} of an oxide is typically used to obtain information about the defect chemistry[54–56] and is then defined as follows[57,58]

$$C_{chem} = 4F^2V \cdot \left(\frac{\partial \mu_O}{\partial c_O}\right)^{-1} \quad , \tag{2.1}$$

where F denotes the Faraday constant and V the electrode's (bulk) volume. Thus, the chemical capacitance scales with the volume and is determined by the derivative of the oxygen chemical potential μ_O with respect to the concentration of oxygen c_O. This approach can be extended to the gas phase, present in a given volume V via

$$C_{chem} = 16F^2V \cdot \left(\frac{\partial \mu_{O_2}}{\partial c_{O_2}}\right)^{-1} \quad , \tag{2.2}$$

with the chemical potential and concentration of O_2 being μ_{O_2} ($= 2\mu_O$) and c_{O_2} ($= c_O/2$), respectively. Since the derivative depends on the oxygen partial pressure, the chemical capacitance may be used for the determination of internal gas pressures.

This is demonstrated for $La_{0.6}Sr_{0.4}CoO_{3-\delta}$ (LSC) thin film electrodes with closed pores operated upon anodic polarization (corresponding to the SOEC mode). Closed porosity was introduced by depositing a dense capping layer on top of a porous thin film using pulsed laser deposition. Very unusual peaks of the chemical capacitance resulted from impedance measurements, with values exceeding 8000 F/cm^3 at overpotentials higher than 100 mV. It turned out that explaining these capacitive peaks is non-trivial since it requires use of a real gas equation, to deal with the extremely high gas pressure and fugacity values. Our model calculations clearly indicate that the measured anodic peak of the chemical capacitance is caused by highly compressed oxygen in closed pores corresponding to gas pressures in the order of 10^4 bar.

2.2 Experimental

2.2.1 Sample preparation

Yttria-stabilized zirconia (YSZ) single crystals ($5 \times 5 \times 0.5$ mm^3, (100)-oriented, 9.5 mol% Y_2O_3; CrysTec, Germany) were used as electrolyte substrates. For the fabrication of the working and the counter electrodes, LSC thin films were deposited on the YSZ single crystals using pulsed laser deposition (PLD). The corresponding target was prepared via Pecchini synthesis followed by a calcination of the obtained powder for 2 h at 1000 °C. Afterwards the powder was pressed to a pellet by cold isostatic pressing (300-310 MPa) and subsequently sintered in air for 12 h at 1200 °C.

Ablation of the target was done in a vacuum chamber using a KrF excimer laser (Complex Pro 201F, Coherent LaserSystems GmbH & Co. KG, Germany) with a wavelength of 248 nm. In the first step, porous LSC counter electrodes were deposited at an oxygen partial pressure of 0.4 mbar and at a substrate temperature of 450 °C. Earlier studies revealed that electrodes prepared with these parameters exhibit very low polarization resistances due to an increased inner surface area (open porosity).[59,60] Three sample types were then prepared, which differ in microstructure (*i.e.* porosity and surface area) of the working electrode: a) polycrystalline dense, b) porous and c) porous films with a dense capping layer on top (denoted as porous/capped) (see Figure 2.1). Table 2.1 displays the deposition parameters for the three different sample types. The deposition temperatures were measured with a pyrometer which was adjusted to the emissivity of YSZ. For the deposition of dense films, the laser energy was adjusted such that the fluence inside the vacuum chamber was approximately 1.1 J/cm^2. For porous films of similar composition, the laser energy was increased prior to the deposition yielding a fluence of about 1.4 J cm^2. For all different sample types the laser was operated with a pulse repetition rate of 5 Hz. By varying the pulse number, total electrode thicknesses between 40 and 100 nm were obtained (slightly thicker films were used for transmission electron microscopy (TEM) measurements). The film thicknesses were deter-

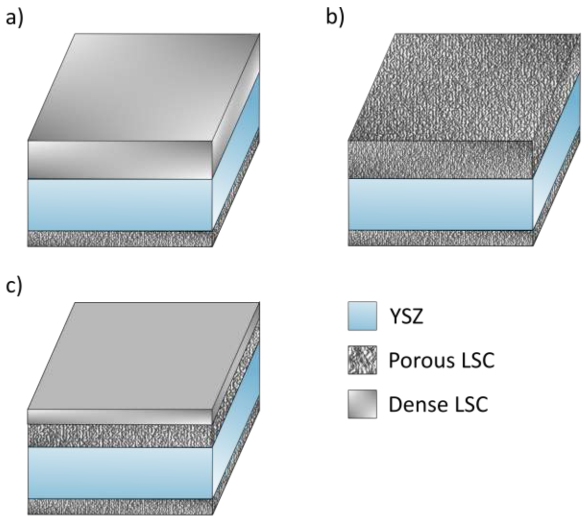

FIGURE 2.1: Sketches of the different sample types investigated in this study: dense (a), porous (b) and porous/capped (c).

TABLE 2.1: Deposition parameters for the five different sample types investigated in this study.

Sample type	Temperature (°C)	Oxygen partial pressure (mbar)	Target-substrate distance (cm)
Dense	600	0.04	6
Porous	450	0.4	5
Porous/capped	450/600	0.4/0.04	5/6

mined using a profilometer (DektakXT, Bruker, USA). The porous part of the porous/capped films accounted for about 80 % of the total electrode thickness. Immediately after the deposition of this porous part, the parameters were changed to those for the dense films in order to deposit a dense capping layer with a thickness in the range of 10 to 20 nm. The deposition parameters of the dense films were chosen based on earlier studies, which confirmed dense packing of columnar grains by TEM cross sections.[61,62] The parameters for the porous films were also taken from a previous study, where the porosity of the respective films was confirmed via TEM bright field cross sections and high-angle annular dark field (HAADF) measurements.[59] After the deposition, all samples were cooled with a rate of 15 °C per minute. The compositions of the films were analyzed by dissolving them in hydrochloric acid and using inductively coupled plasma-mass spectroscopy (ICP-MS). This revealed an average film composition for all sample types of $La_{0.599\pm0.019}Sr_{0.411\pm0.010}Co_{0.990\pm0.016}O_{3-\delta}$.

After the PLD process, microstructuring of the working electrodes was done via photolithography and ion beam etching. For the photolithography process, the samples were coated with 4 x 100 µl of photoresist (ma-N 1420 MicroResist Technology, Germany) using a spincoater, spinning the samples for 1 min every 100 µl. After heating the samples for 5 min at 100 °C in order to evaporate the excess solvent, they were exposed to UV light (350 W, USHIO 350DP Hg, Ushio, Japan) for 1 min through a patterned shadow mask to obtain circular microelectrodes with a diameter of 250 µm. The non-illuminated parts of the photoresist were removed with a developer solution (ma-D 533/s, MicroResist Technology, Germany). These areas of the LSC films were then removed via ion beam etching (KDC 40, Kaufman & Robinson Inc., USA) using a diffuse Ar plasma operated at 9×10^{-4} mbar Ar with a beam voltage of 500 V and a beam current of 10 mA. Finally, the remaining photoresist was carefully removed with a clean room wipe, which was soaked in ethanol.

2.2.2 Impedance spectroscopy

Measurements were performed by placing the samples in a closed fused silica apparatus and heating them in a tube furnace to temperatures between 460 °C and 608 °C. The temperature was measured with a type S thermocouple, which was positioned within 1 cm distance to the sample. Electrical contact of the counter electrodes was realised by placing the samples on a platinum mesh. The (working) microelectrodes were contacted by means of platinum-rhodium needles using a microscope camera. Impedance measurements with DC bias voltages from 0 to 440 mV were carried out using an Alpha-A High Performance Frequency Analyzer with an Electrochemical Test Station POT/GAL 30 V/2 A (both: Novocontrol Technologies GmbH & Co. KG, Germany). An alternating root-mean-square voltage of 10 mV was employed and impedance spectra were measured in the frequency range of 10^6 to 10^{-2} Hz with 5 data points per decade. DC voltages and currents were also measured with the Electrochemical Test Station. All measurements were performed in synthetic air (99.999 %, Messer Austria GmbH, Austria).

2.2.3 X-ray diffraction

The crystal structure of differently prepared LSC thin films was analyzed via X-ray diffraction (XRD) with a Cu radiation source in grazing incidence geometry using an Empyrean X-ray diffractometer (Malvern Panalytical, UK). A parallel beam mirror on the incident beam side and a parallel plate collimator together with a scintillation detector on the diffracted beam side were used for the scans, which were performed at an incidence angle of 2°.

2.2.4 Inductively coupled plasma mass spectrometry

To determine the elemental composition of LSC thin films, an inductively coupled plasma mass spectrometer (ICP-MS) equipped with a quadrupole mass filter and a collision cell (iCAP QC, ThermoFisher Scientific, Germany) was used. Prior to the analysis, a two-step dissolution process was applied according to a previous study[62]: In a first step, the water-soluble species of Sr possibly formed on the surface of pristine LSC samples were dissolved in 5 mL freshly prepared ultra-pure water (BarnsteadTM EasypureTM II, 18.2 MΩcm) for 30 min. In a second step, the remaining LSC thin film was completely dissolved with 100 µL concentrated HCl. The obtained data was processed using Qtegra software (ThermoFisher Scientific, USA). To minimize the influence of polyatomic interferences, the kinetic energy discrimination (KED) mode was used. Herein undesirable molecule ions are suppressed in the collision cell containing a mixture of helium with 7 % hydrogen. Observed signal intensities were normalized using the signal response for the internal standard and finally converted into concentration units by means of external aqueous calibration. Derived Cu signals were constant over each measurement session (less than 5 % relative standard deviation for the whole measurement period, indicating the absence of temporal trends), and no significant difference in Cu-response between samples and calibration standards was observed.

2.2.5 Transmission electron microscopy

Electron-transparent lamellae of about 10 µm length were prepared from additional films of each sample type via standard lift-out techniques with a focused ion beam/scanning electron microscopy (FIB/SEM) system (Scios 2 DualBeam, Thermo Fisher Scientific, Germany), operating with a Ga-ion beam at 30 kV accelerating voltage. Final low-voltage cleaning of the lamellae was conducted at 5 kV and 2 kV. Bright field transmission electron microscopy (BF-TEM) was performed on a 200 kV FEI TECNAI F20.

2.3 Results

2.3.1 Film characterisation

XRD measurements revealed the same crystal structure for LSC films of all different sample types and all reflexes could be assigned to the LSC perovskite phase. In Figure 2.2, all LSC peaks in the different diffractograms were labeled according to the pseudo-cubic structure. For the porous LSC film, only one distinct peak is visible which indicates a low degree of crystallinity.

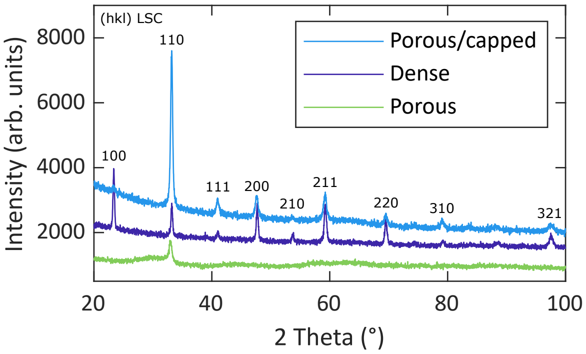

Figure 2.2: XRD diffractograms of dense, porous and porous/capped films measured in the grazing incidence geometry.

In order to investigate the open porosity (*i.e.* the surface area) of the three different sample types, the surface compositions of the LSC thin films were analyzed via ICP-MS measurements in accordance with the approach described in previous works.[59,62,63] Former studies reported a water soluble Sr surface species being present at the surface after the preparation of the thin films.[59,62,64] Thus, by analyzing the amount of this species it is possible to compare the surface area of the different thin films. At first, leaching was done with pure H_2O, particularly dissolving surface species, followed by a subsequent chemical analysis via ICP-MS. Then the films were completely dissolved in hydrochloric acid and an ICP-MS measurement was again conducted to examine the amount of Sr in the bulk (c_{bulk}). In order to compare the data obtained for the three different sample types, the amount of water soluble Sr (c_{surf}) was related to the total amount of Sr in the film ($c_{total} = c_{surf} + c_{bulk}$). The corresponding results are shown in Table 2.2.

We assume that the water soluble Sr species is homogeneously distributed across the surface of all different films. A higher amount of dissolved Sr thus suggests a larger accessible surface area. The poly/dense and the porous/capped films have similar amounts of water soluble surface Sr, which indicates that the top layer of the porous/capped films has a similar morphology as the dense films. Moreover, we can conclude that the majority of the initially open pores in the bottom layer of the porous/capped films becomes closed due to the deposi-

Table 2.2: Ratio of water soluble surface Sr (c_{surf}) to total Sr ($c_{total} = c_{surf} + c_{bulk}$) of LSC thin films

Sample type	c_{surf}/c_{total} (%)
Dense	0.86
Porous	6.75
Porous/capped	1.09

tion of a dense film on top. The amount of water soluble Sr of the porous films is much higher than for the dense and the porous/capped samples. In accordance with a former study[59] we therefore assume open porosity for the porous films leading to a surface area that is 7 to 8 times larger compared to the dense films.

BF-TEM measurements were performed to further analyze the porosity and nanostructure of the different LSC thin films (see Figure 2.3). TEM cross-sections of a dense film reveal dense packed and columnar growth in accordance with an earlier study[61] where the same oxygen partial pressure and substrate temperature was used during deposition. Similar to a previous work on LSC[59], porous films exhibit a rather dense growth in the first approximately 25 nm followed by a porous nanostructure confirming the findings from the ICP-MS measurements. A similar nanostructure is found for the porous/capped film, however above the porous layer the film looks dense. This is again in accordance with the conclusion from the ICP-MS analysis suggesting that the pores get closed due to the deposition of a dense capping layer on top.

2.3.2 Impedance spectroscopy

Figure 2.4 shows exemplary impedance spectra of the different thin film microelectrodes used in this study at various anodic DC bias voltages. The four spectra displayed in each plot are examples of measurement cycles with bias voltages from 0 to 440 mV and steps of 20 mV. All impedance spectra contain a high frequency x-axis intercept which corresponds to the ionic transport resistance of the YSZ electrolyte (R_{YSZ}), in accordance with literature[56,59,65]. This electrolyte resistance is temperature dependent[65], but shows no dependence on the applied bias voltage. R_{YSZ} was determined by extrapolating the electrode-related impedance to the x-axis and this value was also used for subtracting the ohmic overpotential from the applied bias (see Section 2.3.3). The slightly different electrolyte resistance for the spectrum at open circuit conditions in Figure 2.4b compared to the spectra under DC bias voltages of the porous electrode reflects a temperature difference of about 2 °C. In addition, a semi-circular feature at low frequencies is obtained for all spectra. The size of this feature varies depending on the applied DC bias. In agreement with former studies, this low frequency arc is attributed to the oxygen surface exchange resistance R_s and the chemical capacitance C_{chem} of the LSC

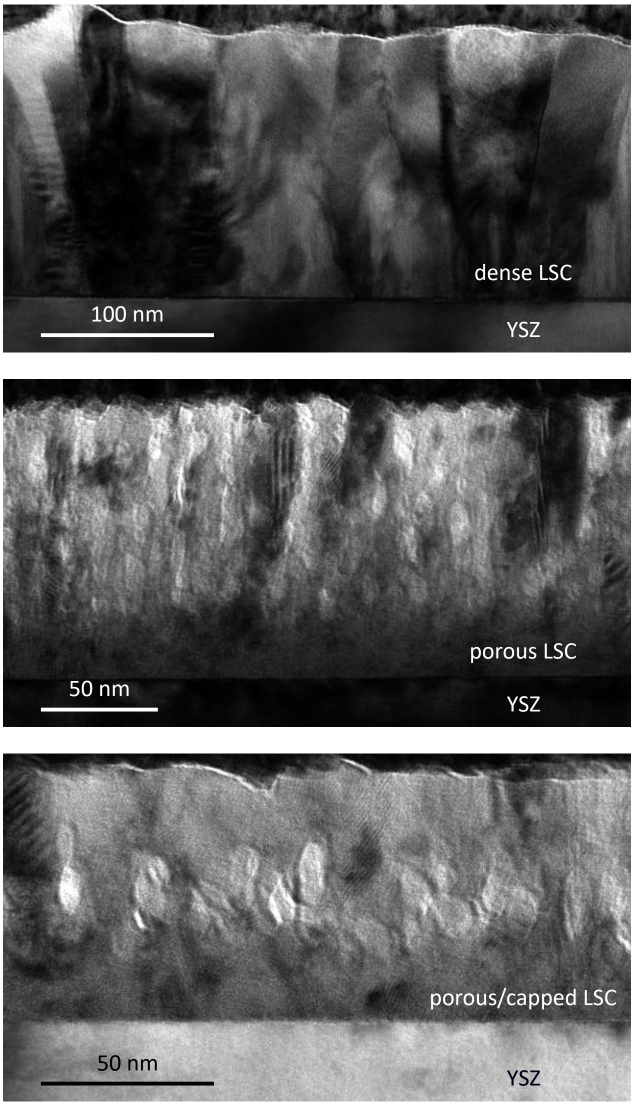

Figure 2.3: BF-TEM cross sections of dense, porous and porous/capped LSC films.

working electrode.[55,56,59,60,62,66] Please note that the oxygen exchange kinetics at open circuit conditions is much faster than for similar bias dependent measurements for LSCF reported in literature[56] ($R_s = 50\,\Omega\mathrm{cm}^2$ at a significantly higher temperature of 700 °C[56]), most probably due to the different preparation parameters and thermal history of the films. It is therefore not surprising that the bias dependence of R_s is also different for the measurements of this study. Moreover, the oxygen exchange rates are strongly affected by defect concentrations (holes, oxygen vacancies)[67,68] and those vary with the applied anodic bias. Finally, also some surface changes at high voltages may occur[69]. Thus, different and also complicated bias dependencies of the differential resistance R_s may result, e.g. the surprising increase and decrease of R_s for the dense film in Figure 2.4a. However, a more detailed analysis of the oxygen surface exchange resistance is beyond the scope of this paper.

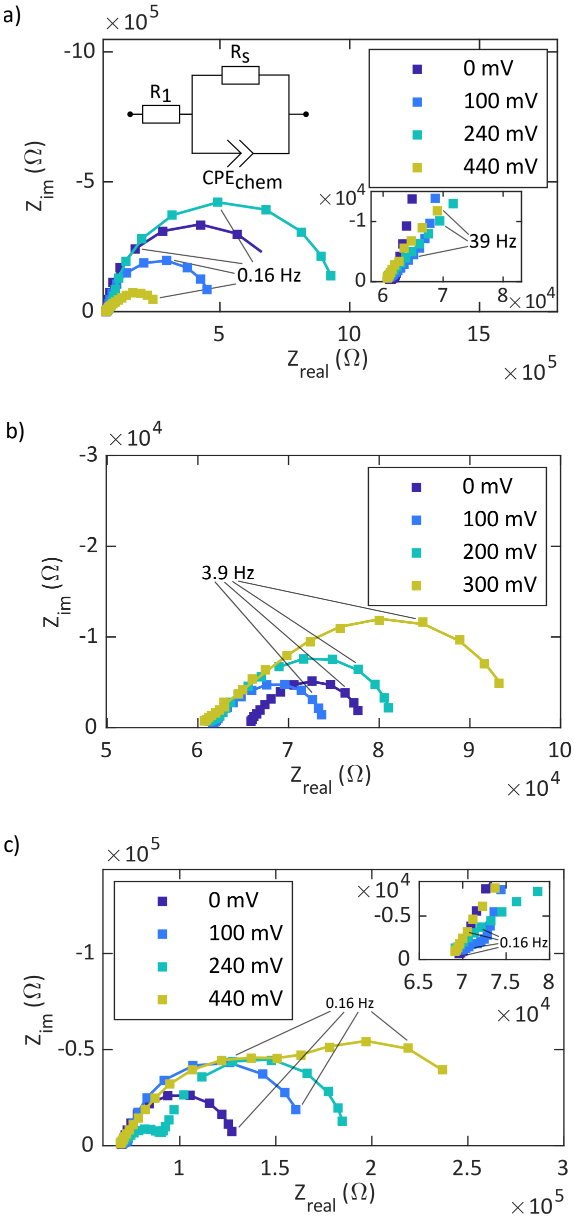

FIGURE 2.4: Impedance spectra of a dense (a), a porous (b) and a porous/capped (c) LSC thin film microelectrode at various anodic DC bias voltages (U_{DC}) measured at 460 °C. Lines represent fits according to the sketched equivalent circuit in (a) (with the exception of spectra at 440 mV in a) and c) and at 300 mV in b), where an additional R/CPE element was used).

Furthermore, additional electrode-related features can be observed at intermediate frequencies. As can be seen in Figure 2.4, those differ between sample types and show a dependency on the applied DC voltage. The shape of these intermediate frequency features varies between arc-like and Warburg-like slopes, though a finite Warburg element alone could never fit the spectra properly. Such intermediate frequency contributions are known from literature data on LSC electrodes[59,61,62] and are usually attributed to processes which are located at the YSZ/LSC interface. The Warburg-like behaviour found here in some cases may also indicate the onset of an oxygen diffusion limitation in LSC. In general, intermediate frequency contributions become larger with increasing DC voltage. Since the focus of this study is on the analysis of the chemical capacitance C_{chem}, we did not further investigate those intermediate frequency features.

C_{chem} was evaluated as long as the low frequency semicircle was clearly separated and accounted for a major part of the respective spectrum, *i.e.* when the polarization resistance of the electrode was determined by the surface exchange reaction. Then, one can assume that a major part of the electrode overpotential is transferred to an oxygen chemical potential change in the electrode.[54,55] When the intermediate and the low frequency contributions were similar in size (e.g. spectra at 440 mV in Figure 2.4a and 2.4c and at 300 mV in Figure 2.4b), the determination of C_{chem} and the corresponding chemical potential from the nominal electrode overpotential (see below) became somewhat doubtful. Therefore, such data were excluded from the following chemical capacitance analysis and a different equivalent circuit was used to describe these spectra (two R/CPE elements and a resistance in series). However, the majority of the obtained spectra allow a reasonable analysis of C_{chem} since the resistance associated with the intermediate frequency feature is considerably smaller than R_s as can be seen in Figure 2.4. The low frequency feature of these spectra was described by a parallel connection of a constant phase element (CPE_{chem}) and a resistance (R_s). A constant phase element with the impedance

$$Z_{CPE} = \frac{1}{(j\omega)^n Q} \tag{2.3}$$

considers the non-ideal behaviour of a capacitance. The CPE parameter Q and the exponent n, which quantifies the deviation from an ideal capacitance, were both obtained from non-linear least square fitting and used to calculate the corresponding capacitance via[70]

$$C_{chem} = (R_s^{1-n} \cdot Q)^{\frac{1}{n}} \quad . \tag{2.4}$$

An additional serial resistance in the equivalent circuit (R_1) considers the above mentioned contributions from the electrolyte (R_{YSZ}) and the intermediate frequency feature (see circuit in Figure 2.4a). Fitting of the spectra to one R/CPE element, considering the low frequency semicircle, and a serial resistance R_1 allowed the most reliable determination of the chemical capacitance, which was the focal point of this paper. Tables 2.3-2.5 in the Appendix show exemplary fitting results for each sample type according to this equivalent circuit.

2.3.3 Chemical capacitance analysis

As shown in a previous study[59], the porous counter electrodes exhibit very low polarisation resistances. Moreover, they have an active area being at least 500 times larger than that of the microelectrodes. Thus, their influence on the measured impedances is negligible and the overpotential of the (working) microelectrodes η_{WE} is determined as follows

$$\eta_{WE} = U_{DC} - \eta_{YSZ} = U_{DC} - I_{DC} \cdot R_{YSZ} \quad , \tag{2.5}$$

where U_{DC} stands for the applied DC bias voltage, I_{DC} is the DC current and η_{YSZ} denotes the ohmic overpotential caused by the finite ionic conductivity of the electrolyte. Figure 2.5 shows the chemical capacitances of the three different sample types, measured at 460 °C in synthetic air. All values were normalized to the respective electrode volume, without correcting for the pore volume of porous and porous/capped electrodes. In the case of porous electrodes, the chemical capacitance could only be evaluated up to $\eta_{WE} \approx 130\,\mathrm{mV}$ due to a strong merging of the intermediate and the low frequency feature.

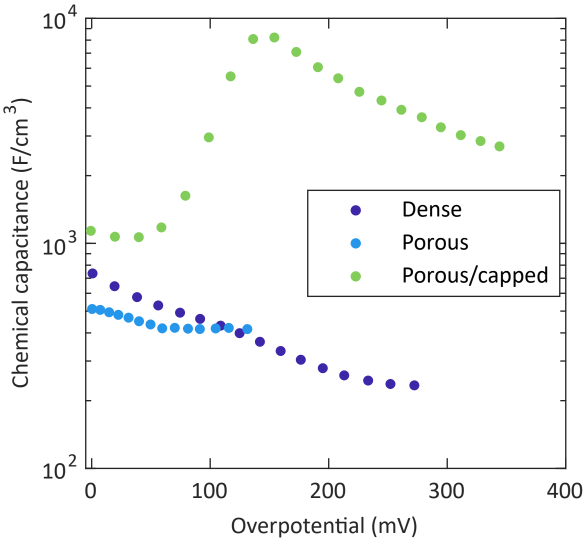

Figure 2.5: Chemical capacitance of a dense, a porous and a porous/capped thin film microelectrode as a function of the electrode overpotential, measured at 460 °C.

While the curves for the dense and the porous films are somewhat similar, a very different and completely unexpected behavior is found for porous/capped electrodes: a capacitance peak with extremely high values. The latter is in the main focus of our study, however, we first discuss the "standard behaviour" of the other films. The chemical capacitances of these films decrease with increasing overpotential and levels off at about 250 and 60 mV, respectively. Such a behaviour is qualitatively consistent with previous studies on LSC and similar mixed conducting oxides upon anodic polarization.[54–56] The corresponding chemical capacitance is caused by the redox reaction of the transition metal cations and its dependence on the oxygen chemical potential. This reaction is accompanied by a change in concentration of oxygen vacancies, which are the minority charge carriers under these conditions. The general behavior of a decreasing chemical capacitance with increasing overpotential can thus be attributed to the decrease of the oxygen vacancy concentration with increasing chemical potential of oxygen.[71–76] As shown in literature[54,55], the concentration of oxygen vacancies and other defects solely depend on the chemical potential of oxygen in the electrode ($\mu_{O_2}^{WE}$) according to:

$$\mu_{O_2}^{WE} = \mu_{O_2}^{0,T} + RT \cdot \ln\left(\frac{p_{O_2}^{at}}{1\,\text{bar}}\right) + 4F\,\eta_{WE} \quad , \tag{2.6}$$

regardless of the respective contribution of the overpotential η_{WE} and the actual atmospheric partial pressure $p_{O_2}^{at}$ (assuming an ideal gas). Here, $\mu_{O_2}^{0,T}$ stands for the chemical potential of oxygen at 1 bar and R, T are the usual notations of the universal gas constant and the temperature, respectively. Hence, applying anodic (*i.e.* positive) overpotential leads to an increase of the chemical potential of oxygen. Validity of Equation (2.6) requires that the transport of charge carriers in the thin film is fast compared to the oxygen surface exchange reaction. In addition, we neglect that a certain part of the electrode overpotential η_{WE} refers to the intermediate frequency feature and does not change $\mu_{O_2}^{WE}$ in the entire electrode. However, as long as the low frequency arc is the dominant feature in the corresponding impedance spectra (see above), Equation (2.6) is a reasonable approximation.

Moreover, one may introduce an effective oxygen partial pressure inside the working electrode $p_{O_2}^{WE,eff}$, as similarly done in former studies[54,55], according to

$$\mu_{O_2}^{WE} = \mu_{O_2}^{0,T} + RT \cdot \ln\left(\frac{p_{O_2}^{WE,eff}}{1\,\text{bar}}\right) \quad , \tag{2.7}$$

and thus we get

$$p_{O_2}^{WE,eff} = p_{O_2}^{at} \cdot \exp\left(\frac{4F\eta_{WE}}{RT}\right) \quad , \tag{2.8}$$

which further illustrates the relation between oxygen partial pressure, the electrode's overpotential and the oxygen chemical potential. However, please note that considering the high anodic overpotentials of the measurements in this study, Equations (2.7) and (2.8) exceed their range of validity, since ideal gas behaviour is assumed. The extension to a real gas is discussed in more detail below.

The overall lower capacitance values for the porous films may be a result of the oxygen exchange reaction taking place along the open pores, which can lead to inactive parts of the film. Apart from not considering the porosity of these films for the volume normalization, this effect contributes to a further reduction of the effective volume. This explanation is also supported by the higher capacitance values of the porous/capped electrodes at low overpotentials. The different slopes of the dense and the porous electrodes may be attributed to strain effects and/or contributions from grain boundaries since porous films show a low degree of crystallinity (see Figure 2.2). A more detailed analysis of the decreasing chemical capacitance is beyond the scope of this study.

The chemical capacitance of porous/capped electrodes also decreases with increasing overpotential, however only up to about 40 mV. At higher overpotentials, these electrodes exhibit a pronounced capacitance peak at about 150 mV with maximum values up to 8200 F/cm^3. Thus, they display a completely different and unexpected behaviour. After reaching this maximum, the chemical capacitance again decreases with increasing overpotentials. This capacitive peak was found for all porous/capped microelectrodes on several different samples at overpotentials of about 150 and 190 mV for temperatures of 460 °C and 608 °C, respectively (see Figure 2.6a). Interestingly, the chemical capacitances for different temperatures show a considerable overlap when plotting against the electrodes' oxygen fugacity (see discussion below) as depicted in Figure 2.6b. Additionally, the peak remains with only little changes if electrodes were cycled stepwise up to about 300 mV and subsequently back to 0 mV. To the best of the authors' knowledge, such an increase of the chemical capacitance under anodic polarization in synthetic air has not been reported in literature yet.

This behaviour cannot be explained by the standard defect chemical interpretation of the chemical capacitance[54,55] and clearly suggests the involvement of an additional species in the redox reaction contributing to the chemical capacitance. Since this phenomenon was only observed for the porous/capped samples, we may conclude that closed porosity is required for the occurrence of this chemical capacitance peak. In the following discussion we show that the appearance of this pronounced capacitance maximum, its temperature dependence and overpotential dependence as well as its absolute value can be excellently explained by high pressure oxygen storage in closed pores, provided that real gas equations instead of ideal gas laws are considered.

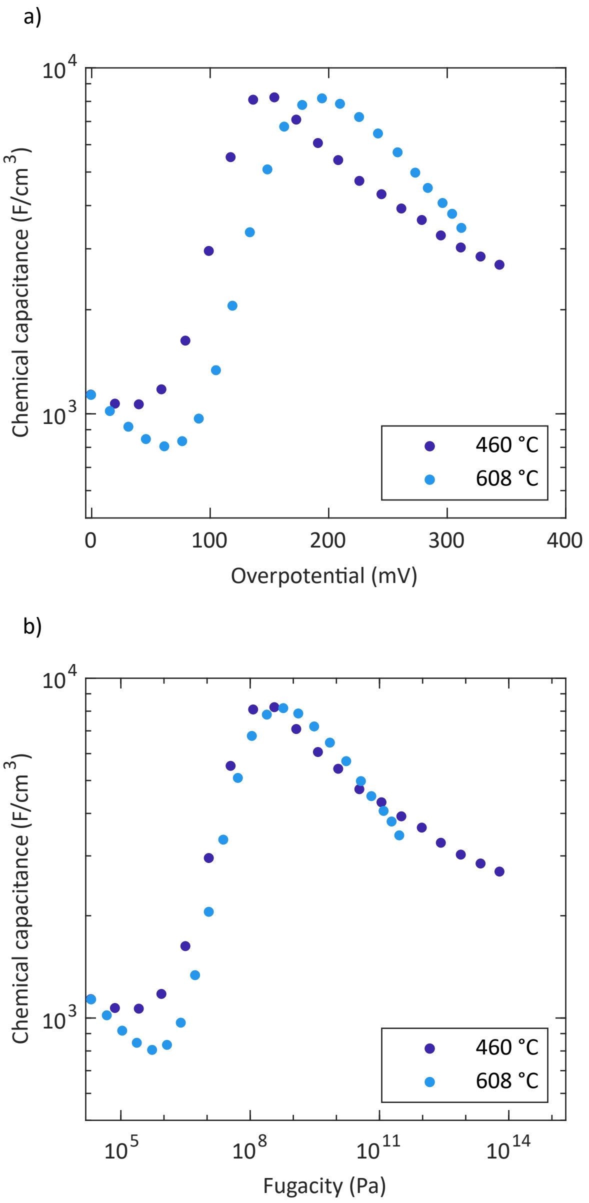

Figure 2.6: Chemical capacitance of porous/capped thin film microelectrodes measured at 460 °C and 608 °C as a function of the electrodes' overpotential (a) and equivalent fugacity (b). Two different samples were used for the different temperatures.

2.4 Mechanistic discussion

A mixed ionic and electronic conducting oxide has the ability to shift its nonstoichiometry, *i.e.* to change δ of $La_{0.6}Sr_{0.4}CoO_{3-\delta}$, upon external drivers such as oxygen partial pressure, temperature or bias voltage. However, as already discussed above, this phenomenon can only explain the baseline of the chemical capacitance curve with decreasing C_{chem} values. Therefore, another redox process has to contribute to the chemical capacitance. Based on the requirement of closed porosity in order to obtain the capacitive peak at anodic overpotentials, we now consider the formation and storage of neutral oxygen gas in closed pores as an additional contribution to C_{chem}. Figure 2.7 depicts this reaction in closed pores of a porous/capped film. Assuming ideal gas behaviour, the corresponding O_2 gas reservoir acts as a chemical capacitor with a capacitance according to

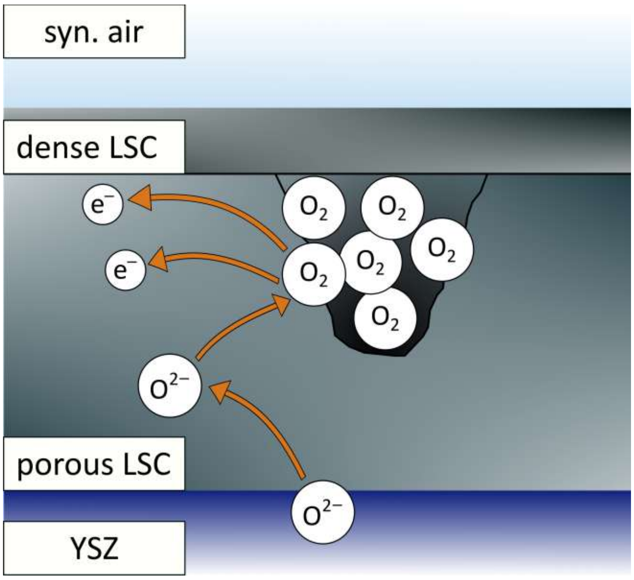

FIGURE 2.7: Sketch of neutral oxygen gas formation and storage in closed pores of a porous/capped film.

$$C_{chem}^{gas,ideal} = 16F^2\lambda V \cdot \left(\frac{\partial\mu_{O_2}}{\partial c_{O_2}}\right)^{-1} = \frac{16F^2\lambda V}{RT} \cdot c_{O_2} = \lambda V \left(\frac{4F}{RT}\right)^2 \cdot p_{O_2}^{pore} \quad , \tag{2.9}$$

with the film porosity λ and the O_2 pressure in closed pores $p_{O_2}^{pore}$. This relation yields a continuous increase of the capacitance with increasing partial pressure or correspondingly, with increasing anodic overpotential (see Figure 2.8). Even though a strong increase was indeed found above 40 mV-60 mV, the measured capacitance curve is not predicted by Equation (2.9). Rather, the capacitance decreased after reaching a maximum value which appeared at overpotentials at about 150 and 190mV for temperatures of 460 °C and 608 °C, respectively. According to Equation (2.8), these overpotentials correspond to high effective internal oxygen partial pressures $p_{O_2}^{WE,eff}$ between 1.5×10^3 and 8×10^3 bar, respectively, and thus to values beyond the limits of ideal gas behaviour. This is even more true for overpotentials far beyond the maximum; 300 mV at 460 °C, for example, results in a nominal pressure of 3.7×10^7 bar. Consequently, we have to consider real gas behaviour. In the following we do this in terms of the Soave-Redlich-Kwong (SRK) equation of state[77] according to

$$p_{O_2}^{pore} = \frac{RT}{V_{O_2} - b} - \frac{a\alpha}{V_{O_2}(V_{O_2} + b)} = \frac{RT}{\frac{1}{c_{O_2}} - b} - \frac{a\alpha}{\frac{1}{c_{O_2}}(\frac{1}{c_{O_2}} + b)} \quad , \tag{2.10}$$

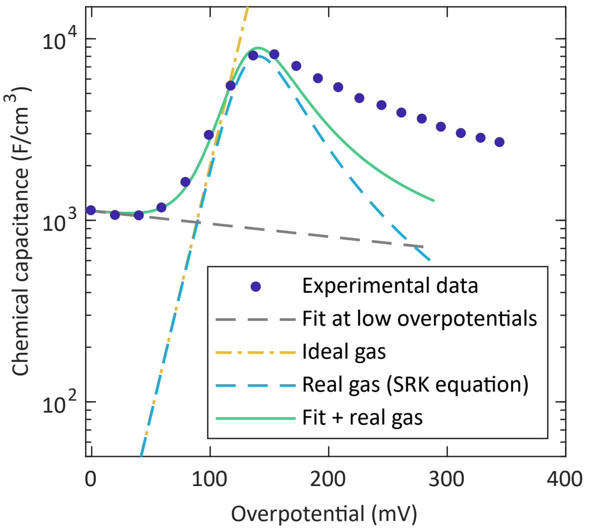

Figure 2.8: Calculated chemical capacitance of an ideal ($C_{chem}^{gas,ideal}$) and a real ($C_{chem}^{gas,real}$) high pressure oxygen gas and experimentally obtained chemical capacitance of a porous/capped electrode at 460 °C as a function of the electrode overpotential. The grey dashed line represents the fit and the corresponding extrapolation of the experimental capacitance values at low overpotentials (C_{chem}^{fit}). Additionally, the green curve shows the sum of this extrapolation and the capacitance of the real gas approach.

$$a = \frac{0.42747 \cdot R^2 T_c^2}{p_c} \quad , \tag{2.11}$$

$$b = \frac{0.08664 \cdot R T_c}{p_c} \quad , \tag{2.12}$$

$$\alpha = (1 + (0.480 + 1.574 \cdot \omega_a - 0.176 \cdot \omega_a^2) \cdot (1 - \sqrt{T/T_c}))^2 \quad , \tag{2.13}$$

with V_{O_2} denoting the molar volume of O_2 and $T_c = 154.6\,\mathrm{K}$ and $p_c = 50.46\,\mathrm{bar}$ being the critical temperature and critical pressure of O_2[78], respectively. The α parameter contains the acentric factor of O_2 $\omega_a = 0.022$, which takes account of the influence of intermolecular forces depending on the orientation of the molecule.[78] The fugacity coefficient φ corresponding to the Soave-Redlich-Kwong (SRK) equation of state can be calculated as follows[77]

$$\varphi = \frac{f_{O_2}}{p_{O_2}^{pore}} = Z - 1 - \ln\left(Z - \frac{b p_{O_2}^{pore}}{RT}\right) - \frac{a}{bRT} \cdot \ln\left(1 + \frac{b p_{O_2}^{pore}}{ZRT}\right) \quad , \tag{2.14}$$

with the fugacity of O_2 f_{O_2} and the compressibility factor Z being

$$Z = \frac{p_{O_2}^{pore}}{c_{O_2} RT} \quad . \tag{2.15}$$

For the calculation of the chemical capacitance of a real gas, it is necessary to consider the fugacity coefficient for the oxygen chemical potential according to

$$\begin{aligned} C^{gas,real}_{chem} = 16F^2\lambda V \cdot \left(\frac{\partial \mu_{O_2}}{\partial c_{O_2}}\right)^{-1} &= 16F^2\lambda V \cdot \left(\frac{\partial\left(\mu^{0,T}_{O_2} + RT\ln\left(\frac{\varphi p^{pore}_{O_2}}{1\,bar}\right)\right)}{\partial c_{O_2}}\right)^{-1} \\ &= \frac{16F^2\lambda V}{RT} \cdot \left(\frac{\partial\left(\ln\left(\frac{\varphi p^{pore}_{O_2}}{1\,bar}\right)\right)}{\partial c_{O_2}}\right)^{-1} \quad . \end{aligned} \tag{2.16}$$

By taking the values for $p^{pore}_{O_2}$ and φ calculated according to Equations (2.10) and (2.14), respectively, $\frac{\partial \mu_{O_2}}{\partial c_{O_2}}$ in Equation (2.16) was determined numerically.

In order to compare the capacitance obtained from this calculation with our experimental data, the overpotential η_{WE} relative to the oxygen partial pressure in synthetic air is related to the fugacity f_{O_2} and the fugacity coefficient φ by

$$\eta_{WE} = \frac{RT}{4F} \cdot \ln\left(\frac{f_{O_2}}{0.21\,\mathrm{bar}}\right) = \frac{RT}{4F} \cdot \ln\left(\frac{\varphi p^{pore}_{O_2}}{0.21\,bar}\right) \quad . \tag{2.17}$$

As a consequence, for high anodic overpotentials, the effective internal oxygen partial pressure $p^{WE,eff}_{O_2}$ defined in Equation (2.8) should be replaced by the effective oxygen fugacity $f^{WE,eff}_{O_2}$ as follows

$$f^{WE,eff}_{O_2} = p^{at}_{O_2} \cdot \exp\left(\frac{4F\eta_{WE}}{RT}\right) \quad . \tag{2.18}$$

Figure 2.8 shows the calculated chemical capacitance of an ideal and a real oxygen gas as well as the experimental values of a porous/capped electrode for a temperature of 460 °C. The overall closed porosity of the porous/capped film (including the dense capping layer) of the calculated curves was the only free parameter in the calculation and was adjusted in order to obtain the best agreement with the experimental data. This yielded a closed porosity of $\lambda = 0.0425$. The chemical capacitance of a real gas thus exhibits an increase with a maximum at a very similar overpotential as the experimentally determined capacitance. Moreover, unlike for the ideal gas approach, the capacitance of the real gas decreases with increasing overpotential, *i.e.* with increasing oxygen concentration, after reaching a maximum at 140.5 mV. The sum of the calculated real gas capacitance and the extrapolation of the defect-related LSC chemical capacitance at low overpotentials agrees rather well with the experimentally obtained capacitance of a porous/capped electrode.

At high overpotentials, the calculated capacitances are lower than the experimental values. This deviation may have several possible reasons including a continuous loss of oxygen e.g. via leaky grain boundaries in the dense top layer or some errors in determining the proper local fugacity due to neglecting any interfacial and/or transport overpotentials. Additionally, the high oxygen pressure may induce redox processes in or near pores which could further contribute to the increased experimental capacitances at high overpotentials, e.g. SrO_2 formation from SrO and O_2. From thermodynamic data[79] the stability limit for the reaction of SrO to SrO_2 would correspond to an overpotential of 67 mV at 445 °C, which is lower than the overpotentials for which deviations from our model are observed. However, for the system in our study it needs to be considered that the thermodynamics of SrO on or in LSC are different than for bulk SrO. We therefore expect a shift of the corresponding stability limit to higher overpotentials at which the reaction could also contribute to the increased chemical capacitance. Further deviations may occur due to particle interactions at extremely high densities.

However, due to the very good agreement of the calculated curve with the experimental data at moderate overpotentials and the fact that the suggested mechanism explains the decrease of the capacitance with increasing overpotential after reaching a maximum, we conclude that the formation of high pressure oxygen gas in closed pores is responsible for the strong capacitance increase upon anodic polarization. Furthermore, calculations based on the presented real gas model yield a shift of the capacitance maximum to higher overpotentials with increasing temperature as observed in our experiments. The calculations based on the real gas model predict a peak shift from 141 mV at 460 °C to 174 mV at 608 °C and the corresponding experiments yield peaks at 154 mV and 194 mV, respectively. As already described above, the chemical capacitance curves measured at 460 °C and 608 °C overlap when they are plotted as a function of the electrodes' oxygen fugacity according to Equation (2.18). This overlap indicates that the storage of highly pressurized O_2, which causes the C_{chem} increase, occurs at particular fugacity values.

As already mentioned above, the capacitance peak was reproducibly found when performing several measurements on one electrode. Besides, no morphological changes were visible in the optical microscope after measurements on porous/capped electrodes at overpotentials >300 mV. This indicates that closed pores were largely not destructed (*i.e.* opened) in our measurements despite (mechanical) gas pressure values in the range of 10^4 bar. Nevertheless, the long term stability of such closed pores upon polarization can still be a serious issue in real SOEC electrodes. Tiny closed pores at interfaces or within electrode particles may be exposed to extremely high true (mechanical) gas pressures of $\sim 10^4$ bar for long times which may cause degradation, e.g. delamination or pore and crack formation.

The existence of this capacitance peak due to closed porosity may also be used as a non-destructive observation tool during cell operation for detecting the presence of closed pores at an early stage in a real SOEC anode. Even if the ratio between closed pore volume to LSC bulk is a factor of 300 lower than in our model electrodes, a shoulder is visible on the defect-related C_{chem} baseline. Moreover, the presented electrochemical method is capable of detecting any high pressure oxygen buildup in closed porosity at the anode side of SOECs, regardless of the location, as the internal oxygen formation is always associated with an increased chemical capacitance. Thus, it should be possible to detect closed pores or cracks (and the development of high pressure oxygen therein) at the anode/electrolyte interface and even in the electrolyte close to that interface. Nevertheless, the kinetics of the associated oxygen exchange reaction is important since $1/(R \cdot C_{chem})$ determines the frequency of the respective feature in the impedance spectrum (R being the resistance of the oxygen production). Therefore, a large exchange resistance R and slow electron transport in the electrolyte might lead to extremely low frequencies $<10^{-3}$ Hz, which may render impedance measurements difficult.

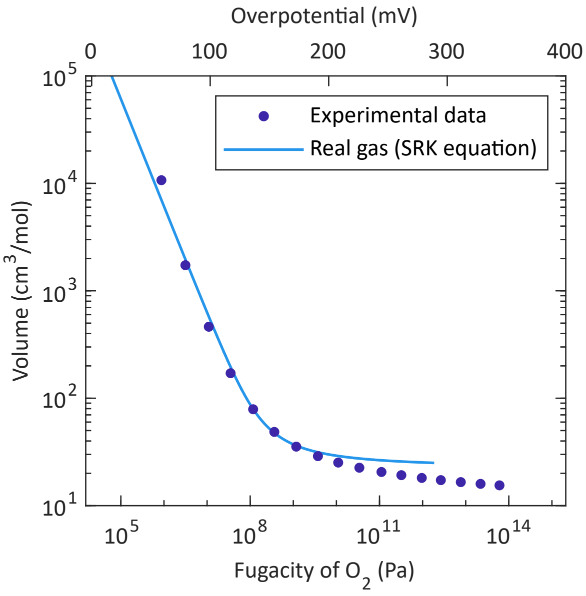

FIGURE 2.9: Molar volume according to the real gas model shown in Equation (2.10) compared to the molar volume V_m calculated from experimental chemical capacitance data shown in Figure 2.8 as a function of the electrode overpotential and the corresponding fugacity.

In addition to the implications of this effect for the oxygen electrode of SOECs, we can also attempt to extract fundamental data of pressurized O_2 at high temperatures that are otherwise hardly accessible. Figure 2.9 displays the oxygen molar volume calculated from a cumulative numerical integration over the peak of the experimental capacitance data shown in Figure 2.8. Subtracting the extrapolation of the fit at low overpotentials (C_{chem}^{fit}) according

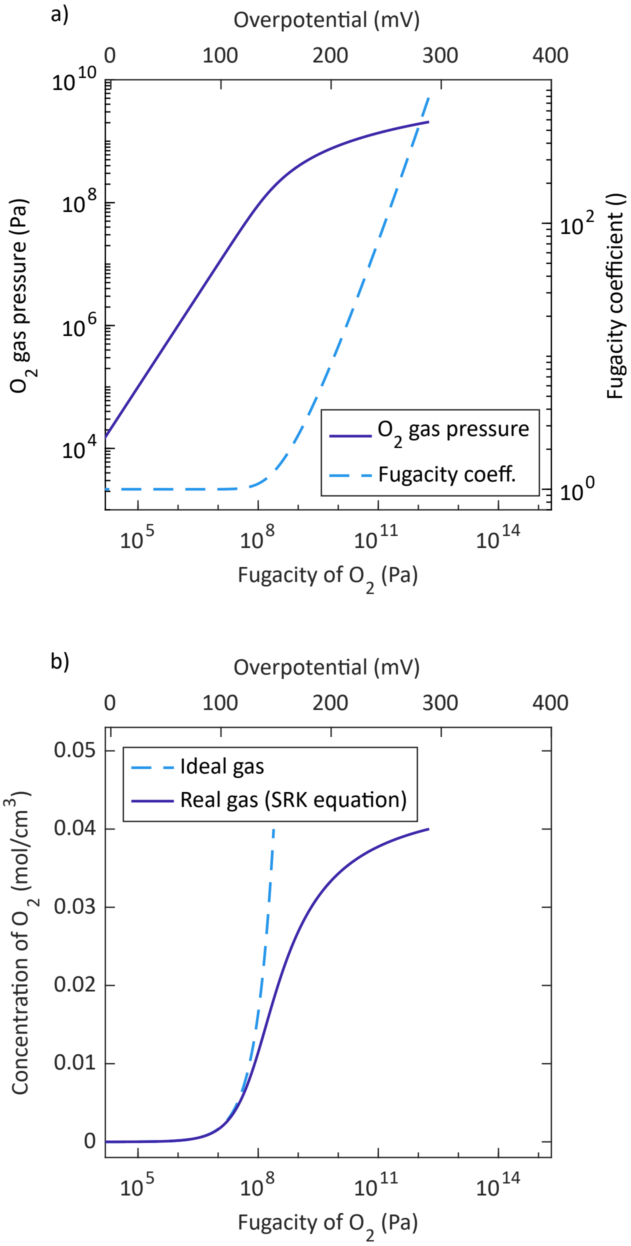

FIGURE 2.10: (a): Oxygen gas pressure p_{O_2} and fugacity coefficient φ obtained from Equations (2.10) and (2.14), respectively. (b): Oxygen concentration c_{O_2} according to the ideal and real gas model, respectively. All quantities are plotted as a function of the fugacity and the corresponding electrode overpotential at 460 °C.

to

$$Q_O = \int_{peak} \frac{C_{chem} - C_{chem}^{fit}}{V} \, d\eta_{WE} \tag{2.19}$$

yields the volume specific charge Q_O of the oxygen gas formation. The corresponding molar volume $V_{O_2}^{exp}$ was calculated as follows:

$$V_{O_2}^{exp} = \frac{4e\lambda N_A}{Q_O} \quad , \tag{2.20}$$

with the Avogadro constant N_A. The oxygen molar volume V_{O_2} obtained from integrating the curve of the real gas model in Figure 2.8 is also displayed. Both curves demonstrate that we may face oxygen molar volumes in the 30 cm^3/mol range. For the purpose of comparison it is worth mentioning that solid oxygen exhibits about 15 cm^3/mol at 10 GPa and room temperature[80].

Figure 2.10a illustrates the deviation of the gas pressure according to the real gas model from the partial pressure calculated via Nernst's equation as shown in Equation (2.8). Here it is clearly demonstrated that at overpotentials higher than approximately 140 mV (equivalent to a fugacity of about 148 MPa) the oxygen gas pressure does not increase exponentially with increasing overpotential (or linearly with the fugacity). In particular, the capacitance maximum obtained for the porous/capped electrode at 460 °C corresponds to a (mechanical) gas pressure of about 2000 bar and thus already deviates from the effective partial pressure $p_{O_2}^{WE,eff}$ according to Nernst's equation as defined in Equation (2.8) which yields 2800 bar and is actually the fugacity f_{O_2} of oxygen (see Equation (2.18)). The difference between gas pressure and fugacity becomes even larger at higher overpotentials (or fugacities) which is further demonstrated by plotting the fugacity coefficient φ (see Figure 2.10a). For overpotentials (fugacities) <130 mV (<10^3 bar) $\varphi \approx 1$ results, indicating ideal gas behaviour. However, at higher overpotentials (fugacities), φ increases drastically which reflects that at these overpotentials, the O_2 gas formation and storage in our LSC films occurs at conditions far beyond ideal gas limitations.

Figure 2.10b displays the oxygen concentration as a function of the fugacity and the corresponding electrode overpotential at 460 °C. The chemical capacitance $C_{chem}^{gas,real}$ is determined by the derivative of the oxygen concentration c_{O_2} with respect to the fugacity $f_{O_2} = \varphi p_{O_2}$ as shown in Equation (2.16). This corresponds to the slope of the concentration curve in Figure 2.10b. Hence, the increasing slope of the concentration curve with a maximum at 140 mV directly reflects the increasing C_{chem} curve and the maximum peak values at similar overpotentials. Furthermore, the decreasing concentration slope at higher overpotentials explains the peak-shaped C_{chem} curve with decreasing values beyond the maximum.

2.5 Conclusion

The chemical capacitance of LSC thin film microelectrodes with different microstructures was analyzed upon varying anodic DC voltages. In the case of dense and porous electrodes (open porosity), the chemical capacitance decreased with increasing overpotential in accordance with literature due to the decrease of the oxygen vacancy concentration. However, porous electrodes with a dense capping layer (closed porosity) exhibited an increase of the chemical capacitance with extremely high peak values $> 8000\,\mathrm{F/cm^3}$ at anodic overpotentials above 100 mV. In addition, it was shown that a higher measurement temperature leads to a shift of the capacitive peak to higher overpotentials.

Since this novel capacitive effect requires closed porosity, we considered the formation of high pressure oxygen in closed pores and calculated the corresponding chemical capacitance according to the Soave-Redlich-Kwong real gas equation. The thus calculated capacitance curve agrees very well with the experimental data at moderate overpotentials. Moreover, the real gas behaviour explains the unexpected decrease of the chemical capacitance with increasing overpotential beyond the maximum despite increasing oxygen concentration in the closed pores. Therefore, we conclude that the formation of high pressure oxygen in closed pores is responsible for the observed peak of the chemical capacitance upon anodic polarization. This capicitive peak was reproducibly found even when measuring one electrode several times, which indicates that closed pores largely withstood gas pressures of $\sim 10^4$ bar.

More specifically the present study shows the following:

- The chemical capacitance of LSC thin film electrodes can be used to observe and quantify oxygen gas pressures in closed pores upon anodic polarization in synthetic air. This capacitive effect can also be of importance for SOEC applications. Whenever some sort of closed porosity occurs in such SOEC anodes or at the anode/electrolyte interface, either due to degradation phenomena or simply because of the configuration of the cell (*i.e.* current collector or interconnect on top of the electrode), high pressure oxygen will form and lead to high mechanical load.

- Analyzing the chemical capacitance of an electrode in SOEC mode could be used for detecting any kind of closed porosity at an early stage and thus may prevent destructive processes due to high pressure buildup. Since even ratios of closed porosity to bulk volume in the order of 10^{-4} should be detectable, this method might be used as a non-destructive measurement tool during SOEC operation.

- The formation of high pressure oxygen in closed pores corresponds to extremely high oxygen densities approaching molar volumes in the 30 cm^3/mol range. The closed pores thus act as kind of nano-vessels which can withstand pressures in the gigapascal range. Accordingly, determining mechanical gas pressures on the anode side of SOECs requires the application of real gas equations and fugacities.
- Closed pores in thin films can act as a chemical oxygen storage with capacitances $> 8000\,\mathrm{F/cm^3}$ or $> 400\,\mathrm{mAh/g/V}$ and thus may be technologically interesting.

2.6 Appendix

Tables 2.3-2.5 show the fitting results of R_s, Q and n according to the equivalent circuit depicted in Figure 4 at different bias voltages U_{DC} for each sample type. For each fitting procedure $n \geq 0.92$, therefore the exponent values of 1/n are sufficiently close to 1 for the calculation of the chemical capacitance C_{chem}.

Table 2.3: Fit parameters of the CPE element for the dense electrode at 460 °C.

U_{DC} (mV)	R_s (Ωcm^2)	Q (mF s^{n-1})	n ()
0	3.37×10^2	3.49×10^{-3}	0.983
20	3.85×10^2	3.07×10^{-3}	0.984
40	3.56×10^2	2.75×10^{-3}	0.984
60	2.94×10^2	2.54×10^{-3}	0.986
80	2.35×10^2	2.37×10^{-3}	0.987
100	1.98×10^2	2.23×10^{-3}	0.987
120	1.78×10^2	2.08×10^{-3}	0.990
140	1.75×10^2	1.93×10^{-3}	0.991
160	1.87×10^2	1.77×10^{-3}	0.993
180	2.17×10^2	1.61×10^{-3}	0.993
200	2.63×10^2	1.47×10^{-3}	0.991
220	3.34×10^2	1.35×10^{-3}	0.990
240	4.26×10^2	1.25×10^{-3}	0.982
260	5.44×10^2	1.18×10^{-3}	0.984
280	6.74×10^2	1.13×10^{-3}	0.981
300	7.95×10^2	1.12×10^{-3}	0.983

Table 2.4: Fit parameters of the CPE element for the porous electrode at 460 °C.

U_{DC} (mV)	R_s (Ωcm^2)	Q (mF s^{n-1})	n ()
0	5.77	1.83×10^{-3}	0.932
20	4.60	1.70×10^{-3}	0.940
40	4.18	1.60×10^{-3}	0.947
60	4.36	1.59×10^{-3}	0.946
80	4.82	1.60×10^{-3}	0.941
100	5.36	1.60×10^{-3}	0.938
120	5.82	1.58×10^{-3}	0.951
140	6.45	1.56×10^{-3}	0.949
160	7.02	1.54×10^{-3}	0.951
180	7.76	1.52×10^{-3}	0.946
200	8.51	1.48×10^{-3}	0.941
220	9.28	1.43×10^{-3}	0.940
240	1.02	1.39×10^{-3}	0.938
260	1.11	1.37×10^{-3}	0.935
280	1.24	1.40×10^{-3}	0.920

Table 2.5: Fit parameters of the CPE element for the porous/capped electrode at 460 °C.

U_{DC} (mV)	R_s (Ωcm^2)	Q (mF s^{n-1})	n ()
0	2.88×10^1	2.47×10^{-3}	0.953
20	3.50×10^1	2.41×10^{-3}	0.952
40	4.12×10^1	2.36×10^{-3}	0.951
60	4.53×10^1	2.32×10^{-3}	0.957
80	4.67×10^1	2.33×10^{-3}	0.961
100	4.64×10^1	2.53×10^{-3}	0.963
120	4.56×10^1	3.06×10^{-3}	0.968
140	4.44×10^1	4.42×10^{-3}	0.973
160	4.35×10^1	6.93×10^{-3}	0.976
180	4.31×10^1	1.05×10^{-2}	0.977
200	4.32×10^1	1.38×10^{-2}	0.984
220	4.45×10^1	1.49×10^{-2}	0.982
240	4.69×10^1	1.44×10^{-2}	0.985
260	5.06×10^1	1.25×10^{-2}	0.975
280	5.37×10^1	1.12×10^{-2}	0.992
300	5.93×10^1	9.61×10^{-3}	0.989
320	6.62×10^1	8.27×10^{-3}	0.988
340	7.24×10^1	7.22×10^{-3}	0.990
360	7.14×10^1	6.61×10^{-3}	0.986
380	6.31×10^1	6.68×10^{-3}	0.999

3 Closed Pore Formation in Oxygen Electrodes for Solid Oxide Electrolysis Cells Investigated by Impedance Spectroscopy

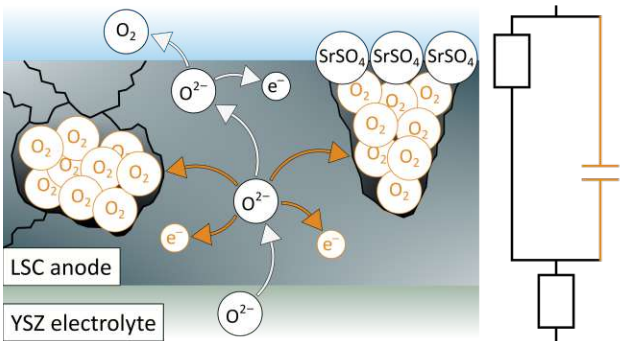

The study presented in this chapter has been accepted for publication:
Krammer, M.; Schmid, A.; Nenning, A.; Bumberger, A. E.; Siebenhofer, M.; Herzig, C.; Limbeck, A.; Rameshan, C.; Kubicek, M.; Fleig, J. Closed Pore Formation in Oxygen Electrodes for Solid Oxide Electrolysis Cells Investigated by Impedance Spectroscopy. *ACS Applied Materials & Interfaces* **2023**. DOI: 10.1021/acsami.2c20731.

3.1 Introduction

In order to prevent destructive mechanical load on the oxygen electrode side of SOECs, it would be beneficial to observe the buildup of internal gas pressures at an early stage. In Chapter 2 it was shown that thin film electrodes with intentionally built-in closed porosity exhibit a capacitance maximum at moderate anodic polarization. Thermodynamic calculations based on a real gas model clearly demonstrate that the build-up of high-pressure oxygen in closed pores causes this chemical capacitance peak. These findings also indicate that such capacitance measurements might be a highly sensitive tool for detecting closed pores in or near oxygen electrodes of SOECs.

In this chapter, we apply this tool to investigate the chemical capacitance of $La_{0.6}Sr_{0.4}CoO_{3-\delta}$ (LSC) thin film electrodes after annealing and bias voltage treatments, respectively, which are both known to induce degradation phenomena in oxygen electrodes of SOECs. We observed that electrodes with initially open pores or cracks exhibit a capacitance peak under anodic polarization (*i.e.* in the electrolysis mode) after several hours of annealing in synthetic air. A peak of the chemical capacitance also develops in the case of dense electrodes after applying high anodic bias voltages >750 mV. It is shown that in both cases degradation mechanisms lead to the formation of closed pores and those can be detected by the chemical capacitance. The quantitative model from Chapter 2 is used to estimate the amount of closed porosity and indicates the potential of the presented electrochemical method for detecting and quantifying closed pores in or near oxygen electrodes of SOECs.

3.2 Experimental

3.2.1 Sample preparation

All thin films of this study were deposited on yttria-stabilized zirconia (YSZ) single crystals ($5 \times 5 \times 0.5\,\mathrm{mm}^3$, (100)-oriented, 9.5 mol % Y_2O_3; CrysTec, Germany), which served as electrolytes and substrates. The thin film working and counter electrodes were prepared via pulsed laser deposition (PLD). The targets for the PLD deposition of $La_{0.6}Sr_{0.4}CoO_{3-\delta}$ (LSC) were fabricated by Pechini synthesis and the obtained powder was calcined for 10 h at 800 °C. Thereafter, the powder was pressed to a pellet by cold isostatic pressing (300-310 MPa), followed by a sintering step of 12 h at 1200 °C in air. The film deposition was performed in a vacuum chamber with a KrF excimer laser (248 nm; Compex Pro 201F, Coherent, Germany). First, porous LSC counter electrodes were prepared by depositing at a substrate temperature of 450 °C and at an oxygen partial pressure of 0.4 mbar. These parameters were chosen based on former studies[59,60], which showed that LSC electrodes fabricated under these conditions exhibit very low polarization resistances due to nanopores leading to an increased surface area. Afterwards the LSC working electrodes were deposited. By varying the deposition parameters, five sample types were fabricated, which are different in terms of microstructure (*i.e.* porosity and surface area) and crystal structure of the working electrode: i) highly oriented, resembling epitaxial dense (epi/dense), ii) polycrystalline dense (poly/dense), iii) polycrystalline with cracks, otherwise dense (cracked/dense), iv) porous and v) porous films with a dense capping layer on top (porous/capped) (see Figure 3.1). The deposition parameters for the individual sample types are shown in Table 3.1.

Shortly before each deposition, the substrate temperature was determined with a pyrometer which was tuned to the emissivity of YSZ. The laser fluence inside the vacuum chamber was adjusted to approximately 1.1 J/cm² for the deposition of dense films (epi/dense, poly/dense and cracked/dense) and to about 1.4 J/cm² for the deposition of porous films.

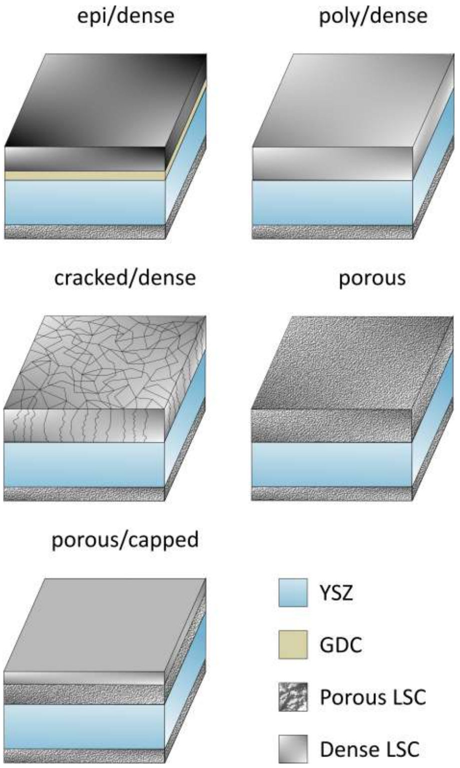

Figure 3.1: Sketches and nomenclature of the different sample types investigated in this study.

Table 3.1: Deposition parameters for the five different sample types investigated in this study.

Sample type	Temperature (°C)	Oxygen partial pressure (mbar)	Target-substrate distance (cm)	Special treatment
Epi/dense	600	0.04	6	GDC interlayer
Poly/dense	600	0.04	6	-
Cracked/dense	600	0.04	6	Deposited before counter electrode
Porous	450	0.4	5	-
Porous/capped	450/600	0.4/0.04	5/6	Poly/dense film on top

Thus, all films exhibited similar compositions with an average of $La_{0.605\pm0.023}Sr_{0.407\pm0.014}Co_{0.989\pm0.019}O_{3-\delta}$ determined by inductively coupled plasma-mass spectroscopy (ICP-MS). The laser was operated with a pulse repetition rate of 5 Hz for all depositions. For the preparation of the epi/dense films, 100 laser shots were fired onto a $Ce_{0.8}Gd_{0.2}O_{2-\delta}$ (GDC) target prior to the deposition of the dense LSC film, yielding a GDC interlayer of about 6 nm thickness. The parameters for the deposition of the poly/dense films were taken from former studies[61,62,81], in which cross sections from transmission electron microscopy (TEM) revealed densely packed columnar growth. The cracked/dense films were produced by changing the routine of the fabrication process: The film of the working electrode was deposited before the counter electrode preparation, *i.e.* before any heat exposure of the YSZ single crystal. Following this routine, cracks are formed in the working electrode (see Figure 3.3c). The deposition parameters for the porous samples were also chosen according to previous works, which used TEM bright field cross sections, high-angle annular dark field (HAADF) and ICP-MS measurements in order to demonstrate the porosity of the respective films.[59,81] The porous/capped electrodes were finally produced by first depositing a standard porous film, followed by an immediate change of the deposition parameters in order to deposit a dense capping layer with a thickness ranging from 8 to 15 nm. This deposition routine was also reported in a recent study[81], in which TEM cross sections confirmed the stacking of a dense LSC layer on top of a porous one. The porous part of those electrodes amounted to about 80 % of the total electrode thickness. Right after the deposition, all samples were cooled down in the respective atmosphere with a cooling rate of 15 °C per minute. Film thicknesses were determined from ICP-MS measurements using the lattice parameter from X-ray diffraction (XRD) and with a profilometer (DektakXT, Bruker, USA), respectively. By varying the amount of pulses, total electrode thicknesses between 43 and 285 nm were obtained.

The LSC films fabricated as working electrodes were then microstructured via photolithography and ion beam etching. In the first step of the photolithography process, the samples were coated with a photoresist (ma-N 1420 MicroResist Technology, Germany) while spinning on a spincoater. Afterwards the samples were placed on a heating stage for 5 min at 100 °C in order to evaporate the excess solvent. In the next step, a patterned shadow mask was placed above the sample and UV light (350 W, USHIO 350DP Hg, Japan) was employed to transfer the shape of circular microelectrodes with diameters of 195 to 300 µm to the photoresist. A different mask was used for the electrodes prepared for additional near ambient pressure X-ray spectroscopy measurements, which yielded rectangular electrodes with an area of 0.41 mm^2. The parts of the photoresist not being illuminated were removed with a developer solution (ma-D 533/s, MicroResist Technology, Germany). The uncovered areas of the films were etched away with an ion beam (KDC 40, Kaufman & Robinson, USA). For this purpose, a diffuse Ar plasma was operated at 9×10^{-4} mbar Ar with a beam voltage of 500 V and a beam current of 10 mA. The remaining photoresist on top of the microelectrodes was carefully removed using a clean room wipe soaked in ethanol.

3.2.2 Impedance spectroscopy

For most of the measurements the samples were placed inside a closed fused silica apparatus and symmetrically heated in a tube furnace to temperatures between 450 and 610 °C. A type S thermocouple located within 1 cm from the sample was used to measure the temperature.

The samples were placed on a platinum mesh to ensure electrical contact of the counter electrodes. For the electrical contact of the (working) microelectrodes, platinum-rhodium needles were applied and positioned with a microscope camera. Only the experiments with the cracked/dense LSC thin films were conducted with a different measurement setup. Those samples were placed in a vacuum chamber onto a corundum heating stage, which was coated with platinum in order to apply electrical contact of the counter electrodes. The (working) microelectrodes were contacted with a platinum needle, again using a microscope camera. Owing to the asymmetric heating in this measurement setup, the temperature of the working electrodes was calculated from the high frequency x-axis intercept in the impedance spectra, which corresponds to the ionic transport resistance R_{YSZ} of the electrolyte.[65,82]

Impedance spectra were recorded with DC bias voltages ranging from 0 to 1000 mV using an Alpha-A High Performance Frequency Analyzer and an Electrochemical Test Station POT/GAL 30 V/2 A (both: Novocontrol, Germany). All impedance measurements were conducted with an alternating root-mean-square voltage of 10 mV in the frequency range of 10^6 to 10^{-2} Hz with 5 data points per decade. The Electrochemical Test Station was also used to measure DC voltages and currents. Most of the measurements were performed in synthetic air. For the *in situ* near ambient pressure X-ray photoelectron spectroscopy experiments and the corresponding *ex situ* measurements, which were carried out for the purpose of comparison, an oxygen/nitrogen mixture with an oxygen partial pressure of 1 mbar was used. High purity gases (99.999 %, Messer Austria GmbH, Austria) were employed for all experiments.

3.2.3 Structural characterization

X-ray diffraction (XRD) measurements were performed to investigate the crystal structure of the different thin films and microelectrodes using an Empyrean X-ray diffractometer (Malvern Panalytical, UK) with a Cu radiation source in grazing incidence and Bragg Brentano geometry. For the grazing incidence scans, which were performed at an incidence angle of 2 °, a parallel beam mirror on the incident beam side and a parallel plate collimator together with a scintillation detector on the diffracted beam side were employed. A focusing mirror on the incident beam side and a semiconductor area detector (GaliPix3D, Malvern Panalytical, UK) on the diffracted beam side were applied for the measurements in Bragg Brentano geometry. In order to focus the beam onto individual microelectrodes, a 0.3 mm slit was used.

Atomic force microscopy (AFM) measurements were conducted in order to analyze the surface structure of different LSC samples (Nanoscope V multimode setup (Bruker, USA) operated in tapping mode).

3.2.4 Inductively coupled plasma mass spectrometry

The elemental composition of the LSC films was determined via an inductively coupled plasma mass spectrometer (ICP-MS), equipped with a quadrupole mass filter and a collision cell (iCAP QC, Thermo Fisher Scientific, Germany). Before the actual analysis, a two-step dissolution was performed according to former studies[62,81]: At first, the water-soluble Sr species, which possibly formed on the surface of the LSC thin films, were dissolved in 5 mL of freshly prepared ultra-pure water (BarnsteadTM EasypureTM II, 18.2 MΩcm) for 30 min. In the second step, 100 µL concentrated HCl was used to completely dissolve the remaining LSC thin film. The obtained data was processed using Qtegra software (Thermo Fisher Scientific, USA). Further details regarding the ICP-MS measurements are reported in a previous paper[81].

3.2.5 *In situ* near ambient pressure X-ray photoelectron spectroscopy

Near ambient pressure X-ray photoelectron spectroscopy (NAP-XPS) measurements were performed while simultaneously recording electrochemical impedance spectra as described above. NAP-XPS was carried out in a lab-based machine with monochromated Al K-α radiation (µFOCUS 500 NAP, SPECS, Germany) at an oxygen pressure of 1 mbar. The instrument is further equipped with a differentially pumped hemispherical electron energy analyzer (PHOIBOS 150 NAP, SPECS, Germany), which has a water-cooled nozzle and a sample stage optimized for solid state electrochemical characterization. Details regarding the sample stage can be found in an earlier study[83]. The sample was mounted on a Pt-coated Al_2O_3 disk with a 4.5 × 4.5 mm^2 central bore on which the sample with a size of 5 × 5 mm^2 is located. This enables direct sample heating with the near-infrared laser, as sketched in Figure 3.20 in the Appendix. The macroscopic porous LSC counter electrode was contacted through the sample stage, and the specifically designed rectangular LSC electrode (380 × 1080 µm^2) was contacted by a Pt-Ir tip. In order to avoid XPS peak shifts due to the applied voltage, the microelectrode was grounded and a negative bias was applied to the counter electrode.

The temperature of the sample was controlled using the high frequency x-axis intercept in the impedance spectra as described above. Due to the rectangular electrode geometry and a contribution of the electrode sheet resistance, the relation of sample temperature and high frequency resistance was calibrated *ex situ* in the homogeneously heated apparatus prior to the NAP-XPS measurements. XPS spectra were collected at an analyzer pass energy of 30 eV and processed by the software CasaXPS. A s-shaped "Shirley" background was used for all peaks. Components were fitted primarily with mixed Gaussian-Lorentzian peak shapes (for Sr 3d, most O 1s components and S 2p). Additionally, an asymmetric component ("LF" peak shape in CasaXPS) was used for the second O1s "bulk" component. Spin-orbit doublets of p and d orbitals were constrained to have equal FWHM, appropriate area ratio (2:3 for d and 1:2 for p transitions) and fixed energy separation (1.6 eV for Sr 3d and 1.2 eV for S 2p). For chemical quantification, the peak areas were further corrected for photo-excitation cross-section[84], analyzer transmission function and energy dependence of the photoelectron inelastic mean free path (IMFP $\approx {E_{kin}}^{0.8}$).

3.2.6 Transmission electron microscopy

For transmission electron microscopy (TEM) investigations, an electron-transparent lamella was prepared via standard lift-out techniques with a focused ion beam/scanning electron microscopy (FIB/SEM) system (Scios 2 DualBeam, Thermo Fisher Scientific, Germany), operating with a Ga-ion beam at 30 kV accelerating voltage. Final low-voltage cleaning of the lamella was performed at 2 and 5 kV. All TEM measurements were carried out on a 200 kV FEI TECNAI F20 equipped with an EDAX APOLLO XII detector for energy dispersive X-ray spectroscopy (EDX). Scanning transmission electron microscopy (STEM) and EDX line scans were performed with a probe size of approximately 2 nm and high-angle annular dark field (HAADF) camera lengths of 350 and 490 mm.

3.3 Structural and electrochemical characterization

3.3.1 X-ray diffraction

XRD measurements of the different sample types showed that all reflexes measured in grazing incidence and Bragg Brentano geometry could either be assigned to the pseudo-cubic structure of the LSC perovskite phase or the YSZ phase of the substrate (see Figure 3.2). The intensities of the individual reflexes varied between the different sample types and the applied measurement geometries. Diffractograms of pristine poly/dense, pristine porous and pristine porous/capped films were also part of an earlier study[81]. Figure 3.2a shows that the pristine porous film exhibits a low degree of crystallinity, since only one distinct peak is visible. However, after annealing for 54 h at 608 °C the porous LSC film shows all the reflexes obtained for the poly/dense film. Thus, some post-crystallization seems to occur in porous films upon annealing. The diffractogram of the epi/dense film, which was measured in Bragg-Brentano geometry, suggests highly oriented growth resembling fully epitaxial films, since only peaks from (100) planes were found (see Figure 3.2b). Moreover, Figure 3.2b shows diffractograms of a cracked/dense microelectrode which was "frozen" at 195 mV overpotential and 600 °C, as well as of a cracked/dense microelectrode "frozen" at 600 °C without polarization. The "frozen" samples were removed from the heating stage (at 600 °C) during an impedance measurement with/without DC bias voltage and rapidly cooled down to room temperature prior to the XRD measurement. No significant differences between the diffraction patterns of these two cracked/dense electrodes were observed. The low intensity of the corresponding peaks resulted from the application of a narrow slit, which was used to focus the beam onto individual microelectrodes. The unlabeled peaks at about 31.5 ° and 65.5 ° result from a reflection corresponding to the Cu K-β wavelength of the radiation source.

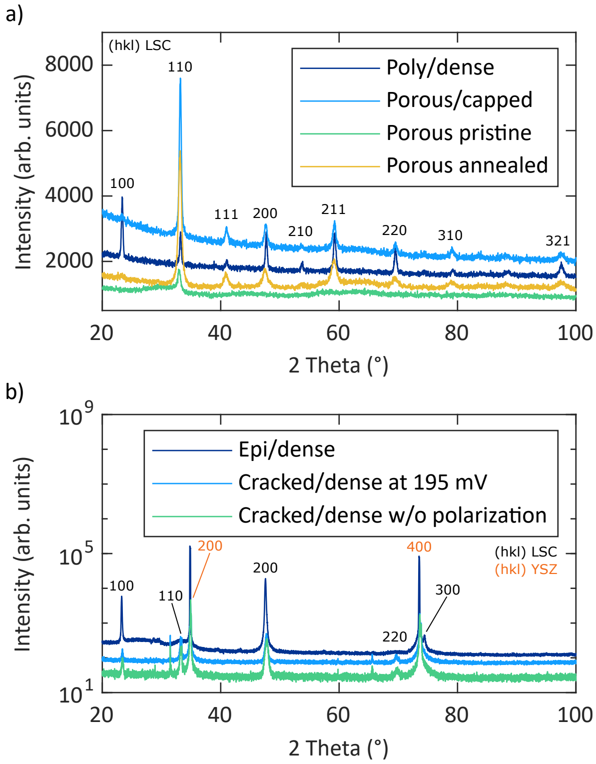

Figure 3.2: XRD diffractograms of pristine poly/dense[81], pristine porous/capped[81], pristine[81] and annealed porous films measured in the grazing incidence geometry (a), as well as of epi/dense and cracked/dense ("frozen" at 195 mV and 600 °C and without polarization history at 600 °C) films measured in the Bragg Brentano geometry (b).

3.3.2 Atomic force microscopy

Figure 3.3 displays AFM scans of pristine films corresponding to the different sample types investigated in this study. All films show distinguishable and homogeneously distributed grains. Films without a GDC interlayer, which were deposited at 600 °C and 0.04 mbar (poly/dense, cracked/dense) exhibit a larger grain size than those deposited at 460 °C and 0.4 mbar (porous, porous/capped), as expected from earlier studies[61,66]. The surface of the porous/capped film shows a similar grain size as the porous film, despite the deposition of a dense capping layer at 600 °C and 0.04 mbar. Hence, it is assumed that this dense capping layer adapts its grain size to the porous layer underneath. The AFM image of the cracked/dense sample also displays the cracks that were distinctive for these films. Furthermore, a porous film is shown which was annealed for more than 100 h at 608 °C. By comparing the pristine and the annealed porous film, it becomes apparent that large grains with heights up to about 100 nm were formed during annealing.

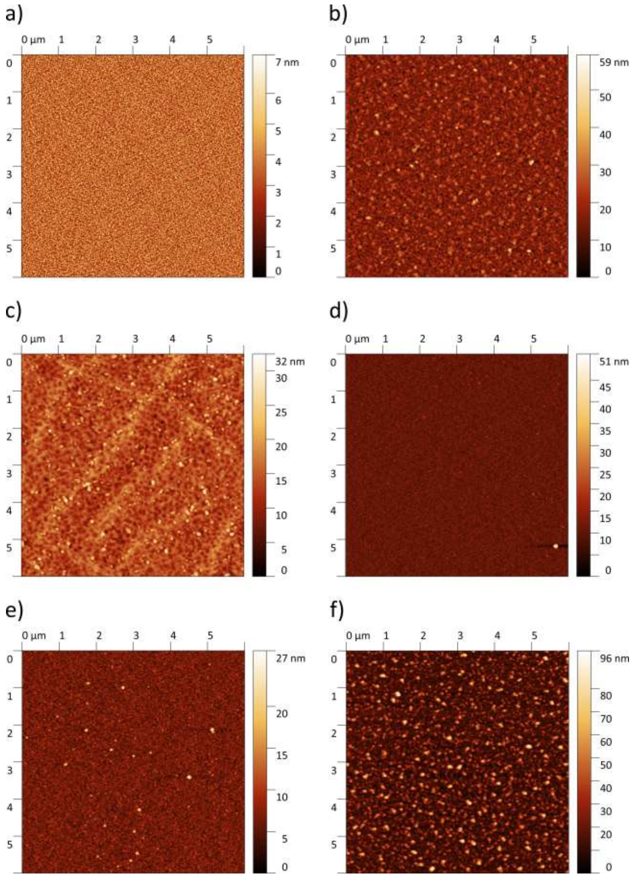

Figure 3.3: AFM scans of the different LSC sample types investigated in this study: pristine epi/dense (a), pristine poly/dense (b), pristine cracked/dense (c), pristine porous/capped (d), pristine porous (e) and annealed porous (f).

3.3.3 Impedance spectroscopy

The exemplary impedance spectra in Figure 3.4 show data from impedance measurements with applied bias voltages ranging from 0 to 440 mV. Please note that spectra of epi/dense electrodes are very similar to those shown for poly/dense electrodes (Figure 3.4a). Furthermore, porous/capped electrodes exhibit similar spectra as annealed porous ones (Figure 3.4c). All spectra contain a high frequency x-axis intercept which is temperature dependent, but independent of the applied bias voltage. In accordance with literature[56,59,65] this intercept can be attributed to the ionic transport resistance of the YSZ electrolyte (R_{YSZ}). The value of R_{YSZ} was determined from the intersection of the x-axis with the extrapolation of the electrode-related impedance feature. At intermediate frequencies, features are visible that

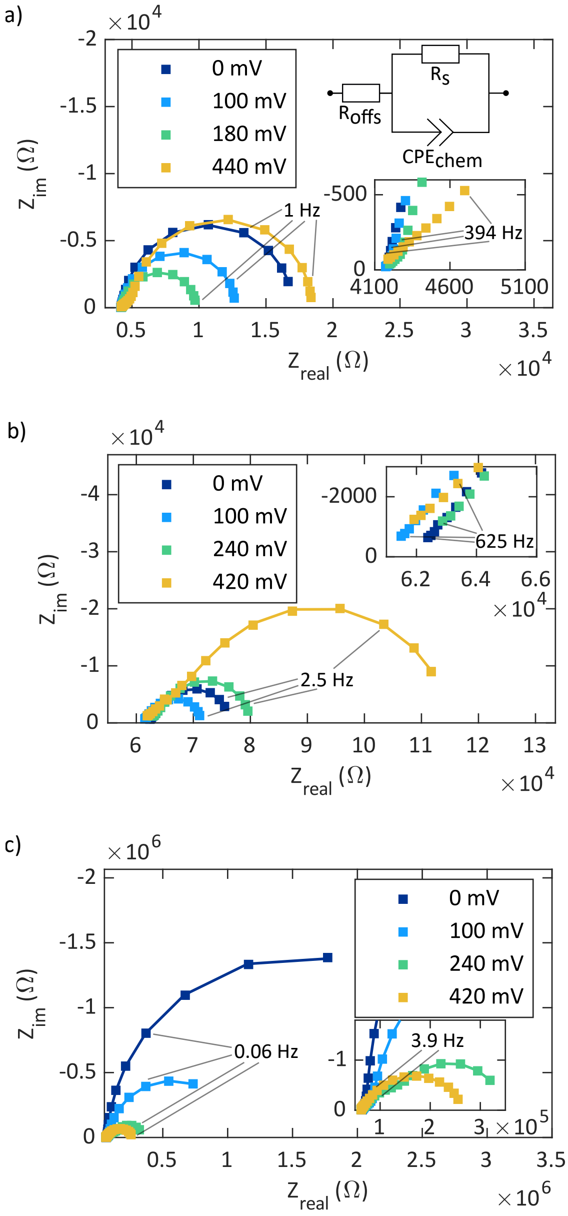

Figure 3.4: Impedance spectra of a pristine poly/dense (a), a pristine porous (b) and an annealed (6 h at 460 °C) porous (c) LSC thin film microelectrode at various DC bias voltages (U_{DC}) at measurement temperatures of 608 °C (poly/dense) and 460 °C (porous). Solid lines are fits to the shown equivalent circuit in a) (with the exception of spectra at 420 mV in b) and c), see Section 3.2.2).

vary depending on the sample type and on the annealing time and generally become larger with increasing bias voltage. Such contributions were also reported in previous studies on LSC[59,61,62] and are often associated with interfacial processes between the electrolyte and the electrode. As can be seen in Figure 3.4, some spectra resemble a Warburg-like behavior in the intermediate frequency range, which may indicate the onset of an oxygen diffusion limitation in the LSC working electrode. However, a finite Warburg element alone never yielded reasonable fit results of these spectra. Given that these intermediate frequency features were not the focal point of this study, their contributions were not examined in more detail.

At low frequencies, all spectra contain a semicircular-type feature, which is associated with the oxygen surface exchange resistance R_s and the chemical capacitance C_{chem} of the working electrode, in agreement with former studies on LSC and similar mixed conducting oxides[54–56,59,62,66]. The evaluation of the chemical capacitance C_{chem} under anodic polarization was the main focus of this work. For this purpose, the low frequency semicircle was fitted to a parallel connection of constant phase element (CPE_{chem}) and a resistance (R_s) using a non-linear least squares method. The impedance of a constant phase element is defined as

$$Z_{CPE} = \frac{1}{(j\omega)^n Q} \quad , \tag{3.1}$$

which considers the non-ideal behavior of a capacitance. With the parameter Q and the exponent n, both obtained from the fitting procedure, the chemical capacitance C_{chem} can be calculated via[70]

$$C_{chem} = (R_s^{1-n} \cdot Q)^{\frac{1}{n}} \quad . \tag{3.2}$$

Apart from the parallel connection of CPE_{chem} and R_s, the equivalent circuit used for the fitting procedure consisted of a serial resistance R_{offs} (see circuit in Figure 3.4a). This offset serial resistance R_{offs} considers the above described impedance contributions from the electrolyte (R_{YSZ}) and any intermediate frequency features. This simple equivalent circuit yielded the most reliable determination of the chemical capacitance, as long as the low frequency semicircle accounted for the major part of the corresponding spectrum and was reasonably well separated from intermediate frequency features. Under these conditions the oxygen chemical potential in the whole working electrode μ_O^{WE} is determined by the electrode's overpotential η_{WE} according to

$$\mu_O^{WE} = \mu_O^{at} + 2F\eta_{WE} \quad . \tag{3.3}$$

The symbol μ_O^{at} represents the oxygen chemical potential in the gas phase and η_{WE} is calculated via

$$\eta_{WE} = U_{DC} - \eta_{YSZ} = U_{DC} - I_{DC} \cdot R_{YSZ} \quad . \tag{3.4}$$

Here, U_{DC} is the applied DC bias voltage, I_{DC} stands for the DC current and η_{YSZ} is the electrolyte's overpotential caused by the finite ionic conductivity of YSZ. Accordingly, deviations caused by any interfacial resistance or transport limitation in the electrode are neglected. Also any overpotential contribution from the counter electrode was neglected, since its active area was at least 350 times larger than that of the (working) microelectrodes and its polarization resistance is very low as shown in a former study[59].

In most cases, the above described conditions were reasonably met, however, at very high bias voltages some spectra revealed intermediate frequency contributions similarly sized as the low frequency feature and partly merged with the latter. Such spectra (e.g. spectra at 420 mV in Figure 3.4b and 3.4c) would require a more sophisticated impedance analysis (at least two R/CPE elements and a resistance in series) and are not included in the following chemical capacitance analysis.

In general, oxygen exchange rates are governed by the concentrations of defects (holes, oxygen vacancies)[67,68], which in turn are strongly dependent on the overpotential[54]. Consequently, a significantly bias-dependent surface exchange resistance R_s can be expected. In combination with the non-trivial defect chemistry of LSC[73,75,85] and possible irreversible changes at very high anodic overpotentials (see below), the overpotential dependence of R_s is supposed to be rather complex. Since the chemical capacitance rather than the surface exchange resistance was in the main focus of this study, we did not investigate this overpotential-dependent behavior in detail. For the sake of completeness, Figure 3.17 in the Appendix shows the surface exchange resistance R_s of pristine and annealed electrodes of all different sample types determined with the simple equivalent circuit depicted in Figure 3.4a.

3.4 Chemical capacitance analysis

3.4.1 Chemical capacitance of pristine electrodes

Figure 3.5a displays the chemical capacitance curves of pristine electrodes as a function of the electrode overpotential. In this and all subsequent figures, the chemical capacitance values were normalised to the respective entire electrode volume, without subtracting cavity and pore volumes of cracked/dense, porous and porous/capped electrodes. The poly/dense and the epi/dense electrodes were measured at 608 °C (thermocouple), whereas a temperature of 600 °C was determined from R_{YSZ} for the cracked/dense electrode. Due to the superior oxygen exchange kinetics of pristine porous electrodes ($R_s < 0.1\ \Omega\text{cm}^2$ at 608 °C in synthetic air), their chemical capacitance was analyzed at a lower temperature (*i.e.* 460 °C) in order to obtain data at overpotentials comparable to the measurements on the other electrodes. Nevertheless, the chemical capacitance could only be evaluated up to $\eta_{WE} \approx 100$ mV because of a strong merging of the intermediate and the low frequency feature.
The curves of all pristine electrodes reveal a decrease of the chemical capacitance with increasing anodic overpotential (see Figure 3.5a). This behavior is consistent with previous studies on LSC and similar mixed conducting oxides.[54–56,81] The porous/capped electrode shows a different behavior and will be discussed later in this section. The chemical capaci-

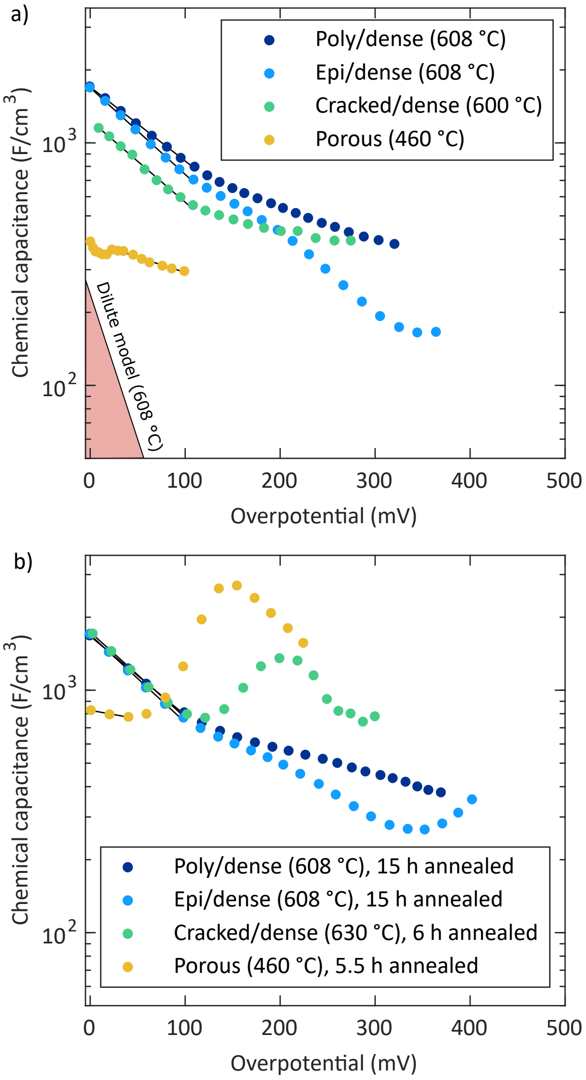

Figure 3.5: Chemical capacitance of different pristine (a) and annealed (b) LSC electrodes as a function of the electrode overpotential η_{WE}, measured at the indicated temperature and corresponding fits (solid line). The red triangle represents the slope corresponding to the dilute defect model at 608 °C.

tance is usually defined as follows[57,58]

$$C_{chem} = 4F^2 V \cdot \left(\frac{\partial \mu_O}{\partial c_O} \right)^{-1} \quad , \tag{3.5}$$

with F denoting the Faraday constant. Hence, C_{chem} scales with the electrode's volume V and the inverse derivative of the oxygen chemical potential μ_O with respect to the oxygen concentration c_O. Assuming dilute defects in an acceptor-doped mixed conducting oxide, the chemical capacitance of the solid can be expressed in terms of the concentrations of electronic defects (c_{eon}) and oxygen vacancies (c_V) as

$$C_{chem} = \frac{F^2 V}{RT} \left(\frac{1}{4c_V} + \frac{1}{c_{eon}} \right)^{-1} \quad . \tag{3.6}$$

T and R denote the temperature and the universal gas constant, respectively. Obviously, the chemical capacitance is largely determined by the minority charge carriers, which are oxygen vacancies in many SOEC-relevant perovskites under these conditions. In order to analyze the voltage-dependent chemical capacitances properly, it is useful to consider the individual contributions of atmosphere and voltage to the oxygen chemical potential inside the working electrode. Relative to 1 bar oxygen it is given by[54,55]

$$\mu_O^{WE} = \mu_O^{0,T} + \frac{RT}{2} \cdot \ln \left(\frac{p_{O_2}^{at}}{1\,\text{bar}} \right) + 2F\eta_{WE}, \tag{3.7}$$

where $p_{O_2}^{at}$ stands for the actual atmospheric oxygen partial pressure and $\mu_O^{0,T}$ is the chemical potential of oxygen gas at 1 bar. Please note that Equation (3.7) is valid as long as the transport of charge carriers in the electrode is fast in comparison to the oxygen exchange reaction at the surface and the atmospheric oxygen partial pressure $p_{O_2}^{at}$ reasonably well approximates the respective oxygen fugacity $f_{O_2}^{at}$ (see below). Moreover, we neglect that a part of the electrode overpotential η_{WE} refers to intermediate frequency features, which do not alter μ_O^{WE} in the entire film. However, given that C_{chem} was only evaluated for spectra with dominating low frequency arc, Equation (3.7) represents a solid approximation.

Accordingly, both increasing (anodic) overpotential and inreasing oxygen partial pressure increases the oxygen chemical potential in the working electrode, as also demonstrated experimentally in former studies[54,55]. Thus, we may define an effective internal oxygen partial pressure within the oxide of the working electrode $p_{O_2}^{WE,eff}$ [54,55,86] by

$$\mu_O^{WE} = \mu_O^{0} + \frac{RT}{2} \cdot \ln \left(\frac{p_{O_2}^{WE,eff}}{1\,\text{bar}} \right) \quad , \tag{3.8}$$

and together with Equation (3.7) one gets

$$p_{O_2}^{WE,eff} = p_{O_2}^{at} \cdot \exp \left(\frac{4F\eta_{WE}}{RT} \right) \quad . \tag{3.9}$$

In accordance with defect chemical studies on LSCF in literature[54,55,71–76,87], we attribute the measured decrease of the chemical capacitance values under increasing anodic overpotential to the decrease of the oxygen vacancy concentration. From the dilute defect model of an acceptor-doped oxide we get

$$\left(\frac{c_V}{c_V^{at}}\right) = \left(\frac{p_{O_2}^{WE,eff}}{p_{O_2}^{at}}\right)^{-1/2} \quad , \tag{3.10}$$

provided that the atmospheric vacancy concentration c_V^{at} is already in the range where vacancies are minority charge carriers. Combining Equation (3.10), (3.9) and (3.6) leads to

$$C_{chem} \approx \frac{4F^2 V c_V^{at}}{RT} \cdot \exp\left(\frac{-\alpha F \eta_{WE}}{RT}\right) \quad , \tag{3.11}$$

with an exponential factor $\alpha = 2$ (see bottom left corner in Figure 3.5a). For the poly/dense, epi/dense and cracked/dense electrodes, fits up to 100 mV yielded exponential factors between 0.5 and 0.6. This is close to the value obtained by Kawada *et al.*[55] (0.7) for $La_{0.6}Sr_{0.4}CoO_{3-\delta}$ electrodes deposited on a $Ce_{0.9}Ca_{0.1}O_{1.95}$ electrolyte substrate and measured at 600 °C and 0.1 bar oxygen partial pressure. The data for the pristine porous electrode does not follow a linear slope even at low overpotentials, which may be caused by crystallisation effects, since post-crystallisation was observed in the corresponding XRD measurements (see Figure 3.2a). However, deviations from the dilute defect model are not surprising considering the metal-like character of LSC[73,75] and we still assume that the chemical capacitances in Figure 3.5a are all determined by the overpotential-dependent oxygen vacancy concentrations.

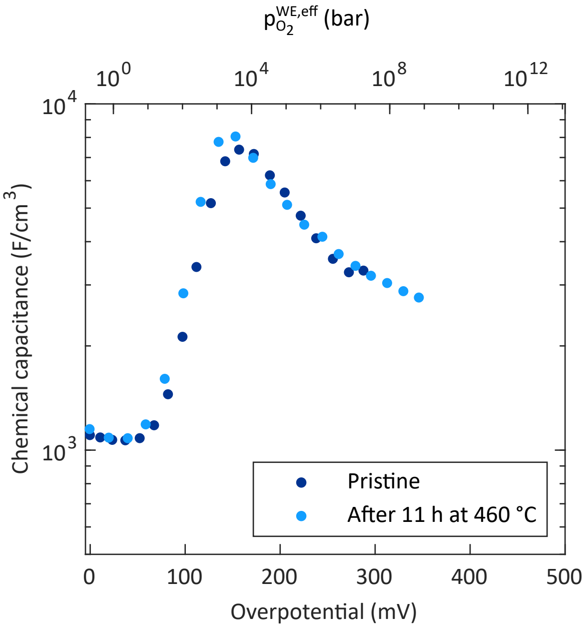

FIGURE 3.6: Chemical capacitance of a pristine and annealed (11 h at 460 °C) porous/capped electrode as a function of the electrode overpotential and the corresponding effective internal oxygen partial pressure, respectively, measured at 460 °C.

Figure 3.6 reveals that pristine porous electrodes with a polycrystalline, supposedly dense capping layer exhibit a completely different behavior compared to the pristine electrodes of all other sample types: After an initial minor decrease of the chemical capacitance at low overpotentials, a very pronounced peak can be observed with a maximum of >8000 F/cm^3 at about 150 mV. At overpotentials >150 mV the capacitance decreases again. This peak-shaped curve cannot be explained by the standard defect chemical interpretation of the chemical capacitance in an oxide[54–56]. Instead, another redox reaction has to be involved. This phenomenon was discussed and interpreted in detail in a previous work[81]. There, it is shown that the formation of highly pressurized oxygen in closed pores causes this capacitive effect. Since overpotentials between 150 and 250 mV would correspond to effective oxygen partial pressures $p_{O_2}^{WE,eff}$ ranging from 2.8×10^3 to 1.6×10^6 bar according to Equation (3.9), it is necessary to consider a real gas equation to predict the experimentally obtained peak-shaped capacitance curves[81], see also below. Consequently, a relation as in Equation (3.9) cannot be used for describing the gas pressure in closed pores, instead, it corresponds to the fugacity f_{O_2} of oxygen.

3.4.2 Appearance of a capacitance peak after annealing

The same measurements as described above were carried out after annealing the electrodes in synthetic air for several hours at the temperature of the subsequent measurement. Poly/dense and epi/dense electrodes were measured after 5, 10 and 15 h of annealing and showed very similar results as in the pristine state. Figure 3.5b depicts the capacitance curves of these electrodes after 15 h of annealing with slopes in the low overpotential range ($\eta_{WE} < 100$ mV) corresponding to exponential factors α between 0.6 and 0.7. The chemical capacitance curves of the cracked/dense and the porous electrodes, however, are completely different already after 6 and 5.5 h hours at 630 °C and 460 °C, respectively, compared to the corresponding pristine ones. They exhibit capacitance peaks at about 200 and 150 mV with high maximum values of about 1400 and 2700 F/cm^3, respectively (see Figure 3.5b). Hence, they show a behavior similar to (pristine) porous/capped electrodes.

Figure 3.7 displays chemical capacitance curves of another porous electrode obtained at 608 °C after an extensive pre-treatment, with annealing for about 112 h at temperatures between 460 and 608 °C and bias voltages up to 440 mV (corresponding to η_{WE} up to 385 mV). The chemical capacitance was probed by increasing bias to an overpotential (η_{WE}) of about 390 mV and back to 0 mV. Please note that the chemical capacitance was only evaluated up to overpotentials of about 250 mV due to an increase of the intermediate frequency feature and its merging with the low frequency semicircle at higher overpotentials (see analysis of impedance spectra). The curves for increasing and decreasing bias steps are almost identical, and they exhibit extremely high peak values of approximately 11 000 F/cm^3 at an overpotential of about 175 mV. This demonstrates that the electrode is not irreversibly changed by probing the peak. Rather, any microstructural or chemical phenomena leading to the capacitance peak have already taken place during annealing.

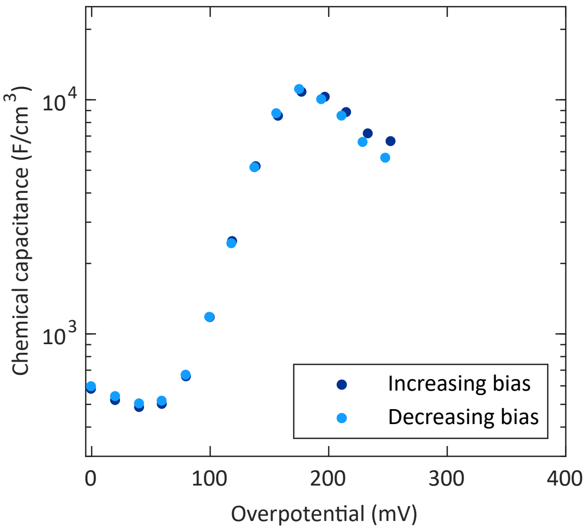

Figure 3.7: Chemical capacitance of a porous LSC electrode after annealing for about 112 h and after applying bias voltages (U_{DC}) up to 440 mV measured at 608 °C.

We can also conclude that capacitance peaks are only found for electrodes with increased inner surface (cracked/dense, porous and porous/capped electrodes). However, we still have to understand why the porous/capped films showed the peak already in the pristine state while the other electrodes required an annealing step. Here, a correlation between the appearance of the chemical capacitance peak, degradation of the oxygen exchange resistance and Sr segregation comes into play. From literature it is known that Sr segregates from the bulk to the surface of LSC thin films upon annealing in air and many studies indicate that this has a negative impact on the kinetics of the oxygen exchange reaction.[62,64,88,89] Degradation in terms of slower oxygen exchange kinetics is also found in the present study: For example, the surface exchange resistance of the porous LSC electrode (at $\eta_{WE} = 0$ mV) increased by more than two orders of magnitude after annealing for 5.5 h at 460 °C (see Figure 3.4b, 3.4c and 3.17 in the Appendix). This degradation is accompanied by the evolution of the chemical capacitance peak as explained above. Please note that defect concentration changes due to oxygen exchange at temperatures between 460 and 608 °C are related to equilibration times of a few seconds (see frequencies of impedance spectra in Figure 3.4). The occurrence of the chemical capacitance peak of porous and cracked/dense electrodes, however, always required annealing for several hours. Therefore, we do not consider chemical expansion as a primary factor causing the chemical capacitance peaks.

Our hypothesis of a relation between Sr segregation and the appearance of the chemical capacitance peak is also supported by the following experiment (see Figure 3.8). A porous electrode was measured in the pristine state, after annealing for 5.5 h and 11 h at 460 °C, respectively, and after annealing for 17 h and subsequently stirring the sample in double distilled H_2O for 30 min. The electrodes with a thermal history of 5.5 and 11 h exhibit very similar chemical capacitance values and a pronounced peak. However, after the H_2O treatment, the peak value decreased to less than one half compared to the measurement after 11 h at 460 °C. Figure 3.8b shows the corresponding surface exchange resistances at open circuit

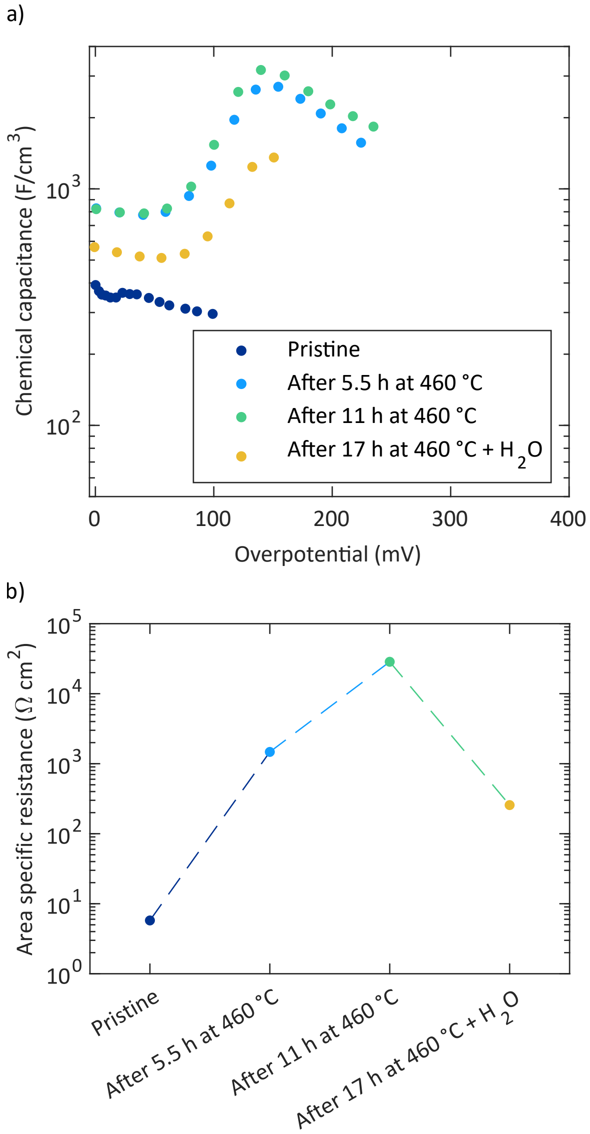

FIGURE 3.8: Chemical capacitance of porous LSC electrodes after different pre-treatments as a function of the electrode overpotential (a) and the corresponding surface exchange resistance R_s at open circuit conditions (b) measured at 460 °C (lines are a guide to the eye).

conditions. The two annealing steps increased the resistance by nearly four orders of magnitude, which we assume to be related to Sr segregation. The H_2O treatment clearly lowers the resistance in accordance with former studies[62,63] reporting enhanced oxygen exchange kinetics after removing a surface Sr species by H_2O. Hence, the lower surface exchange resistance found here after the H_2O treatment suggests at least a partial removal of a water soluble surface Sr species. A more detailed analysis of the relation between Sr segregation and the capacitance peak is presented below.

3.4.3 Appearance of a capacitance peak after high bias treatment

Apart from thermal pre-treatments we also investigated the chemical capacitance after applying high anodic bias voltages. Figure 3.9 shows chemical capacitance curves measured under moderate overpotentials after applying a high anodic bias voltage U_{DC} of 750 or 1000 mV for 1 h to poly/dense and epi/dense microelectrodes. It should be noted that those films did not show a chemical capacitance peak after annealing (see Figure 3.5b). Even a thermal history of more than 500 h at 608 °C did not lead to a chemical capacitance peak for a poly/dense electrode (see Figure 3.18 in the Appendix). Interestingly, anodic polarization for 1 h at U_{DC} = 750 mV (η_{WE} = 406 mV) led to a small capacitance peak for poly/dense films. Also epi/dense films show a small indication of a peak after such a bias treatment. Moreover, applying U_{DC} = 1000 mV (η_{WE} = 438 mV) for 1 h to a poly/dense electrode caused a substantial chemical capacitance peak of about 1400 F/cm^3. In this case, inspection with an optical microscope revealed that the corresponding electrode had undergone morphological changes due to this

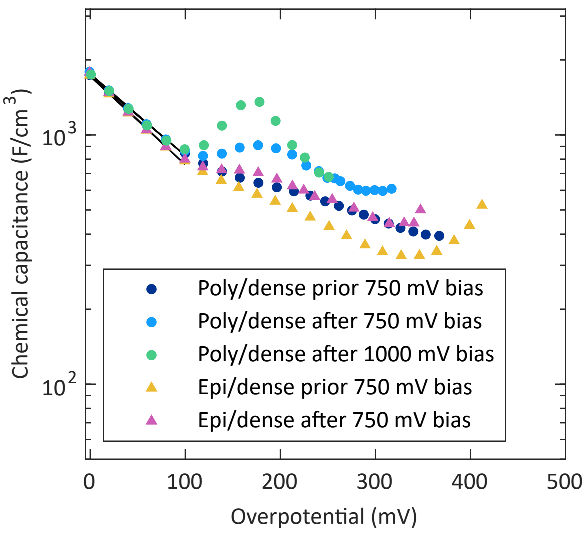

Figure 3.9: Chemical capacitance of annealed poly/dense and epi/dense electrodes before and after applying high anodic bias voltage (U_{DC}) for 1 h , measured at 608 °C and corresponding fits (solid line).

harsh bias treatment. A lower bias voltage of $U_{DC} = 200\,\text{mV}$ applied for more than 500 h, however, did not yield a significant C_{chem} increase (see Figure 3.19 in the Appendix). Accordingly, poly/dense films require the application of high bias voltages for developing a chemical capacitance peak. It is noteworthy that at low overpotentials (<100 mV), the chemical capacitance of all poly/dense as well as epi/dense electrodes did not change at all ($\alpha = 0.6$).

In a further measurement series we cycled different microelectrodes stepwise up to high bias voltages ($U_{DC} = 1000\,\text{mV}$, $\eta_{WE} = 384\,\text{mV}$) and back to 0 mV. Owing to the long measurement time (44 h), this inherently combined annealing and voltage treatment. Figure 3.10a shows the resulting curves of a cracked/dense electrode for two such cycles. Each cycle consisted of a forward run (increasing bias) and a subsequent reverse run (decreasing bias). We again see that at first the chemical capacitance decreases with increasing overpotential, as expected for a decreasing oxygen vacancy concentration. However, already in the first reverse run a very pronounced capacitance peak becomes visible. Please note that for overpotentials higher than 275 mV the spectra cannot be analyzed properly and thus chemical capacitances are not extractable there. During the second cycle, the peak remains with only little changes in the forward run and an increased peak value in the reverse run. This further demonstrates the reproducibility of the chemical capacitance peak and that it is caused by a process occurring under high polarization at the end of the first forward run, *i.e.* at higher overpotentials than the peak detection itself. The corresponding current of the two cycles is given in Figure 3.10b. The strong increase in the first forward run at the highest voltages indicates some drastic changes of the surface reaction kinetics which seems to be associated with some permanent morphological changes of the electrode, since currents of all following cycles were increased at overpotentials higher than 250 mV in comparison to the first run. These bias induced changes differ from those triggered by the annealing itself since the polarization resistance was decreased here.

The sketch in Figure 3.11 summarizes the different samples, pre-treatments, results, the corresponding underlying mechanisms and the employed experiments justifying this interpretation. The suggested mechanisms and their validation are elucidated in detail in the subsequent discussion.

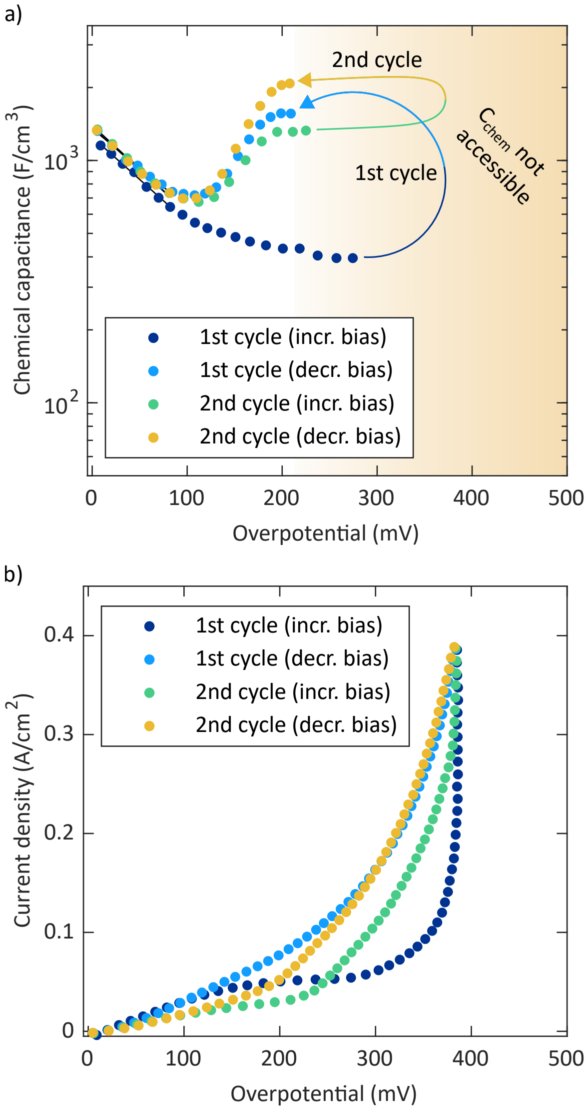

FIGURE 3.10: (a) Chemical capacitance of a cracked/dense electrode at a temperature of 600 °C that was cycled twice up to $U_{DC} = 1000$ mV and back to 0 mV (with 20 mV steps). For high bias voltages the chemical capacitance was not accessible from the analysis of the spectra (indicated by marked area). (b) Corresponding current density.

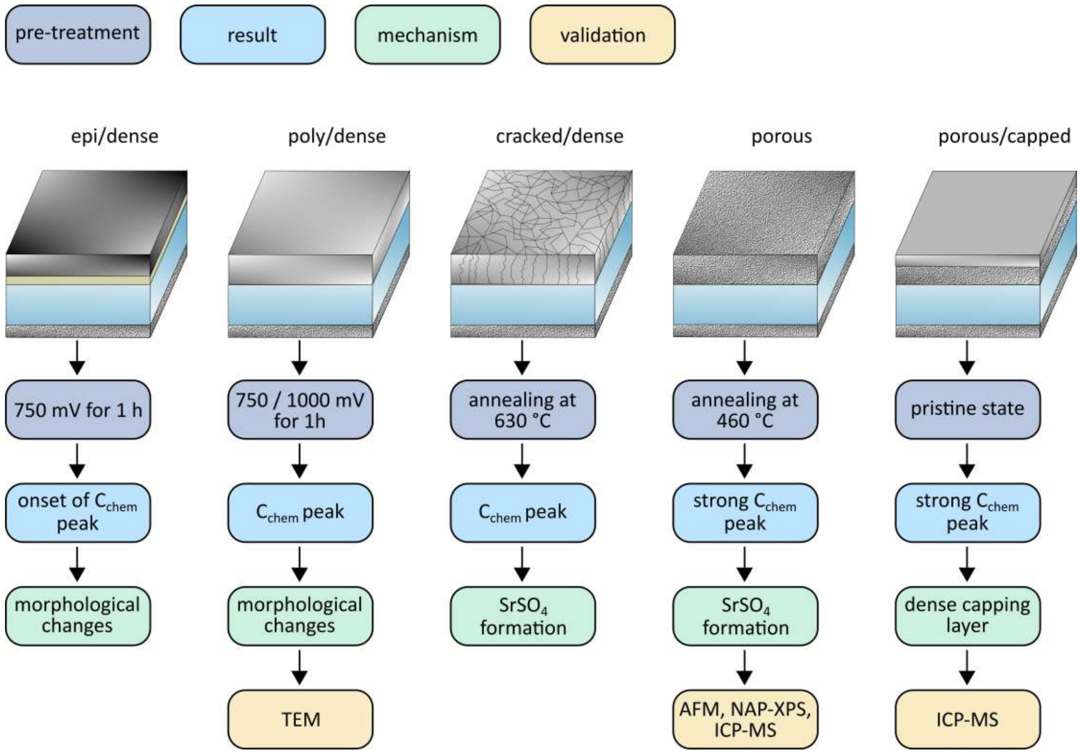

Figure 3.11: Schematic of the different samples, pre-treatments, results, corresponding underlying mechanisms and analytical techniques employed for their justification.

3.5 Mechanistic model and its validation

3.5.1 Degradation mechanisms causing chemical capacitance peaks

We now introduce a mechanistic model explaining the described chemical capacitance peaks and their dependence on the samples' pre-treatment and microstructure. Regardless of the electrode type or the pre-treatment, all capacitance peaks are similarly shaped and are found at similar overpotentials. Therefore, we suggest that they all can be traced back to the same underlying mechanism. As shown in a former study[81] and briefly discussed above, porous/capped electrodes exhibit a capacitance peak already in the pristine state due to high pressure oxygen gas formation in closed pores. Closed porosity seems to be the key requirement for the occurrence of the capacitance peak as this is the distinctive property of pristine porous/capped electrodes. Thus, we conclude that all other pristine films do not show a capacitance peak due to the absence of closed pores and that either annealing or treatment with high bias voltages induces such closed pores and the possibility of filling them with highly pressurized oxygen under anodic polarization. This then manifests itself in chemical capacitance peaks.

Despite the same origin of capacitance peaks in all films (pressurized oxygen in closed pores), the mechanism of forming those closed pores may be manifold. In our case, we seem to face two different mechanisms. The first refers to electrodes with open pores or cracks in the pristine state (porous and cracked/dense). Here we propose that upon annealing in synthetic air, Sr segregates from the bulk of the LSC film to the surface as revealed in former studies[62,64,88]. Initially this surface Sr may exist in the form of SrO or a SrO termination layer.[62,64,90] However, LSC is known to be very prone to sulfur poisoning from the gas phase[91,92] and in accordance with literature[93,94], we expect that even for annealing in synthetic air, minute traces of sulfur cause the formation of $SrSO_4$ particles. We suppose that those particles grow at crack or pore surfaces and finally reach a size that leads to the closure of open pores or cracks (see sketch in Figure 3.12a). This process leads to higher surface exchange resistances as well as to the appearance of a capacitance peak as depicted in Figure 3.8 for a porous electrode. A further validation of this hypothesis by means of surface sensitive analytical techniques is given in the subsequent section.

Owing to the absence of open pores or cracks, this mechanism does not work for dense electrodes (poly/dense and epi/dense), despite Sr segregation. There, we suppose that high anodic bias voltages lead locally to such a high mechanical load that morphological changes take place, ultimately resulting in closed pores or cracks in dense films as sketched in Figure 3.12b. As described above, for a bias voltage of 1000 mV, such morphological changes were already visible in the optical microscope. The formation of such closed pores after a bias treatment was also confirmed via cross-sectional TEM measurements, see below.

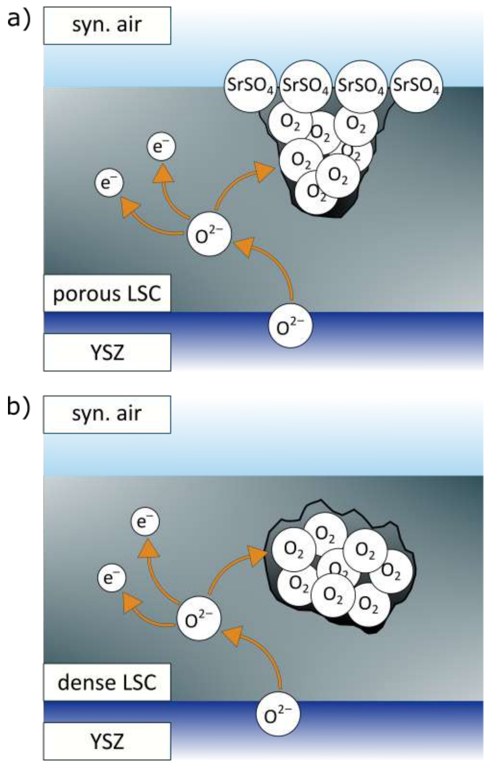

FIGURE 3.12: Sketch of the formation of high pressure oxygen in pores of a porous film which get closed due to a $SrSO_4$ phase formed upon annealing (a) and in closed pores of a dense film caused by high bias treatment (b).

3.5.2 Analysis of surface species

ICP-MS

For electrodes with open inner surfaces (porous and cracked/dense), we suggested that Sr segregation during annealing plays an important role for the closure of open pores. For the purpose of validation, we analyzed the surface compositions of pristine and annealed LSC thin films of different sample types via ICP-MS measurements using an approach already applied in previous studies[59,62,63,81]. Furthermore, by employing this method we can get information about the morphology of the studied LSC films, which is another important aspect of our mechanistic model.

As shown in literature[59,62,63], a water soluble Sr species may form on the surface of LSC films. The amount of this species and a possible dependence on the film microstructure and annealing treatments was examined by stirring the films in pure H_2O (particularly leaching surface species) and then dissolving them in hydrochloric acid, in both cases followed by a subsequent chemical analysis of the solute via ICP-MS. Two equally prepared samples were investigated, one was analyzed in its pristine state and the other one was annealed for 15 h at 608 °C in synthetic air prior to the ICP-MS measurement. After the treatment with pure H_2O

and the first ICP-MS measurement, the films were completely dissolved in hydrochloric acid to determine the amount of Sr in the bulk (c_{bulk}) (including surface species which are not soluble in H_2O). The amount of (water soluble) surface Sr (c_{surf}) was related to the amount of Sr in the entire film ($c_{total} = c_{surf} + c_{bulk}$). Thereby it was possible to compare the results of different sample types. Table 3.2 displays the corresponding results for poly/dense, porous and porous capped films.

Table 3.2: Ratio of water soluble surface Sr (c_{surf}) to total Sr ($c_{total} = c_{surf} + c_{bulk}$) of LSC thin films

Sample type	c_{surf}/c_{total} (%) of pristine state[81]	c_{surf}/c_{total} (%) after 15 h at 608 °C
Poly/dense	0.86	2.00
Porous	6.75	5.86
Porous/capped	1.09	3.99

Assuming a homogeneous distribution of the water soluble Sr species across the entire surface, these measurements give information on the water accessible surface area and thus also on the morphology of the respective film. The analysis of the pristine films was already part of an earlier study[81], which identified similar amounts of water soluble surface Sr for poly/dense and porous/capped films. Accordingly, the top layer of the porous/capped electrode has a similar morphology as the poly/dense electrode and thus indeed closes the open pores in the bottom layer. This is the reason for the appearance of the capacitance peak already in the pristine state of porous/capped films, and also for the absence of any further changes after annealing (see Figure 3.6), since Sr surface species formed upon annealing did not contribute to a substantial increase of closed porosity. Porous films, on the other hand, have large amounts of water soluble surface Sr (see Table 3.2), indicating open porosity with a 7 to 8 times larger accessible surface area than poly/dense films, in agreement with an earlier study[59].

After annealing, the amount of water soluble surface Sr strongly increased in the case of poly/dense and porous/capped films as expected due to Sr segregation to the surface.[62,64,88] However, the porous film seems to have less Sr on the surface after the annealing process compared to its pristine state. This supports our suggested model, as we suppose that during annealing in synthetic air, a less soluble Sr containing species is formed ($SrSO_4$) that caused the closure of a part of the open pores. Hence, the water-accessible surface area is reduced, leading to a slight decrease of water soluble Sr species, despite further Sr segregation during the annealing process. Moreover, this is also in agreement with the fact that the H_2O treatment only lowers the capacitance peak (Figure 3.8a), *i.e.* only partially reopens pores.

These results reveal that Sr indeed segregates from the bulk to the surface of our LSC films, thus supporting the described degradation mechanism. The Sr rich surface phase formed upon annealing was investigated in more detail by NAP-XPS (see next section).

In situ NAP-XPS

In situ NAP-XPS was used to further investigate the surface chemistry of LSC thin films. Impedance measurements were conducted with porous and poly/dense rectangular microelectrodes while recording XPS spectra at 1 mbar oxygen pressure. Anodic bias was applied and the corresponding chemical capacitance was analyzed as described above. Hence, in addition to analyzing the composition of the surface species, we could investigate whether these species change under conditions where the chemical capacitance peak is found.

The lower oxygen pressure of 1 mbar inside the XPS chamber compared to the *ex situ* measurements had to be considered for this analysis. According to Nernst's equation, additional 84 mV are necessary at 460 °C to yield the same oxygen chemical potential as in air. An *ex situ* measurement in air as well as at 1 mbar oxygen partial pressure confirmed this consideration: The onset of the corresponding capacitance peak indeed shifted by almost 80 mV, see Figure 3.21a in the Appendix. This shows, in accordance with former studies[54,55], that the chemical capacitance solely depends on the chemical potential of oxygen in the working electrode (see Equation (3.7)).

In order to observe any bias induced chemical changes at the surface, we recorded O 1s spectra (see Figure 3.21b in the Appendix). In general, all obtained O 1s spectra consist of two distinctive signals, which were fitted according to three components. The component at high binding energy (531.5 eV) is usually identified as surface component (O 1s surf), whereas the component at low binding energy (528.5 eV) is generally considered as "bulk" oxygen.[83,95–97] The O 1s bulk peak is strongly asymmetric and only the addition of a third species close to the main bulk peak leads to a well converging fit. This asymmetry is attributed to the metal-like electronic structure of LSC[73,75]. More details on this asymmetric feature can be found in the Appendix.

O 1s spectra were recorded on a porous electrode, which was annealed for more than 25 h at 460 °C in synthetic air prior to the NAP-XPS measurement. *In situ* impedance spectra revealed a capacitance peak at an overpotential of about 243 mV at 460 °C, which is in accordance with the expected position when taking account of the lower oxygen pressure of 1 mbar inside the XPS chamber. Figure 3.21b in the Appendix displays the corresponding O 1s signals from simultaneously performed XPS measurements. Neither a significant peak shift nor a strong change of the intensities was found for the XPS spectra at 243 mV compared to the spectra at open circuit conditions.

In addition, O 1s spectra were also recorded on a poly/dense electrode, pre-treated with a bias voltage of U_{DC} = 750 mV for 1 h. As shown above, such electrodes exhibited a chemical capacitance peak after the application of this high bias voltage. Again, owing to the lower oxygen pressure of 1 mbar, the capacitance peak was observed at 245 mV. As in the case of the annealed porous electrode, O 1s spectra recorded at the capacitance maximum-related overpotential and at open circuit conditions are very similar (see Figure 3.21b in the Appendix). Thus, there seems to be no XPS-accessible surface redox process that can be directly related to the chemical capacitance peak at the respective anodic overpotential. Rather, for both porous and dense electrodes, the processes relevant for the existence of a capacitance peak have already taken place during the different pre-treatments, *i.e.* annealing and application of high anodic bias voltage. This is in accordance with our mechanistic model suggesting closed porosity as the main cause for the capacitive peak.

For analyzing the thermally induced degradation in more detail O 1s, Sr 3d and S 2p spectra of pristine and annealed (*ex situ* in synthetic air) poly/dense and porous electrodes were recorded under open circuit conditions (see Figure 3.13). The intensities of the surface related O 1s and Sr 3d (Sr 3d surf) signals and particularly the S 2p related species increased after annealing in synthetic air. Corresponding *in situ* impedance measurements revealed an increase of the surface exchange resistance R_s by several orders of magnitude after annealing. Additional *in situ* measurements with a cathodic overpotential of about 230 mV neither changed the capacitance peak of a subsequent anodic measurement, nor had an effect on the simultaneously recorded S 2p signal. The total S 2p signal is plotted against the surface O 1s signal after various annealing times (see Figure 3.13d), yielding a linear correlation between these signals. This indicates that the surface O 1s signal is mainly caused by a sulfur containing species. In combination with the Sr 3d signal it can be concluded that the phase on the surface mainly consists of sulfur, strontium and oxygen. Accordingly, despite the use of very clean gases (*i.e.* 99.999 % purity) in all experiments, formation of $SrSO_4$ occurs during long annealing times, in agreement with results of previous studies[91,93,94,98,99]. This probably also caused the severe degradation of the oxygen exchange kinetics of the LSC thin films measured here (see Figure 3.17 in the Appendix). Moreover, we may conclude that the large grains visible in the AFM scan of the annealed porous film (see Figure 3.3) consist of this $SrSO_4$ phase. This is in line with recent studies[98,100], which showed that trace amounts of sulfur (ca. 0.5 ppmv) are present in typical measurement setups even when using high purity measurement gases. Also $SrCO_3$ may form due to trace amounts of CO_2. However, carbonates are supposed to desorb at the temperatures used in this study.[101]

Hence, these findings are in excellent agreement with the suggested mechanism that initially open pores or cracks become closed during annealing as a result of $SrSO_4$ formation. Under anodic polarization, high pressure oxygen then forms in these closed pores, leading to the observed chemical capacitance peak. Remarkably, these closed pores seem to withstand pressures in the range of 10^4 bar (calculated via the Soave-Redlich-Kwong real gas equation as shown in a previous study[81]) since consecutive measurements of the chemical capacitance on a porous electrode yielded almost identical curves (see Figure 3.7).

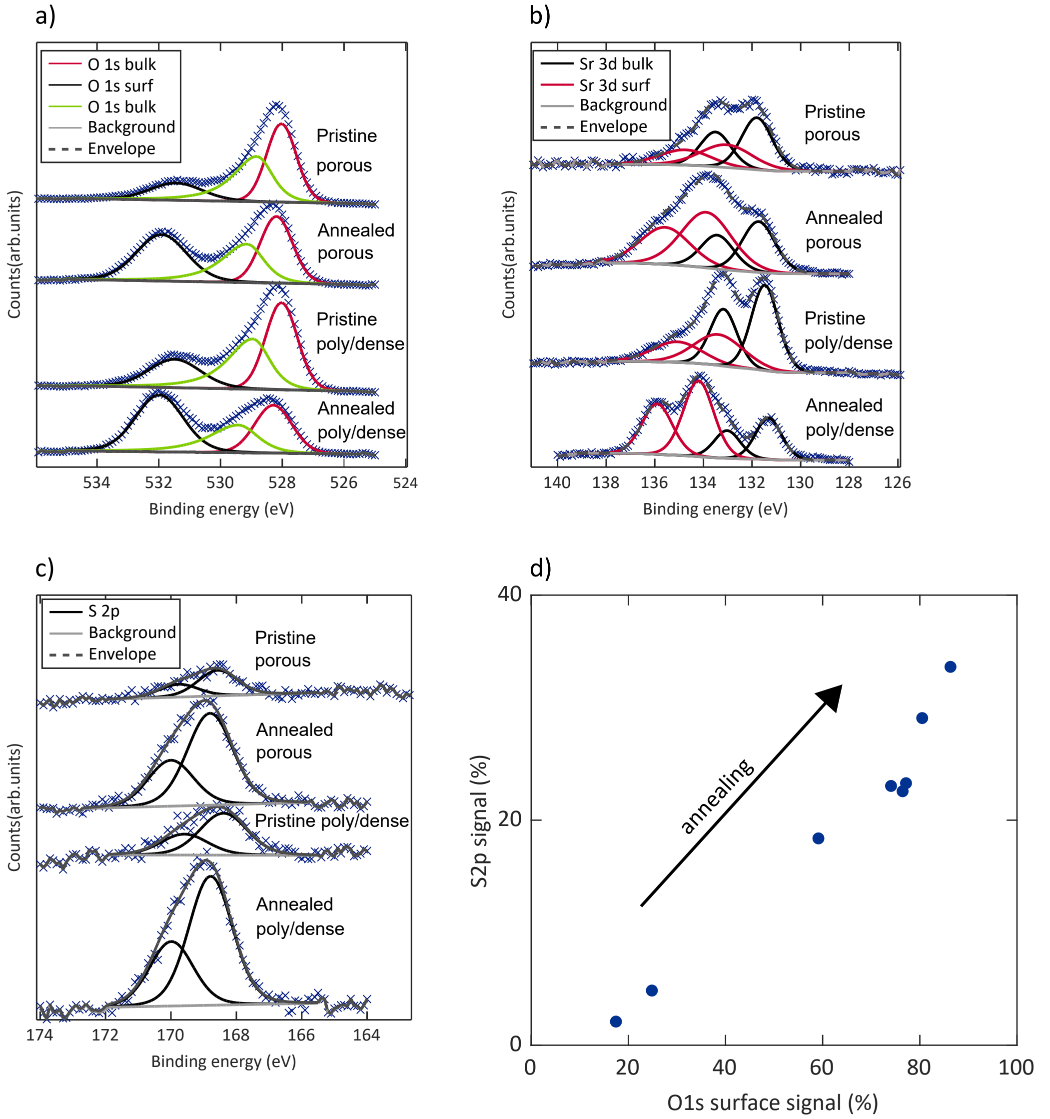

Figure 3.13: O 1s (a), Sr 3d (b) and S 2p (c) spectra of pristine and annealed poly/dense and porous electrodes (counts marked by blue crosses). (d) S 2p signal plotted against O 1s surface signal (both signals are related to total cation counts).

3.5.3 Identification of voltage induced morphological changes

TEM and HAADF-STEM measurements were performed on a lamella with 10 µm length, prepared from a poly/dense electrode after applying a bias voltage of $U_{DC} = 750$ mV for 1 h at 608 °C. The chemical capacitance analysis of this film is displayed in Figure 3.9, revealing a peak at an overpotential of approximately 175 mV. According to our model, this peak indicates bias induced formation of closed pores. HAADF-STEM measurements and EDX scans confirmed the existence of such closed pores as the elemental counts of respective areas are significantly lower, as shown in Figure 3.14. At the position of about 45 nm in the EDX scan an increase of both cobalt and oxygen signals is obtained. This may be associated with the small protrusion in the area of the investigated closed pore. The corresponding increase of the cobalt and oxygen signal could result from a Co_3O_4 phase which may has formed under anodic polarization, as similarly found in a former study[102] for an LSCF oxygen electrode after SOEC operation. A bright field TEM (BF-TEM) image of the closed pore in Figure 3.14 is displayed in Figure 3.22 in the Appendix, where the brighter area indicates the position of the pore (marked with dashed red line). Another closed pore in the bulk of this poly/dense film is shown in the HAADF-STEM image of Figure 3.15a. The corresponding BF-TEM image of this closed pore is depicted in Figure 3.15b. On the left next to this closed pore a crack seems to extend from the bulk to the surface or a near-surface layer (see Figure 3.15a).

In line with our suggested model mechanism, anodic bias voltages ≥750 mV (*i.e.* overpotentials >400 mV) may thus lead to mechanical failure of our dense films and the formation of closed pores in the respective electrodes. Unlike other studies on LSCF electrodes[43,45,46,48], which reported pore and crack formation at the electrode/electrolyte interface and delamination of the electrode from the electrolyte or the barrier layer, here it seems that pores and cracks form in the bulk of the electrode. This may indicate a very good adhesion of our poly/dense LSC electrodes to the YSZ electrolyte.

3.5.4 Porosity estimation based on a real gas model

From all these results we conclude that closed porosity is necessary for obtaining the observed chemical capacitance peak under anodic polarization. These closed pores either result when depositing a dense capping layer on top of a porous electrode (porous/capped) or by two different degradation phenomena: i) Upon annealing cracked/dense or porous electrodes for several hours in synthetic air, minute traces of sulfur containing species react with a SrO phase formed due to Sr segregation to the surface and probably also pull out further Sr from the film to form large $SrSO_4$ particles. This $SrSO_4$ causes the closure of at least a part of the initially open pores (see Figure 3.12a). ii) The second degradation mechanism involves mechanical failure due to the application of high bias voltage (U_{DC} ≥750 mV). HAADF STEM and EDX measurements revealed closed pores in the bulk of poly/dense films after such bias treatments (see Figure 3.12b). For both degradation processes, subsequently recorded impedance spectra revealed chemical capacitance peaks between 140 and 200 mV (in synthetic air).

The same kind of capacitance peaks also result for porous/capped electrodes, where closed porosity was intentionally introduced during the fabrication process. In Chapter 2, a detailed model was introduced to quantify these capacitance peaks by considering the formation of highly pressurized oxygen in closed pores using a real gas equation. By including pressure values $p_{O_2}^{pore}$ and fugacity coefficients φ determined from the Soave-Redlich-Kwong real gas

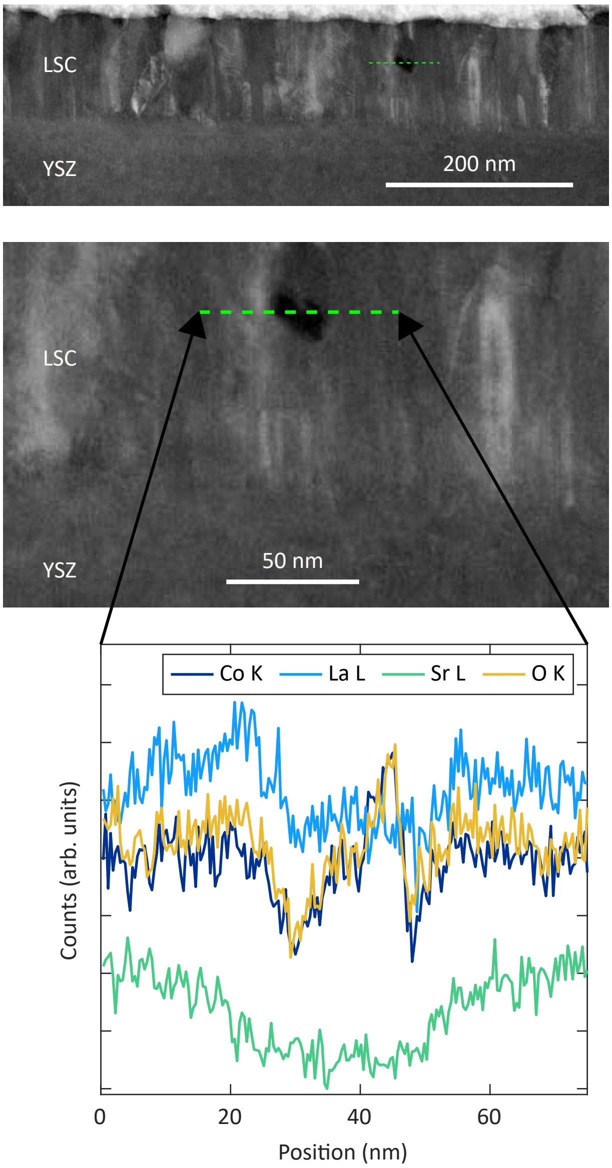

Figure 3.14: HAADF-STEM measurement (top image and section thereof in the middle) and EDX analysis (bottom) of green marked area of a poly/dense electrode after applying 750 mV for 1 h.

equation, the chemical capacitance can be calculated as follows

$$C_{chem}^{gas,real} = 16F^2\lambda V \cdot \left(\frac{\partial \mu_{O_2}}{\partial c_{O_2}}\right)^{-1} = 16F^2\lambda V \cdot \left(\frac{\partial\left(\mu_{O_2}^{0,T} + RT\ln\left(\frac{\varphi p_{O_2}^{pore}}{1\,\mathrm{bar}}\right)\right)}{\partial c_{O_2}}\right)^{-1}$$
$$= \frac{16F^2\lambda V}{RT} \cdot \left(\frac{\partial\left(\ln\left(\frac{\varphi p_{O_2}^{pore}}{1\,\mathrm{bar}}\right)\right)}{\partial c_{O_2}}\right)^{-1}, \qquad (3.12)$$

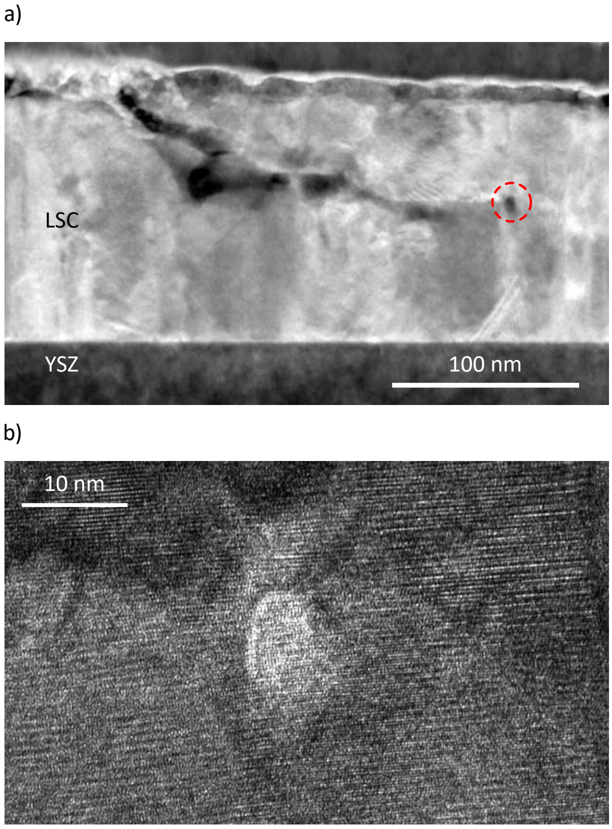

Figure 3.15: (a) HAADF STEM measurement of a poly/dense electrode after applying 750 mV for 1 h revealing a closed pore (marked with dashed red line) and a crack in the bulk of the film. (b) BF-TEM image of the closed pore shown in (a).

with the film porosity λ and μ_{O_2} ($= 2\mu_O$) and c_{O_2} ($= c_O/2$) being the chemical potential and concentration of O_2, respectively. By optimizing λ with a least-squares method, it is possible to estimate the volume fraction of closed porosity contributing to a measured capacitance peak.

This was done for both of the above described degradation cases, *i.e.* for an annealed porous electrode and for a poly/dense electrode after applying high anodic bias voltage: Figure 3.16 displays the experimentally obtained capacitances and the fit results for these two cases. The green solid fit lines represent the sum of i) the extrapolation of the defect-related chemical capacitance at low overpotentials and ii) the numerically determined capacitance according to Equation (3.12) with pressure and fugacity coefficient values from the Soave-Redlich-Kwong real gas equation[77,81]. A more detailed description of this model calculation and the associated real gas equation is provided in the Appendix. Both calculated curves predict the capacitance increase and the shift of the capacitance peak to higher overpotentials with increasing measurement temperature extremely well, which supports our suggestion of high pressure oxygen formation and storage in closed pores being the responsible mech-

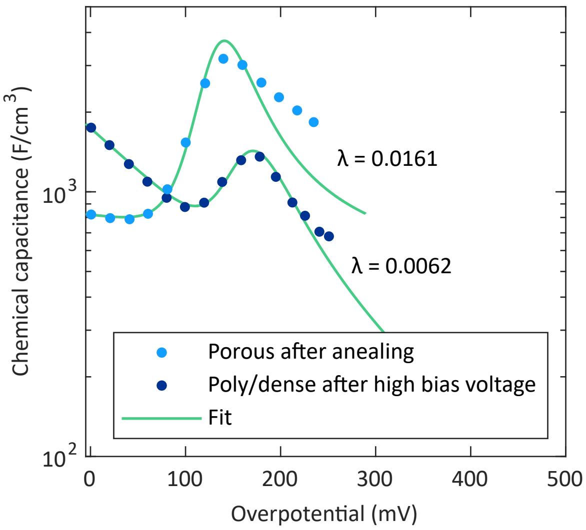

FIGURE 3.16: Chemical capacitance curves of a porous electrode after annealing for 11 h at 460 °C and a poly/dense electrode after applying U_{DC} = 1000 mV for 1 h at 608 °C. The green solid line represents the sum of the extrapolation of the capacitance at low overpotentials and the calculated capacitance according to Equation (3.12). Closed porosity values (λ) from the optimization are given for both electrodes.

anism. Deviations at high overpotentials for the porous electrode may be ascribed to some errors in determining the overpotential of the porous electrode at higher bias voltages due to an increase of intermediate frequency features (see above) or to some leaks in the closed pores which lowers the true fugacity.

Based on the employed real gas equation, we find pressure values up to about 10^4 bar. Obviously, closed pores seem to endure enormous mechanical gas pressures. Even pores which were closed by a $SrSO_4$ phase can apparently withstand such high gas pressures, as capacitance peaks of an annealed porous electrode were almost identical when cycling up to an overpotential of 385 mV and subsequently down to 0 mV (see Figure 3.7). Hence, the capping $SrSO_4$ phase seems to have high mechanical stability at the surface of LSC films. The model calculation yields porosity values of $\lambda = 0.0161$ for the porous and $\lambda = 0.0062$ for the poly/dense electrode, respectively. Accordingly, such electrochemical measurements may be used as an online non-destructive observation tool for detecting the formation of closed pores caused by degradation phenomena at an early stage and allows determining closed porosity with high sensitivity. A detection limit of $\lambda \approx 5 \times 10^{-4}$ for porous and $\lambda \approx 2 \times 10^{-3}$ for dense electrodes can be estimated based on the data in Figure 3.16. Please note that the detection limits vary between the sample types due to the different slopes at low overpotentials, *i.e.* for steeper slopes higher porosity values are required to identify peaks in the chemical capacitance curve.

3.6 Conclusion

Impedance spectroscopy was used to analyze the chemical capacitance of LSC thin film microelectrodes with different microstructures under varying anodic bias voltages. The pristine films exhibit a decrease of the chemical capacitance with increasing anodic overpotential as expected from the decrease of the oxygen vacancy concentration in this regime. However, different types of pre-treatments cause severe changes from this behavior, with an increase of the chemical capacitance under anodic overpotentials and a very pronounced capacitance peak at 150 mV in air at 460 °C. Different oxygen partial pressures and temperatures shift the peak positions in accordance with Nernst's equation. The first type of pre-treatment causing a capacitance peak simply consists of annealing electrodes with open inner surfaces (pores or cracks) for a few hours between 460 and 630 °C in synthetic air. After such an annealing step, these electrodes exhibit a capacitance peak which hardly changes by its monitoring under bias itself. The second type of pre-treatment involves application of high anodic bias corresponding to electrode overpotentials >400 mV. Following such a bias treatment, even polycrystalline dense electrodes without open inner surfaces show a peak of the chemical capacitance. These peaks are very similar to those found for porous electrodes which were intentionally capped with a dense layer already during the fabrication process. There, high-pressure oxygen gas formed in closed pores and high fugacity coefficients of the corresponding real gas are the reasons for the chemical capacitance peak.

Formation of closed pores is also the reason behind the capacitance peaks found in annealed and bias-treated films. ICP-MS, AFM and *in situ* NAP-XPS measurements suggest that annealing in synthetic air leads to the closure of already existing open pores or cracks due to Sr segregation and the formation of a $SrSO_4$ phase on the surface of the respective films. Furthermore, TEM and EDX measurements revealed the formation of closed pores in dense electrodes as a result of bias-induced morphological changes in the bulk of these films. Model calculations based on a real gas equation agree well with experimental data, implying that pressures up to 10^4 bar may develop in closed pores formed due to the described degradation phenomena. Moreover, such model calculations allow to determine the amount of closed porosity in the measured films (in the range of 1 % in our case). An even much lower detection limit can be estimated and thus such capacitance measurements may also be employed as a non-destructive online measurement tool to identify possibly destructive loads in SOEC systems at an early stage.

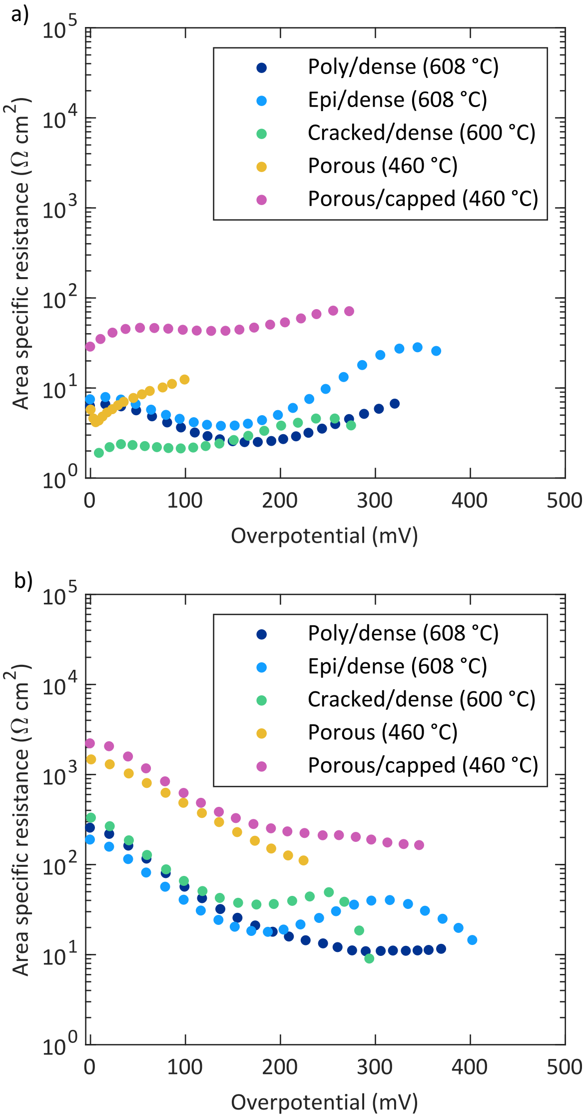

FIGURE 3.17: Surface exchange resistance R_s as a function of the electrode overpotential of pristine (a) and annealed (b) electrodes of all different sample types.

3.7 Appendix

3.7.1 Surface exchange resistance

The surface exchange resistances R_s of pristine and annealed electrodes of all investigated sample types are depicted in Figure 3.17 as a function of the respective electrode overpotentials. Please note that R_s was determined from fitting with the equivalent circuit shown in Figure 4a. As described in the main text, this fitting procedure yielded reasonable C_{chem} and thus also R_s values as long as the low frequency arc represented the major part of the respective spectrum. Hence, R_s values are not available over the same overpotential range for all different sample types.

In the pristine state almost all electrodes exhibit a slight increase of R_s at low overpotentials which may be explained by a thermally induced degradation[62,64,88]. At overpotentials >30 mV, R_s decreases or is almost constant, indicating that apart from the thermal degradation there is a bias related activation, in accordance with literature[56]. Interestingly, at high overpotentials (>150 mV) the resistance increases again. The behavior of the pristine porous electrode differs from the other sample types, which could be caused by crystallisation effects. Please note that R_s of porous electrodes is much lower ($R_s < 0.1\,\Omega\mathrm{cm}^2$) when measured at the same temperature as dense electrodes (608 °C). For all sample types the R_s values at open circuit conditions increase by several orders of magnitude after annealing for several hours in synthetic air. The surface exchange resistances of all annealed electrodes decrease with increasing overpotential up to about 175 mV. At higher overpotentials, R_s curves increase or stay almost constant.

3.7.2 Chemical capacitance during and after long-term annealing

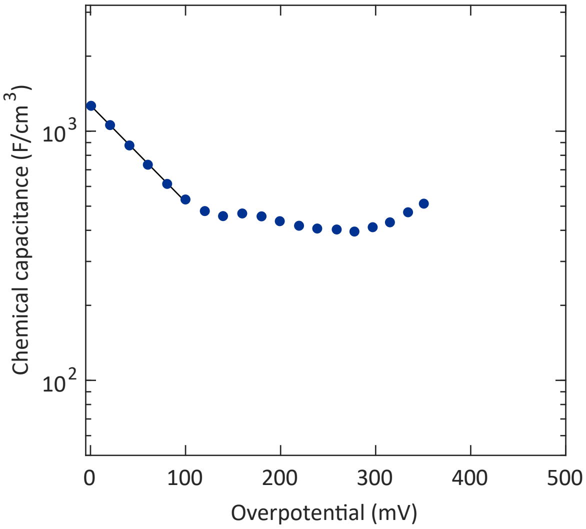

Figure 3.18: Chemical capacitance of a poly/dense electrode after annealing for 507 h at 608 °C and corresponding fits (solid line).

Figure 3.18 displays the chemical capacitance of a poly/dense electrode which was annealed for 507 h at 608 °C prior to the measurement. There is no distinct chemical capacitance peak visible after this long annealing time. Figure 3.19 shows the chemical capacitance and the respective overpotential of a poly/dense electrode as a function of time while a constant application of $U_{DC} = 200$ mV. At the beginning there is a decrease of the chemical capacitance due to an increase of the corresponding overpotential. In the course of the measurement the overpotential levels off at about 195 mV. The chemical capacitance shows no significant increase and remains almost constant after 150 h.

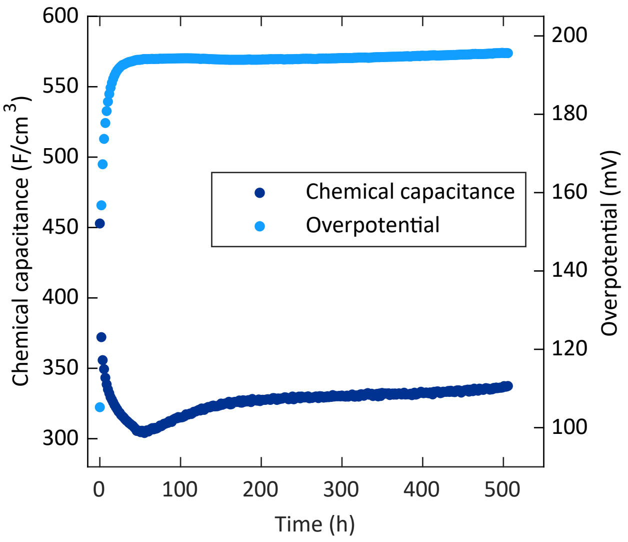

FIGURE 3.19: Chemical capacitance and overpotential of a poly/dense electrode over time while applying anodic bias voltage of U_{DC} = 200 mV at 608 °C.

3.7.3 *In situ* near ambient pressure X-ray photoelectron spectroscopy

Figure 3.20 shows the setup used for the *in situ* near ambient pressure X-ray photoelectron spectroscopy (NAP-XPS) measurements. The onset of the chemical capacitance peak of an annealed porous electrode is shifted by about 80 mV due to the different atmospheres in the *ex situ* (syn. air) and *in situ* NAP-XPS measurement ($p^{at}_{O_2}$ =1 mbar), see Figure 3.21a. This is in line with the value calculated from Nernst's equation (84 mV).

The O 1s spectra depicted in Figure 3.21b were fitted to three components representing "bulk" oxygen (528.5 eV) and a surface-related oxygen component ((531.5 eV), denoted as O 1s surf). The third fitting component is not a chemically distinct oxygen species, but is rather needed to parametrise the asymmetric nature of the O 1s "bulk" signal. In literature this third component was discussed either as a second bulk species[95], or as oxygen in the perovskite termination layer[97]. However, depth profiling by variation of photon energy revealed no significant surface enrichment of this species[95] and it does not seem to change much with the intensity of the S 2p species (see main text). Consequently, we propose a third interpretation: The asymmetric peak shape may be ascribed to the metal-like electronic structure of LSC[73,75]. Since the partly filled conduction band is primarily a hybridization of O 2p and Co 3d states, it is reasonable that the oxygen and cobalt species exhibit a metal-like asymmetry, while the Sr 3d components are symmetric. This interpretation is also in line with the observations of a previous comparative XPS study of different perovskite-type materials.[95] Therein, an asymmetric O 1s bulk peak was only observed for materials with metallic or near-metallic electronic structure.

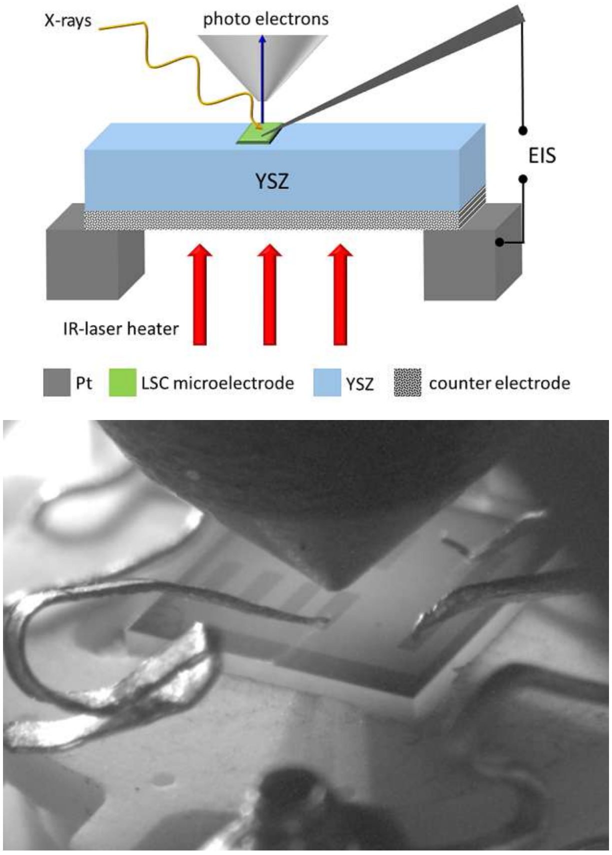

FIGURE 3.20: Sketch (top) and picture (bottom) of the NAP-XPS setup used in this study.

3.7.4 Transmission electron microscopy

Figure 3.22 shows a bright field transmission electron microscopy (BF-TEM) image of a closed pore in the bulk of a poly/dense film after applying 750 mV for 1 h.

3.7.5 Porosity estimation based on a real gas model

In accordance with a recent study[81], we present a detailed model explaining and quantifying the observed chemical capacitance peaks. The build-up of high O_2 gas pressures in closed pores is suggested to cause this capacitive peaks. However, as described in the main text, overpotentials between 150 and 250 mV correspond to effective oxygen partial pressures $p_{O_2}^{WE,eff}$ between 2.8×10^3 and 1.6×10^6 bar. The latter value is far beyond the limits of ideal gas behavior. Therefore, in order to determine the O_2 pressure values in closed pores $p_{O_2}^{pore}$ we have to consider real gas behavior. Here we use the Soave-Redlich-Kwong (SRK) equation of state[77] to calculate $p_{O_2}^{pore}$:

$$p_{O_2}^{pore} = \frac{RT}{V_{O_2} - b} - \frac{a\alpha}{V_{O_2}(V_{O_2} + b)} = \frac{RT}{\frac{1}{c_{O_2}} - b} - \frac{a\alpha}{\frac{1}{c_{O_2}}(\frac{1}{c_{O_2}} + b)} \quad , \tag{3.13}$$

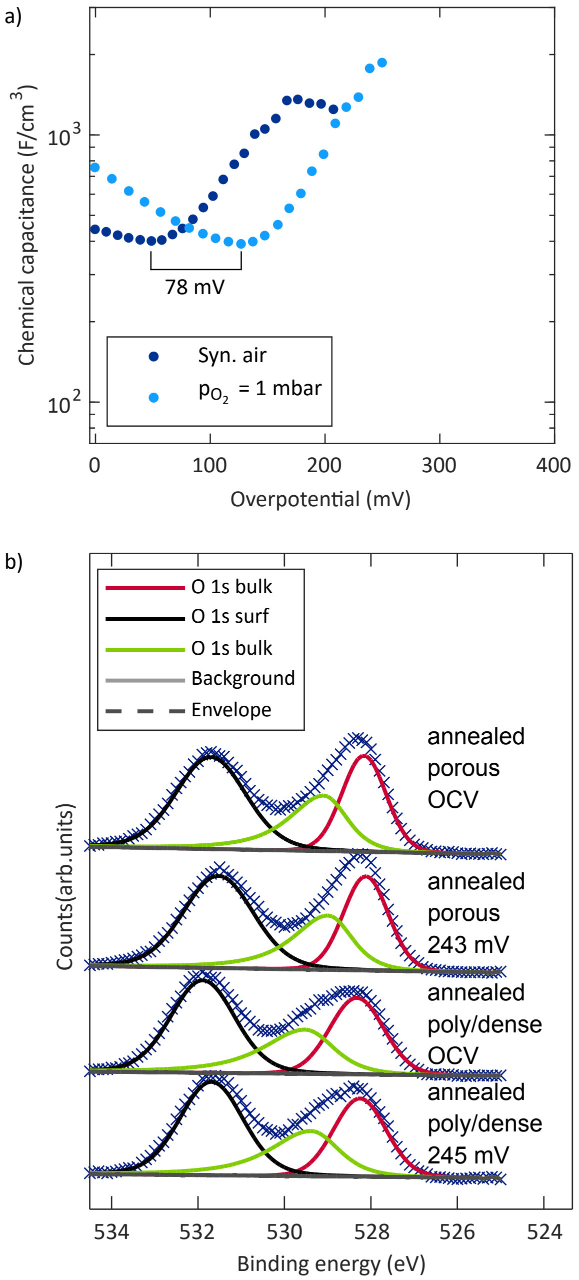

Figure 3.21: (a) Chemical capacitance of an annealed porous electrode as a function of electrode overpotential, measured *ex situ* at 460 °C in synthetic air and at 1 mbar oxygen partial pressure. (b) O 1s spectra of poly/dense and porous electrodes at OCV and anodic overpotentials at which the chemical capacitance peak occurs (counts marked by blue crosses). Measurements were conducted at 1 mbar oxygen pressure and 460 °C.

$$a = \frac{0.42747 \cdot R^2 T_c^2}{p_c} \quad , \tag{3.14}$$

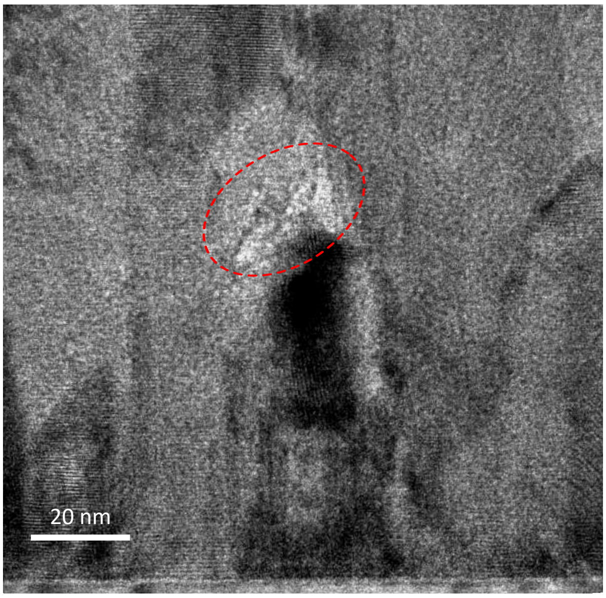

Figure 3.22: BF-TEM image of a poly/dense electrode after applying 750 mV for 1 h revealing a closed pore in the bulk of the film (marked with dashed red line).

$$b = \frac{0.08664 \cdot RT_c}{p_c} \quad , \tag{3.15}$$

$$\alpha = (1 + (0.480 + 1.574 \cdot \omega_a - 0.176 \cdot \omega_a^2) \cdot (1 - \sqrt{T/T_c}))^2 \quad , \tag{3.16}$$

where V_{O_2} and c_{O_2} stand for the molar volume and the concentration of O_2, respectively. R is the universal gas constant and T is the notation for the temperature. Moreover, T_c =154.6 K and p_c =50.46 bar denote the critical temperature and critical pressure of O_2[78], respectively. The temperature dependent term α involves the acentric factor of O_2, *i.e.* $\omega_a = 0.022$, which considers the influence of intermolecular forces depending on the orientation of the molecule.[78] In order to calculate the chemical capacitance of a real gas $C_{chem}^{gas,real}$, we also have to determine the fugacity coefficient φ. According to the Soave-Redlich-Kwong (SRK) equation φ can be calculated as follows

$$\varphi = \frac{f_{O_2}}{p_{O_2}^{pore}} = Z - 1 - \ln\left(Z - \frac{bp_{O_2}^{pore}}{RT}\right) - \frac{a}{bRT} \cdot \ln\left(1 + \frac{bp_{O_2}^{pore}}{ZRT}\right) \quad , \tag{3.17}$$

with f_{O_2} being the fugacity of O_2 and Z denoting the compressibility factor which is defined as

$$Z = \frac{p_{O_2}^{pore}}{c_{O_2}RT} \quad . \tag{3.18}$$

Then, the chemical capacitance of the real gas in closed pores can be determined:

$$C_{chem}^{gas,real} = 16F^2\lambda V \cdot \left(\frac{\partial \mu_{O_2}}{\partial c_{O_2}}\right)^{-1} = 16F^2\lambda V \cdot \left(\frac{\partial\left(\mu_{O_2}^{0,T} + RT\ln\left(\frac{\varphi p_{O_2}^{pore}}{1\,\mathrm{bar}}\right)\right)}{\partial c_{O_2}}\right)^{-1}$$

$$= \frac{16F^2\lambda V}{RT} \cdot \left(\frac{\partial\left(\ln\left(\frac{\varphi p_{O_2}^{pore}}{1\,\mathrm{bar}}\right)\right)}{\partial c_{O_2}}\right)^{-1} , \qquad (3.19)$$

where λ denotes the film porosity, *i.e.* the volume fraction of closed pores with respect to the entire film volume V. With the values for $p_{O_2}^{pore}$ and φ obtained from Equations (3.13) and (3.17), respectively, $\frac{\partial \mu_{O_2}}{\partial c_{O_2}}$ in Equation (3.19) was calculated numerically. To be able to fit our experimental data to Equation (3.19), the overpotential in the working electrode η_{WE} with respect to the oxygen partial pressure in synthetic air is related to the fugacity of the real gas equation as follows

$$\eta_{WE} = \frac{RT}{4F} \cdot \ln\left(\frac{f_{O_2}}{0.21\,bar}\right) = \frac{RT}{4F} \cdot \ln\left(\frac{\varphi p_{O_2}^{pore}}{0.21\,\mathrm{bar}}\right) \quad . \qquad (3.20)$$

Figure 3.23 shows the experimentally obtained volume specific chemical capacitance of a poly/dense electrode after applying $U_{DC} = 1000\,\mathrm{mV}$ for 1 h at 608 °C. In order to fit this experimental data, we also have to consider the defect-related chemical capacitance C_{chem}^{defect}, which is predominant at low overpotentials. As described in the main text, this contribution can be calculated as follows

$$C_{chem} \approx \frac{4F^2 V c_V^{at}}{RT} \cdot \exp\left(\frac{-\alpha F \eta_{WE}}{RT}\right) \quad . \qquad (3.21)$$

A corresponding fit of the experimental chemical capacitance data up to the minimum at about 100 mV yields an exponential factor of $\alpha = 0.56$. This fit and the associated extrapolation to higher overpotentials is shown in Figure 3.23. Additionally, the capacitance contribution of O_2 in closed pores $C_{chem}^{gas,real}$, which was calculated according to Equation (3.19), is depicted in Figure 3.23 (purple dashed line). The corresponding porosity value $\lambda = 0.0062$ for $C_{chem}^{gas,real}$ was determined from a least-squares optimization of the sum of the two capacitance contributions, *i.e.* $C_{chem} = C_{chem}^{defect} + C_{chem}^{gas,real}$ (green solid line in Figure 3.23), to the experimental capacitance data.

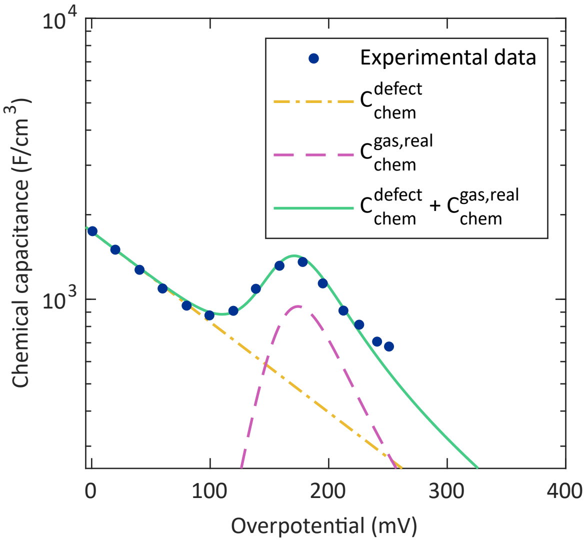

FIGURE 3.23: Experimental chemical capacitance data of a poly/dense electrode after applying $U_{DC} = 1000$ mV for 1 h at 608 °C. The orange dash-dotted line illustrates the fit and the corresponding extrapolation of the defect-related chemical capacitance C_{chem}^{defect}. The purple dashed line represents the chemical capacitance of O_2 in closed pores $C_{chem}^{gas,real}$ according to the real gas model of Equation (3.19). The green solid line shows the sum of the defect-related extrapolation and the capacitance of the real gas.

4 Utilizing Oxygen Gas Formation in Rechargeable Oxygen Ion Batteries

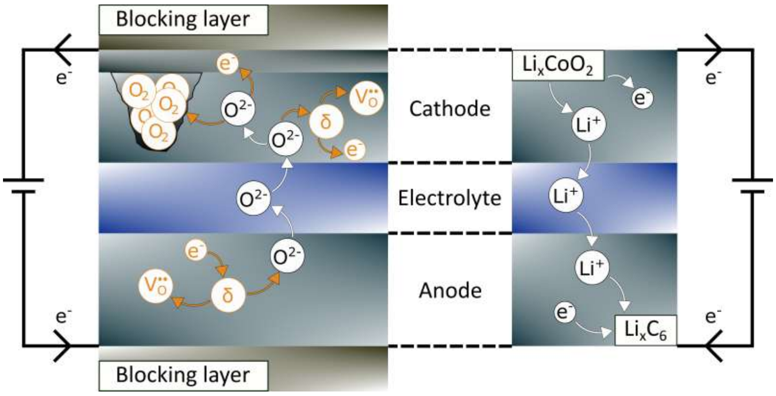

The study presented in this paper will be submitted as an article with the following authors: Krammer, M.; Schmid, A.; Kubicek, M.; Fleig, J.

4.1 Introduction

Rechargeable (secondary) batteries, most commonly in the form of lithium ion batteries (LIBs) are omnipresent in our everyday life as they represent an important component of portable consumer electronics. In addition, such batteries play a major role for electric vehicles and may also be interesting for stationary large to small scale energy storage applications.[103–109] However, due to safety issues[110] as well as concerns about the availability and environmental impact of materials used for current commercial LIBs[111–114], great efforts are devoted to develop other battery technologies either based on cations (e.g. Na, Mg, Al) or on anions (e.g. F, Cl)[115–117].

Recently, a new type of battery based on oxygen ions was developed, in which materials typically used in solid oxide fuel cells (SOFCs) and solid oxide electrolysis cells (SOECs) were employed: Y_2O_3-doped ZrO_2 (YSZ) electrolytes with electrodes consisting of mixed ionic electronic conducting (MIEC) perovskite-type oxides such as $La_{0.6}Sr_{0.4}FeO_{3-\delta}$, $La_{0.5}Sr_{0.5}Cr_{0.2}Mn_{0.8}O_{3-\delta}$ and $La_{0.9}Sr_{0.1}CrO_{3-\delta}$ were tested as model cells.[118] These and similar MIEC materials are characterized by their ability to change the oxygen nonstoichiometry according to the prevailing chemical potential of oxygen.[54,55,71–76,87,119,120] Experimentally the chemical potential of oxygen can either be changed by varying the prevailing oxygen partial pressure or by applying a voltage. For MIEC electrodes, the change of the oxygen nonstoichiometry can be monitored in AC impedance measurements by analyzing the chemical capacitance, which is defined as follows[58]

$$C_{chem}^{defect} = 4F^2V \cdot \left(\frac{\partial \mu_O}{\partial c_O}\right)^{-1} \quad . \tag{4.1}$$

Accordingly, C_{chem}^{defect} is determined by the derivative of the oxygen chemical potential μ_O with respect to the concentration of oxygen c_O and scales with the electrode's volume V (F denotes the Faraday constant).

As described in the previous chapters, MIEC electrodes are commonly applied as oxygen electrodes in SOECs. Furthermore, it was explained that oxygen may be produced inside those cells leading to a build-up of internal pressure and mechanical stress, which in turn can cause pores and cracks or even delamination of the anode from the electrolyte.[28,41,43–52,121] Chapters 2 and 3 demonstrated that this internal pressure build-up may manifest itself as a capacitance maximum under anodic polarization (*i.e.*, in the SOEC mode). Hence, the approach of Equation (4.1) to describe a defect-related chemical capacitance can be extended to the chemical capacitance of the gas phase according to

$$C_{chem}^{gas} = 16F^2V \cdot \left(\frac{\partial \mu_{O_2}}{\partial c_{O_2}}\right)^{-1} \quad , \tag{4.2}$$

with μ_{O_2} ($= 2\mu_O$) and c_{O_2} ($= c_O/2$) being the chemical potential and the concentration of O_2, respectively. It was further shown that those closed pores may remain stable even at mechanical pressures above 1 kbar.

In this study, we use the nonstoichiometry of MIECs as well as the formation of O_2 in closed pores to store oxygen in electrodes of oxide ion battery systems. For this purpose, porous $La_{0.6}Sr_{0.4}CoO_{3-\delta}$ (LSC) thin film electrodes were prepared with a dense ZrO_2 blocking layer on top to prevent oxygen exchange with the measurement atmosphere. Half cells were characterized by AC impedance spectroscopy and galvanostatic cycling with potential limitation. The above described charge storage mechanisms were identified by comparing charge/voltage curves from galvanostatic cycling with the chemical capacitance obtained from impedance spectra and model calculations. Furthermore, full oxygen ion batteries consisting of a porous LSC cathode and a dense $La_{0.9}Sr_{0.1}CrO_{3-\delta}$ (LSCr) anode were fabricated and probed using galvanostatic cycling. In such cells the lower reducibility of LSCr compared to LSC was utilized to realize a battery system, where charge can be reversibly stored by pumping oxygen from the anode to the cathode and vice versa.

4.2 Experimental

4.2.1 Sample preparation

All samples are based on yttria-stabilized zirconia (YSZ) single crystal electrolytes (5 × 5 × 1 mm^3, (100)-oriented, 9.5 mol % Y_2O_3; CrysTec, Germany). A reference electrode was fabricated by brushing Pt paste into a notch (0.3 × 0.3 × 1 mm^2) which was carved around the circumference of the single crystal, followed by sintering at 1200 °C for 2 h in air. The current collectors of working and counter electrodes were prepared from Pt layers of 100 nm thickness, which were sputter-deposited on both sides of the YSZ single crystal. 5 nm thick Ti, deposited beneath the Pt, ensured a proper adhesion. These Ti/Pt layers were then microstructured by photolithography and ion beam etching, resulting in a grid with strips of 15 µm width and 35 × 35 $µm^2$ free squares.

In the next step, mixed conducting oxide thin film electrodes were prepared via pulsed laser deposition (PLD) using a KrF excimer laser (248 nm; Compex Pro 201F, Coherent, Germany). For half cell measurements, porous $La_{0.6}Sr_{0.4}CoO_{3-\delta}$ (LSC) counter electrodes were deposited at a substrate temperature of 450 °C and at an oxygen partial pressure of 0.4 mbar. Previous studies[59,60] demonstrated that LSC electrodes deposited with these parameters exhibit very fast oxygen exchange kinetics due to their nanoporous microstructure. The working electrodes of the half cells consisted of a porous LSC layer with a thickness of about 50 nm, deposited by means of the same parameters as used for the counter electrodes. Then the deposition parameters were changed to 600 °C and 0.04 mbar oxygen partial pressure in order to deposit a dense LSC capping layer (about 20 nm thickness) on top of the porous LSC working electrode layer. Transmission electron microscopy images and inductively coupled plasma mass spectrometry measurements of a previous study[81] show that such a dense capping layer indeed closes the nanometer-sized open pores of the layer underneath. For the deposition of these half cell working electrodes, a shadow mask was used, resulting in an electrode area of about 4.15 × 4.15 × mm^2. Finally, a dense ZrO_2 layer with a thickness of about 1 µm was deposited on top with a slightly larger shadow mask, thus covering the entire working electrode and isolating it from the outer atmosphere.

Full oxygen ion batteries consisted of an LSC cathode as described above and a dense $La_{0.9}Sr_{0.1}CrO_{3-\delta}$ (LSCr) anode with a thickness of about 470 nm. In this case, both electrodes were covered with a ZrO_2 blocking layer. The deposition parameters for all different electrodes and layers can be found in Table 4.1. The LSC and LSCr target pellets for PLD were prepared via a Pechini synthesis using the following metal precursors: $SrCO_3$, La_2O_3, Co, $Cr(NO_3)_3$ (all >99.995 %, Sigma Aldrich, USA). After the synthesis, the obtained powder was calcined for 10 h at 800 °C in air and pressed to a pellet form by cold isostatic pressing (300-310 MPa). Finally, the pellet was sintered for 12 h at 1200 °C in air. X-ray diffraction was used to check the phase purity of the targets.

Table 4.1: Deposition parameters for the five different sample types investigated in this study.

Sample type	Temperature (°C)	Oxygen partial pressure (mbar)	Laser fluence (J/cm^2)
LSC counter electrode	450	0.4	1.4
LSC working electrode (porous)	450	0.4	1.4
LSC working electrode (dense)	600	0.04	1.1
LSCr anode	600	0.015	1.1
ZrO_2 blocking layer	700	0.015	1.1

4.2.2 Electrochemical measurements

Electrochemical measurements on half cells and on full oxygen ion batteries were performed in an atmosphere containing oxygen at a partial pressure of 0.25 mbar and at temperatures between 350 and 460 °C. The samples were placed in a fused silica apparatus inside a tube furnace to heat the samples symmetrically. Temperatures were determined using a type S thermocouple located within 1 cm from the sample. The top electrode was contacted by means of a platinum-rhodium needle, which was placed onto the current collector close to the edge of the YSZ single crystal. The bottom electrode of each cell was contacted by placing the sample onto a platinum mesh. A fine platinum wire was wrapped around the notch to ensure electrical contact of the reference electrode. Prior to each electrochemical measurement, all electrodes were connected at the respective measurement temperature. This led to equilibration of all electrodes with the ambient atmosphere and thus defined the initial oxidation state.

Electrochemical impedance spectroscopy (EIS) was performed in half cell geometry using an Alpha-A High Performance Frequency Analyzer and an Electrochemical Test Station POT/GAL 30 V/2 A (both: Novocontrol, Germany) in a frequency range of 10^6 to 10^{-3} Hz with 5 data points per decade. An AC root-mean-square voltage of 10 mV was employed with superimposed DC bias voltages ranging from 0 to 600 mV. DC voltages were applied between the working and the reference electrode and DC currents were measured between the working and the counter electrode. Before starting the actual impedance measurement, the same DC bias voltage was applied for ca. 4.5 h to warrant a time-independent charging state of the working electrode.

Galvanostatic cycling with potential limitation (GCPL) was done with a Keithly 2600 source meter in 4-wire configuration with currents from 0.5 to 20 µA. For half cells, DC currents were applied between the counter and the working electrode and voltages were measured between the working and the reference electrode. Thus, the voltage of the working electrode was determined with respect to 0.25 mbar oxygen since the reference electrode was in equilibrium with the measurement atmosphere. During full cell cycling, voltages were measured between working and counter electrode as well as between working and reference electrode. Please note that in this work all potentials are plotted with respect to 1 bar oxygen partial pressure.

4.3 Results and discussion

4.3.1 Impedance spectroscopy of $La_{0.6}Sr_{0.4}CoO_{3-\delta}$ half cells

Figure 4.1 depicts exemplary impedance spectra of half cell measurements, recorded in 0.25 mbar oxygen partial pressure with different superimposed anodic DC bias voltages. The potentials Φ given for each spectrum are calculated via Nernst's equation with respect to 1 bar oxygen according to

$$\Phi = \frac{RT}{4F} \cdot \ln\left(\frac{p_{O_2}}{1\,\text{bar}}\right) + U_{DC}, \tag{4.3}$$

with p_{O_2} being the oxygen partial pressure of the measurement atmosphere (*i.e.*, 0.25 mbar) and U_{DC} the DC bias voltage between working and reference electrode. R, T and F are the usual symbols for the universal gas constant, the temperature and Faraday's constant, respectively. The potential Φ thus represents the charging state of the LSC electrode, provided that any leakage current is sufficiently small, see below. All impedance spectra measured in this study exhibit a semicircle at high frequencies (see A in insets of Figure 4.1). This feature decreases with increasing temperature (see Figure 4.1c) but shows no dependence on the applied DC bias voltage. In accordance with previous studies[56,65,122], its resistance is thus attributed to the ionic transport resistance of the YSZ electrolyte R_{YSZ}. This resistance was determined by an extrapolation of A to the x-axis of the Nyquist plot. Furthermore, the insets in Figure 4.1 also show that a smaller semicircular feature (B) at intermediate frequencies is obtained for all spectra, which may be associated with interfacial processes between the LSC working electrode and the YSZ electrolyte.[56] This contribution generally increases with increasing anodic potential and decreasing temperature, in agreement with a former study on $La_{0.6}Sr_{0.4}Co_{0.8}Fe_{0.2}O_{3-\delta}$ thin film electrodes[56]. In addition, a shoulder (C) appears in all impedance spectra ranging from about 1.6 Hz to 10 mHz at 460 °C which may be caused by the lateral diffusion of oxygen ions to those parts of the LSC film that are located on top of the current collector. This preliminary interpretation is based on additional measurements showing that such a shoulder is not encountered when probing half cells with a current collector applied on top of the LSC working electrode (see Figure 4.9 in the Appendix).

A fourth feature (D) becomes apparent at very low frequencies <10 mHz. At low potentials, this feature is predominantly capacitive (see spectrum at $\Phi = -119$ mV in Figure 4.1a). However, with increasing potential, this low frequency feature develops into a semicircle. The values of the corresponding capacitance are rather high, *i.e.* in the order of 10 mF/cm^2.

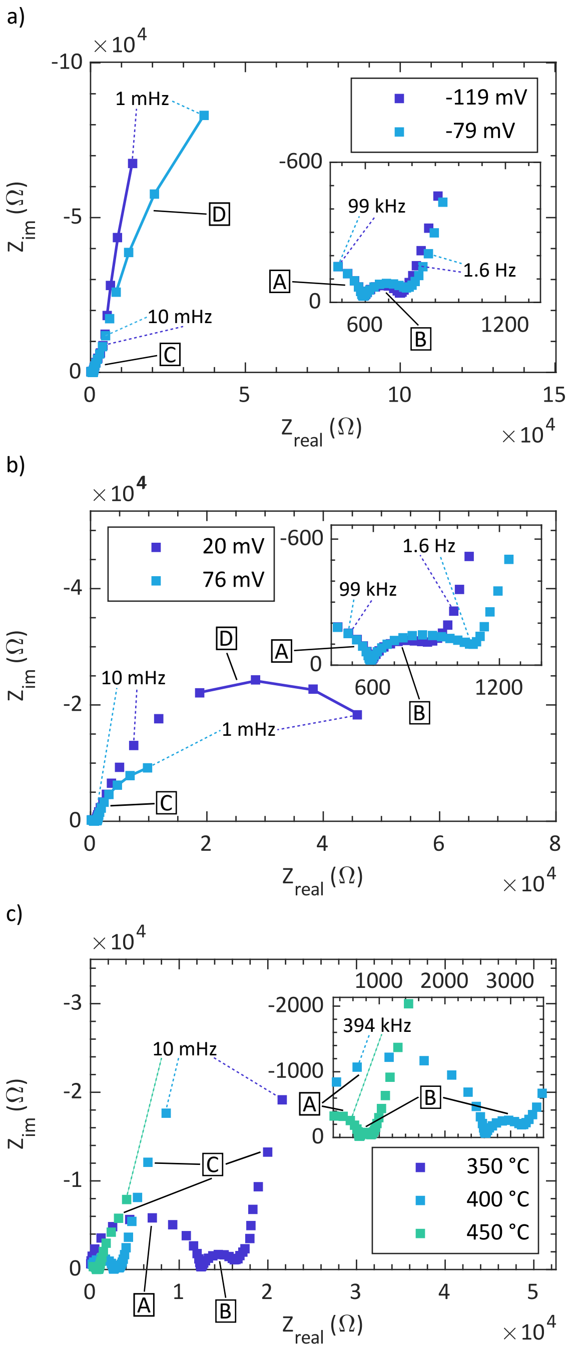

Figure 4.1: Impedance spectra measured at lower (a) and higher (b) potentials Φ (vs. 1 bar O_2), at a temperature of 460 °C and in 0.25 mbar oxygen partial pressure. Lines are fits to the spectra using an equivalent circuit consisting of a serial offset resistance and an R/CPE element. c): Impedance spectra measured at different temperatures in 0.25 mbar oxygen partial pressure without bias voltage, *i.e.* between $\Phi = -0.129$ and -0.111 V.

In agreement with literature on LSC and other mixed conducting oxides[54–56,59,62,66,81,123–125], this capacitive response is attributed to the chemical capacitance of the MIEC electrode C_{chem}.

The resistive contribution of this low frequency feature is ascribed to parasitic current paths, most likely caused by oxygen leakage through the yet non-ideal ZrO_2 blocking layer.[118] This resistance is much smaller for half cells, where the current collector is positioned on top of the LSC film (see Figure 4.9 in the Appendix). Accordingly, the blocking layer seems to be less dense in such a case, leading to an increased oxygen leakage. Consequently, all results presented here correspond to samples with the current collectors underneath the electrode film. As shown in Figure 4.1, the resistance of D gets smaller with increasing potential, *i.e.* with increasing driving force for the oxygen evolution reaction. However, the parasitic currents are low and hardly affect the validity of Equation (4.3), *i.e.* the potential Φ still describes the charging state of the electrode.

A more detailed analysis of the impedance spectra is beyond the scope of this study, only the chemical capacitance behind feature D is of relevance in this paper. Moreover, from the much larger resistance of D compared to all other features, we conclude that oxygen leakage/evolution is DC rate limiting and thus the oxygen chemical potential can be regarded as uniform in the whole electrode. The low frequency feature D was fitted with a parallel connection of a resistance R_s and a constant phase element CPE_{chem}, which considers the non-ideal behaviour of a capacitance. The impedance of a constant phase element is given by

$$Z_{CPE} = \frac{1}{(j\omega)^n Q} \quad , \tag{4.4}$$

where Q and n are fit parameter and ω is the angular frequency. From Q, n and the resistance R_s of a non-linear least-squares fitting, the chemical capacitance C_{chem} can be calculated as follows[70]

$$C_{chem} = (R_s^{1-n} \cdot Q)^{\frac{1}{n}} \quad . \tag{4.5}$$

An additional serial offset resistance R_{offs} in the equivalent circuit considers all other contributions that were described above. This simple equivalent circuit enabled a reasonable analysis of C_{chem}, which is the most important quantity from the impedance measurements regarding charge storage (see mechanistic discussion below).

Figure 4.2 displays the volumetric chemical capacitance of an LSC half cell as a function of electrode potential Φ, determined from fitting the corresponding impedance spectra. Please note that all volumetric half cell quantities were normalized to the volume of the LSC electrode V without subtracting the respective pore volume of the porous layer. At potentials <0 V the chemical capacitance decreases with increasing potential as also observed in former studies on $La_{1-x}Sr_xCo_yFe_{1-y}O_{3-\delta}$ (LSCF) thin film electrodes[54–56]. However, at potentials >0 V the chemical capacitance increases strongly (by almost an order of magnitude between Φ =0 V and Φ =0.076 V), which is also similar to recent works[81,124]. The underlying mechanisms of this chemical capacitance curve is addressed in the mechanistic discussion.

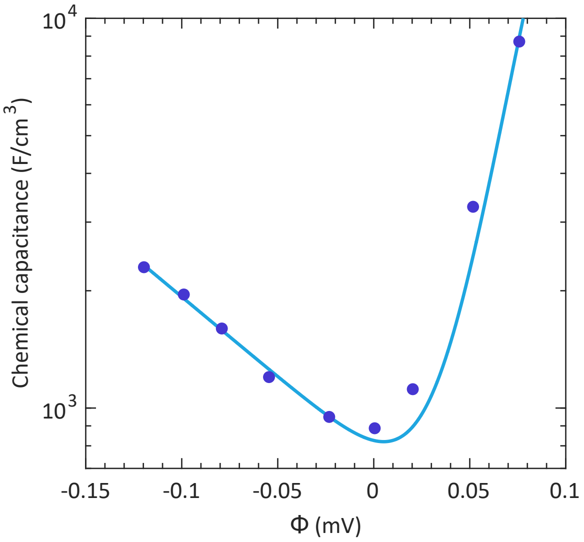

Figure 4.2: Volumetric chemical capacitance vs. potential Φ with respect to 1 bar O_2, determined from impedance spectra recorded at 460 °C in 0.25 mbar O_2 with different anodic DC bias voltages U_{DC}. The solid line represents a fit according to the mechanistic model described in the text.

4.3.2 Galvanostatic cycling of $La_{0.6}Sr_{0.4}CoO_{3-\delta}$ half cells

Half cells were also tested by galvanostatic cycling with potential limitation (GCPL) in order to investigate the capability of porous LSC electrodes to act as oxygen storing cathodes in oxygen ion batteries. Figure 4.3a displays charge/discharge curves of an LSC half cell, measured at 400 °C in 0.25 mbar O_2 with a current of 3 µA/cm^2 over 19 charge/discharge cycles. The half cell is cycled between −0.12 and 0.09 V with respect to 1 bar oxygen. Charge and discharge curves are separated by about 4 mV due to overpotentials attributed to the transport resistance of oxygen ions in the electrolyte (R_{YSZ}) and additional resistances, which might be caused by interfacial and diffusion-related processes (see above). These contributions account for an overpotential of about 2 mV acting in both directions (*i.e.* charge and discharge runs). Charge curves appear to become slightly flatter above 0.07 V, whereas discharge curves do not exhibit such a behavior. In addition, discharge curves show a slightly lower slope at potentials <−0.05 V compared charging.

The corresponding half cell capacities are between 84 and 88 mAh/cm^3 and hardly change for 19 cycles and discharge capacities even slightly increase (see Figure 4.3b, the rates of charging/discharging are in the range of 5 C). Figure 4.3c shows that the initial corresponding coulomb efficiency is around 0.96 and increases to almost 0.99 over the course of the 19 cycles. The small loss of each charge/discharge cycle is probably caused by the yet non-ideal ZrO_2 blocking layer, leading to a tiny leakage of oxygen to the atmosphere.

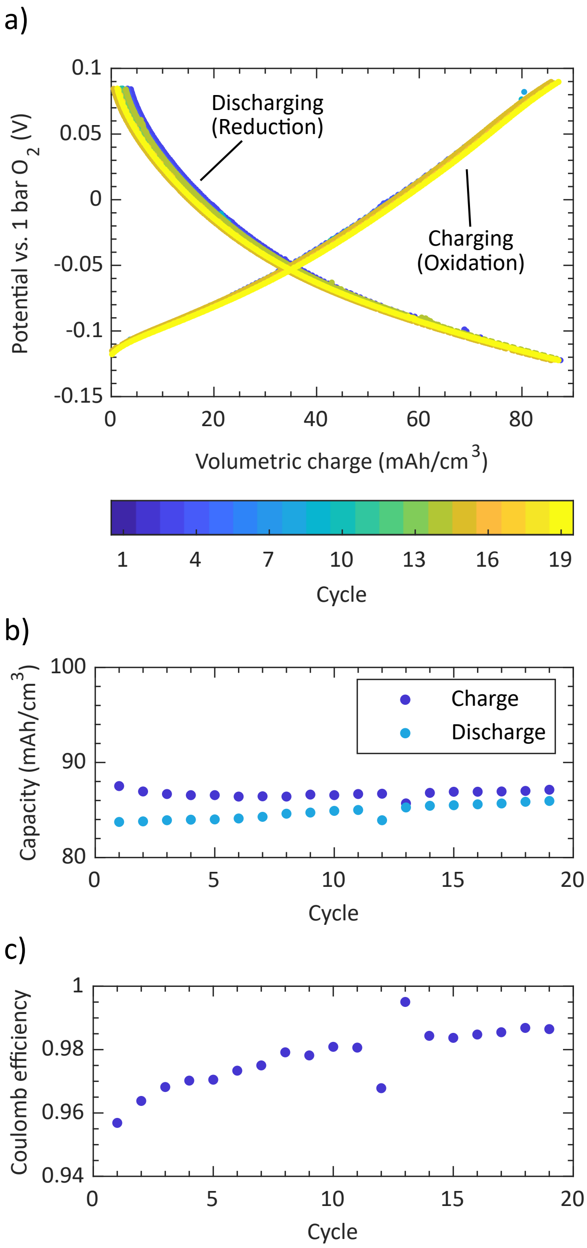

Figure 4.3: (a) Charge/discharge curves over several charge/discharge cycles of an LSC half cell, measured at 400 °C in 0.25 mbar O_2 with a current of 3 μA/cm^2 (ca. 5 C) between $\Phi = -0.12$ and 0.09 V with respect to 1 bar O_2. The very first cycle is not shown. Corresponding half cell half cell capacity (b) and coulomb efficiency (c).

LSC half cells were also probed at a higher temperature of 460 °C. Figure 4.4a shows the corresponding charge/discharge curves over 19 cycles, measured with a current of 116 μA/cm^2. The charge and discharge curves are separated by about 36 mV which is again ascribed to losses in the electrolyte and contributions possibly stemming from interface reactions and lateral diffusion of oxygen ions. Although all resistances related to these three contribu-

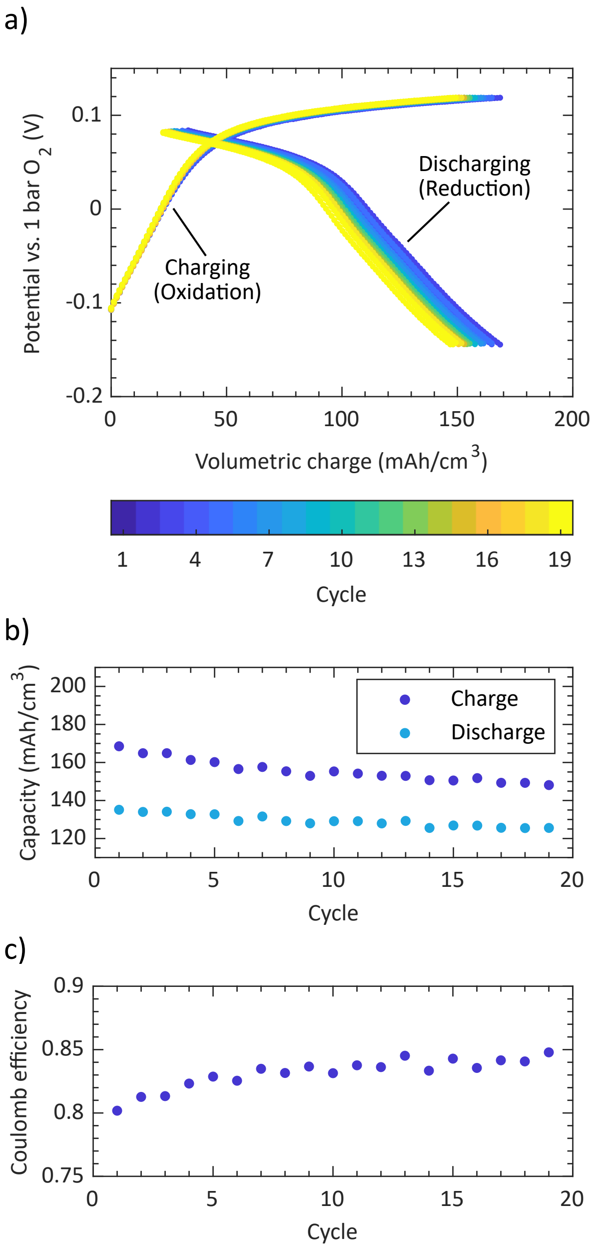

Figure 4.4: Charge/discharge curves over several charge/discharge cycles of an LSC half cell, measured at 460 °C in 0.25 mbar O_2 with a current of 116 µA/cm^2 (between 100 and 135 C) between $\Phi = -0.144$ and 0.119 V with respect to 1 bar O_2. The very first cycle is not shown. Corresponding half cell half cell capacity (b) and coulomb efficiency (c).

tions decrease with increasing temperature (see Figure 4.1c), the overpotential losses are higher compared to the curves at 400 °C (see Figure 4.3a) due to the much higher current (116 µA/cm^2) used for this measurement. Compared to the half cell measurement at lower temperature, charge/discharge curves are significantly flatter at voltages >0.05 V, resulting in a plateau-like characteristic. This plateau also leads to significantly higher discharge capacities of up to about 135 mAh/cm^3 between $\Phi = -0.145$ and 0.085 V (discharge rate of about 125 C) in the first cycle and 126 mAh/cm^3 in the 19th cycle (see Figure 4.3b). However, the increased temperature also causes some capacity losses during each charge/discharge cycle compared to the measurement at 400 °C: Coulomb efficiencies are between 0.8 in the beginning and 0.85 after 19 cycles (see Figure 4.3c). These losses are probably again caused by oxygen leaking through the blocking layer, which seems to be enhanced at higher temperatures. In the next section, we discuss the charge storage mechanisms occurring in these LSC half cells and determining the observed charge/discharge characteristics.

4.3.3 Mechanistic discussion of $La_{0.6}Sr_{0.4}CoO_{3-\delta}$ half cells

In order to understand the charge storage mechanisms in LSC half cells, we have to consider defect chemical-related phenomena of LSC as well as specific features attributed to the porosity of our electrodes. During charging, oxygen from the measurement atmosphere (*i.e.*, $p_{O_2} = 0.25$ mbar) is reduced at the porous LSC counter electrode and the resulting oxygen ions are transported through the counter electrode and the YSZ electrolyte to the LSC working electrode as sketched in Figure 4.5a. There, two charge storage mechanisms may take

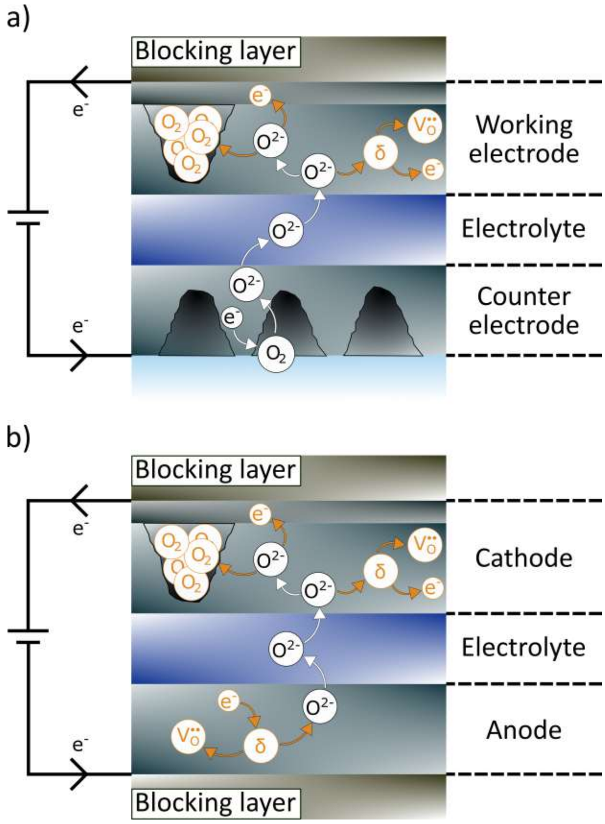

FIGURE 4.5: Sketch of the reactions during charging of an LSC half cell (a) and a full cell consisting of an LSC cathode and an LSCr anode (b).

place, a defect chemical one in the solid and one related to gas formation in pores. We start with discussing the defect chemical oxygen storage, which is similar to Li storage in lithium ion batteries. An oxygen ion battery based on this charge storage principle was recently described in reference 118.

According to this charging mechanism oxygen vacancies $\mathrm{V_O^{\bullet\bullet}}$ in LSC become filled according to

$$\mathrm{O^{2-}_{YSZ} + V_O^{\bullet\bullet} \rightleftharpoons O_O^{\times} + 2\,e^-_{cc} + 2\,h^{\bullet}} \quad . \tag{4.6}$$

Here, $\mathrm{O^{2-}_{YSZ}}$ and $\mathrm{O_O^{\times}}$ refer to oxygen ions in the YSZ electrolyte and in the LSC electrode, respectively. Electrons in the current collector are denoted as $\mathrm{e^-_{cc}}$ and $\mathrm{h^{\bullet}}$ stands for electron holes in LSC. The reverse reaction corresponds to discharging of the LSC half cell which is accompanied by the formation of oxygen vacancies. Consequently, this reaction leads to a change of the oxygen concentration in the electrode c_O. This can be described by the prevailing oxygen chemical potential μ_O and the chemical capacitance C^{defect}_{chem} (see Equation (4.1)). More specifically, in our half cell experiments, the oxygen chemical potential in the working electrode μ_O is altered by applying a voltage U_{DC}, *i.e.* by modifying the potential Φ in Equation (4.3) according to

$$\mu_O = \mu_O^{0,T} + \frac{RT}{2} \cdot \ln\left(\frac{p_{O_2}}{1\,\mathrm{bar}}\right) + 2FU_{DC} = \mu_O^{0,T} + 2F\Phi, \tag{4.7}$$

with $\mu_O^{0,T}$ being the chemical potential of oxygen gas at 1 bar. Hence, a positive DC bias voltage U_{DC} in the impedance measurements increases the oxygen chemical potential μ_O in the LSC working electrode. As frequently demonstrated in literature on LSC and similar mixed conducting perovskites[54,55,71–76,87], this increase of μ_O leads to a decrease of the oxygen vacancy concentration c_V in accordance with the reaction during charging postulated in Equation (4.6). The relation between C^{defect}_{chem}, c_V and the electrode potential Φ becomes clearer when considering a dilute defect model for an acceptor-doped mixed conducting oxide under oxidizing conditions, which leads to the following expression[57]:

$$C^{defect}_{chem} = \frac{F^2V}{RT}\left(\frac{1}{4c_V} + \frac{1}{c_h}\right)^{-1} \quad . \tag{4.8}$$

Consequently, the chemical capacitance C^{defect}_{chem} is primarily determined by the minority charge carrier concentration. In accordance with the known defect chemical model[73,75], we assume that this is the oxygen vacancy concentration c_V rather than the concentration of electron holes c_h for the measurement conditions used here. Thus, we get the relation

$$C^{defect}_{chem} \approx \frac{F^2V}{RT} \cdot 4c_V = \frac{4F^2Vc_V^0}{RT} \cdot \left(\frac{p_{O_2}}{1\,\mathrm{bar}}\right)^{\left(-\frac{1}{2}\right)} = \frac{4F^2Vc_V^0}{RT} \cdot \exp\left(\frac{-\alpha F\Phi}{RT}\right) \quad , \tag{4.9}$$

with $\alpha = 2$ and c_V^0 being the vacancy concentration at an oxygen partial pressure of 1 bar. However, for LSC it was demonstrated that C_{chem}^{defect} deviates from the dilute defect model[55,124] due to its metal-like character[73,75]. As a result, α values between 0.5 and 0.7[55,124] were found for the last term in Equation (4.9). Fitting the chemical capacitance data shown in Figure 4.2 up to about 0 V yielded a similar exponential factor of $\alpha = 0.6$. Thus, we conclude that the decreasing chemical capacitance with increasing potential up to about 0 V is the consequence of the decreasing vacancy concentration.

At potentials >0 V, the chemical capacitance increases significantly with increasing potential (see Figure 4.2). Accordingly, the second charge storage mechanism comes into play, which is also indicated by the flattening of the charge/discharge curve measured at 460 °C (see Figure 4.4a). This second mechanism involves the formation of gaseous O_2 inside closed pores of the LSC working electrode according to

$$2\,\mathrm{O}_{\mathrm{YSZ}}^{2-} \rightleftharpoons \mathrm{O}_2 + 4\,\mathrm{e}_{\mathrm{cc}}^{-} \quad . \tag{4.10}$$

This reaction also leads to a very different model behind the corresponding chemical capacitance as demonstrated in recent studies[81,124]: By calculating pressure values $p_{O_2}^{pore}$ and fugacity coefficients φ from a real gas equation, C_{chem}^{gas} can be numerically determined according to[81,124]

$$\begin{aligned} C_{chem}^{gas} = 16F^2\lambda V \cdot \left(\frac{\partial \mu_{O_2}}{\partial c_{O_2}}\right)^{-1} &= 16F^2\lambda V \cdot \left(\frac{\partial\left(\mu_{O_2}^{0,T} + RT\ln\left(\frac{\varphi p_{O_2}^{pore}}{1\,\mathrm{bar}}\right)\right)}{\partial c_{O_2}}\right)^{-1} \\ &= \frac{16F^2\lambda V}{RT}\cdot\left(\frac{\partial\left(\ln\left(\frac{\varphi p_{O_2}^{pore}}{1\,\mathrm{bar}}\right)\right)}{\partial c_{O_2}}\right)^{-1} \quad . \end{aligned} \tag{4.11}$$

This capacitance contribution scales with the porosity λ, which is the fraction of the volume of closed pores with respect to the entire electrode volume V.

These two charge storage mechanisms may now be combined in a single effective chemical capacitance of LSC, namely $C_{chem} = C_{chem}^{defect} + C_{chem}^{gas}$ consisting of i) the defect related chemical capacitance C_{chem}^{defect} extrapolated from experimental data at low potentials and ii) the numerically calculated chemical capacitance C_{chem}^{gas} using pressure and fugacity coefficient values from the Soave-Redlich-Kwong real gas equation[77]. The green dash-dotted line in Figure 4.2 shows a fit according to this combined chemical capacitance with λ, c_V^0 and α being the only free parameters. This fit yielded a porosity value of $\lambda = 0.194$.

The chemical capacitance C_{chem} corresponds to the differential capacity $dQ/d\Phi$ which is commonly obtained from differentiating galvanostatic charge/voltage curves. Consequently, expected charge/voltage curves can be calculated via the integration of C_{chem} according to

$$Q(\Phi) = \int_0^{\Phi} C_{chem}\, d\Phi \quad . \tag{4.12}$$

Such curves were calculated by performing a cumulative numerical integration of the combined chemical capacitance $C_{chem} = C_{chem}^{defect} + C_{chem}^{gas}$ from the fit in Figure 4.2, and also by directly using the chemical capacitance data displayed in Figure 4.2, which were obtained from AC impedance spectra. Figure 4.6a shows the two resulting charge/voltage characteristics together with a measured discharge curve from the galvanostatic cycling of a half cell at 460 °C, corrected for the overpotential losses described above. The excellent agreement between the measured and the calculated charge/voltage curves strongly supports our model of charge storage in porous LSC electrodes. Only at high potentials $\Phi > 0.06$ V vs. 1 bar O_2 the calculated curve and the data determined from impedance spectra deviate slightly from the measured discharge curve. This may be ascribed to additional overpotentials under such strongly oxidizing conditions. It should be noted, that potentials $\Phi > 0.1$ V (with respect to 1 bar O_2) correspond to very high gas pressure values >500 bar. In the considered specific case, the defect related capacity related to C_{chem}^{defect} from $\Phi = -0.12$ to 0.085 V accounts for 58.5 mAh/cm^3 and hardly increases further for higher voltages due to the low oxygen vacancy concentration at high voltages. The remaining capacity (67 mAh/cm^3) at 0.085 V, *i.e.* about 53 % of the total capacity) originates from oxygen gas in pores, *i.e.* C_{chem}^{gas}. The individual contributions (*i.e.*, C_{chem}^{defect} and C_{chem}^{gas}, respectively) to the calculated charge voltage curve are shown in Figure 4.6b.

Based on this mechanistic understanding, we may now also reconsider the charge/discharge characteristics from galvanostatic cycling measurements. As already addressed above, the charge and discharge curves at 460 °C are significantly flatter at potentials $\Phi > 0.05$ V and thus higher electrode capacities are obtained in comparison to the measurement at 400 °C, where only the onset of a flattening is visible (*cf.* Figures 4.3a and 4.4a). For measurements conducted at 350 °C, not even an onset of a flattening was found (see Figure 4.10a in the Appendix). This plateau-like characteristic of the charge/voltage curve at potentials $\Phi > 0.05$ V is ascribed to the O_2 formation inside closed pores of the LSC working electrode. We can assume that the required oxygen evolution reaction at the LSC surfaces inside closed pores is strongly temperature dependent and becomes much faster at higher temperatures since activation energies related to oxygen exchange of LSC are typically >1 eV[67]. The absence of the gas storage mechanism at lower temperatures is thus most probably due to slow kinetics of the O_2 evolution reaction at temperatures ≤400 °C.[62,126] In principle the storage of high-pressure O_2 may enable enormous capacities by increasing the potential and thus further

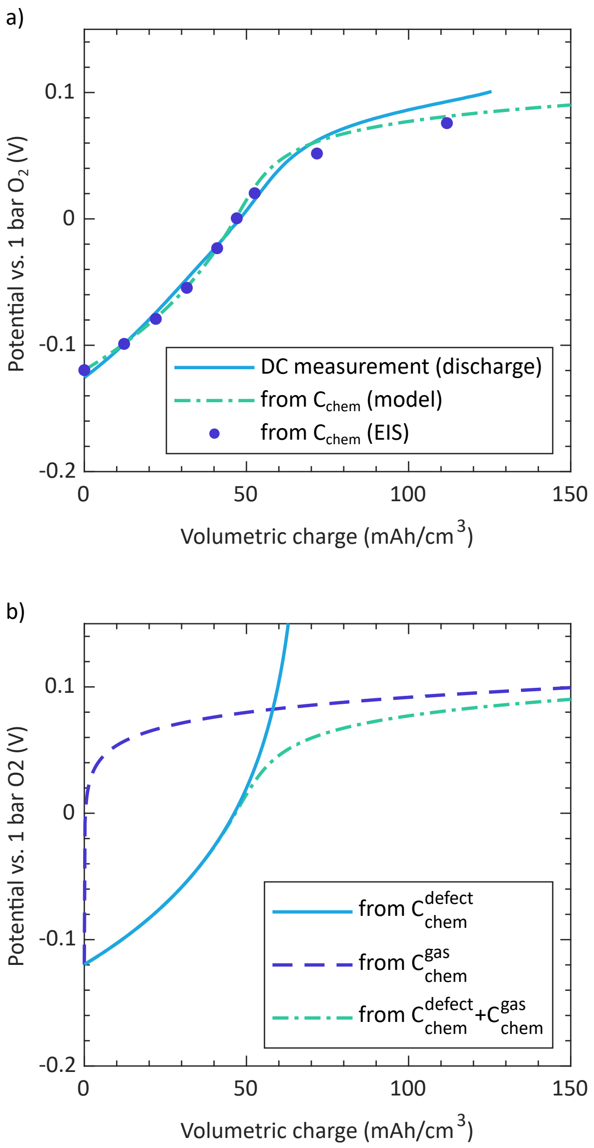

FIGURE 4.6: (a) Charge/voltage curves of an LSC half cell at 460 °C in 0.25 mbar O_2. The blue solid line shows a measured discharge curve from galvanostatic cycling. The purple data points are determined from the chemical capacitance obtained from AC impedance measurements and the green dash-dotted line is the corresponding fit according to Equations (4.9) and (4.11). (b) Individual capacity contributions (determined from the respective chemical capacitances C_{chem}^{defect} and C_{chem}^{gas}) to the combined charge/voltage curve (from $C_{chem} = C_{chem}^{defect} + C_{chem}^{gas}$).

compressing O_2 in closed pores (*i.e.*, 755 mAh/cm^3 at $\Phi = 0.175$ V for a porosity of $\lambda = 0.194$ and even more for higher porosity values). However, potentials $\Phi > 0.175$ V lead to extremely high pressure values >7400 bar, which probably requires an optimized blocking layer.

In general, also the defect-related mechanism can be used to obtain high capacities. In a recent study on similar mixed conducting oxides, values of about 280 mAh/cm^3 were obtained for 40 % Sr content in $La_{1-x}Sr_xFeO_{3-\delta}$[118]. The only moderate capacity due to C_{chem}^{defect} in our study is simply caused by the fact that our LSC electrodes were allowed to equilibrate with the measurement atmosphere (*i.e.*, $p_{O_2} = 0.25$ mbar, T between 350 and 460 °C) prior to each measurement. Hence, the majority of vacancies were already filled with oxygen when starting charging, thus preventing a high capacity gain through this mechanism.

4.3.4 Full oxygen ion batteries

In order to further demonstrate the concept of a battery-system based on oxygen ions, we also investigated full oxygen ion batteries. For this purpose, an LSC electrode as described above was used as a cathode, together with a dense $La_{0.9}Sr_{0.1}CrO_{3-\delta}$ (LSCr) anode, thus utilizing the lower reducibility of $La_{1-x}Sr_xCrO_{3-\delta}$ compared to $La_{1-x}Sr_xCoO_{3-\delta}$.[73,75,119] The general concept of this battery is sketched in Figure 4.5b. The terms cathode and anode refer to reduction (cathode) and oxidation (anode) during discharging. In such a battery, oxygen vacancies of the LSCr anode become filled during discharging, while oxygen vacancies are formed and oxygen gas is removed from pores in the LSC cathode. During charging, oxygen vacancies and pores of the LSC cathode are again filled with oxygen ions and oxygen gas, respectively.

Figure 4.7a shows charge/discharge curves of such a full cell, measured at 460 °C using a current of 30 µA/cm^2. A cell voltage of about 1.2 V was obtained, with corresponding capacities ranging from 89 to 108 mAh/cm^3 (see Figure 4.8a), normalized to the combined volume of both electrodes (again without subtracting the volume of pores of the LSC cathode). Hence, charge/discharge rates are about 20 C. By integrating the discharge curves, volumetric energy densities between 51 and 53 mWh/cm^3 are obtained. Figure 4.7b displays charge/discharge curves of the LSC cathode, which were determined by measuring the voltage between the cathode and the reference electrode. The results correspond to the half cell measurements discussed above (now normalized to the volume of both electrodes). The charge/discharge characteristics of the LSCr anode, calculated from cell and cathode potentials, are shown in Figure 4.7c. The flattening of the curves at full cell potentials >0.8 V is associated with cathode potentials $\Phi > 0.1$ V vs. 1 bar O_2, *i.e.* with potentials for which O_2 formation in closed pores becomes the dominant charge storage mechanism in the LSC cathode (see above). Furthermore, charge and discharge curves of the LSCr anode show an asymmetric behavior, since the flattening is much more pronounced during charging.

Similar to the half cell measurements at 460 °C described above, capacity losses are most likely caused by oxygen leaking through the blocking layer on top of the LSC electrode, leading to coulomb efficiencies between 0.87 to 0.91 (see Figure 4.8b). A degradation of the cell capacity is not found, rather it slightly increases over the 19 cycles. The capacity of such

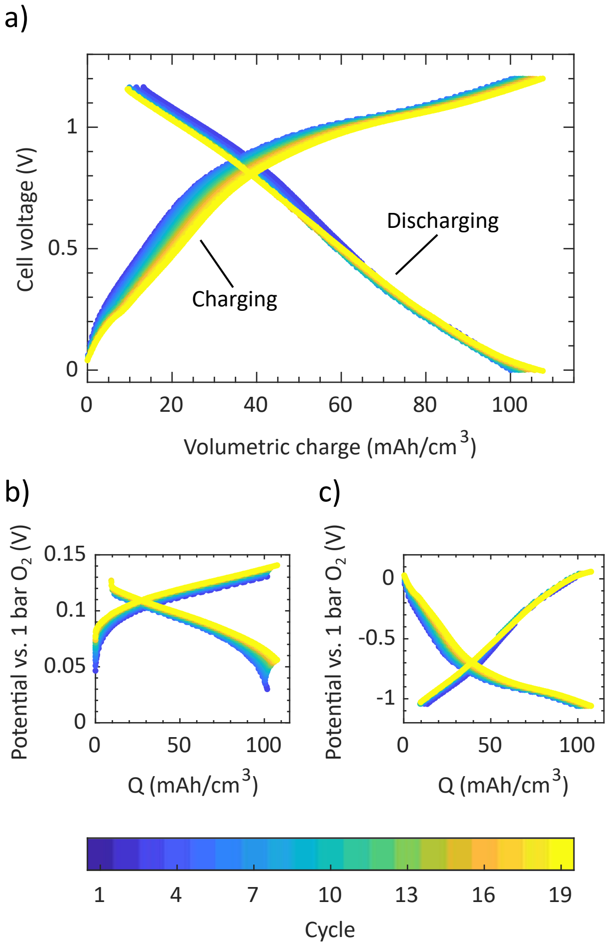

FIGURE 4.7: Cell voltage (a) and corresponding half cell potentials of a porous LSC cathode (b) and a dense LSCr anode (c) over several charge/discharge cycles, measured at 460 °C in 0.25 mbar O_2 with a current of 30 µA/cm^2 (about 20 C). The very first cycle is not shown. The charge in (a), (b) and (c) is normalized to the volume of both electrodes.

full oxygen ion batteries may be increased by pumping oxygen out of the LSC cathode via the reference electrode prior to the measurement, thus providing more oxygen vacancies to be filled with oxygen from the LSCr anode. Furthermore, the employment of a cathode material that exhibits oxygen overstoichiometry over a wide potential range such as $La_{2-x}Sr_xNiO_{4+\delta}$ could increase both the capacity as well as the cell voltage.[127]

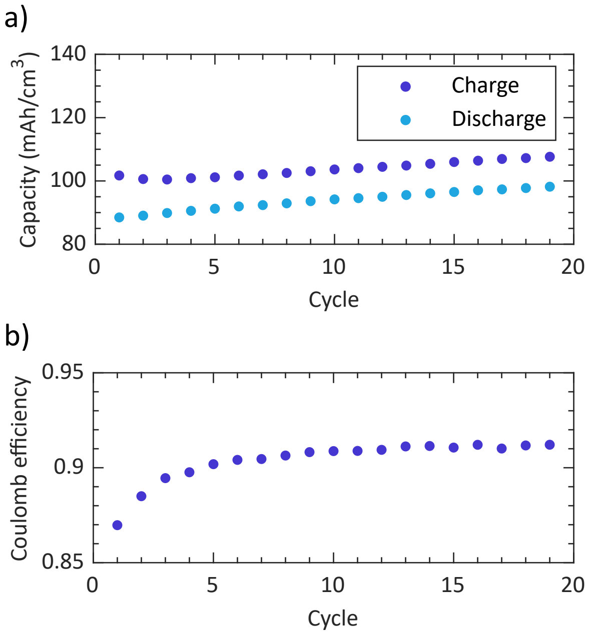

FIGURE 4.8: Cell capacity (a) and corresponding coulomb efficiency (b) of a full cell consisting of a porous LSC cathode and a dense LSCr anode during consecutive charge and discharge runs with 30 µA/cm^2 (about 20 C) at 460 °C in 0.25 mbar O_2

4.4 Conclusion

Impedance spectroscopy as well as galvanostatic cycling was used to investigate the storage of oxygen in mixed conducting oxide electrodes. For this purpose, porous $La_{0.6}Sr_{0.4}CoO_{3-\delta}$ (LSC) thin film electrodes were prepared on YSZ single crystals, with a dense LSC and a ZrO_2 blocking layer on top to prevent oxygen exchange with the measurement atmosphere. Half cell measurements were conducted at different temperatures ranging from 350 to 460 °C after equilibrating all electrodes with an oxygen partial pressure of 0.25 mbar. The highest discharge capacity of about 135 mAh/cm^3 is found at 460 °C for potentials between $\Phi = -0.145$ and 0.085 V vs. 1 bar O_2. At this temperature, two different storage mechanisms are present: For potentials <0.05 V primarily oxygen vacancies become filled, similar to the Li intercalation in electrodes of lithium ion batteries. With increasing potential, a second storage mechanism becomes relevant, where high-pressure O_2 (>500 bar at potentials >0.1 V) forms inside closed pores of the LSC working electrode. The latter process causes a broad plateau in the corresponding charge curves. It was shown that a real gas model can excellently describe this oxygen storage in closed pores. The results from galvanostatic cycling were compared with charge/voltage curves deduced from AC impedance measurements and with model calculations considering the sum of the two chemical capacitance contributions. The excellent agreement of those curves strongly supports our suggested storage mechanisms.

Measurements were also performed on full battery cells consisting of an LSC cathode and an $La_{0.9}Sr_{0.1}CrO_{3-\delta}$ (LSCr) anode. The much lower reducibility of LSCr compared to LSC resulted in a cell voltage of 1.2 V with discharge capacities up to 100 mAh/cm^3, energy densities up to 53 mWh/cm^3 at 460 °C and reasonable cycling performance. Our study thus shows that rechargeable oxygen ion batteries may store oxygen in two ways, via oxygen ions by changing the oxygen nonstoichiometry of mixed conducting oxides and via the formation of high-pressure O_2 in closed pores of a cathode at high potentials.

4.5 Appendix

4.5.1 Impedance spectroscopy

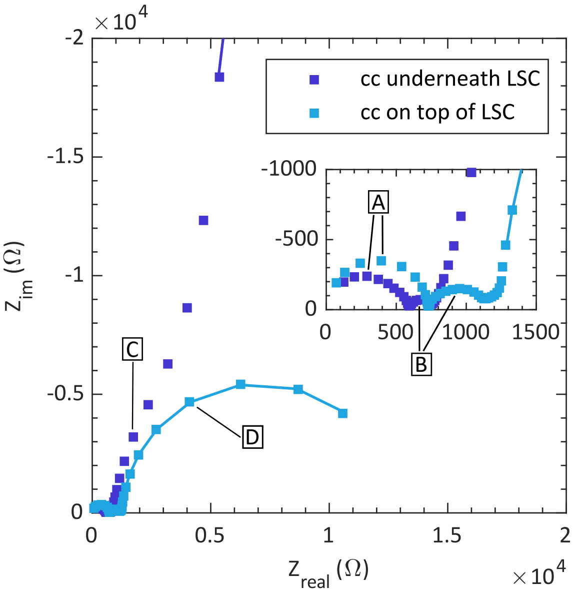

FIGURE 4.9: Impedance spectra of half cells with a difference in terms of the position of the current collector (cc), measured at open circuit conditions ($U_{DC} = 0$ V) in 0.25 mbar at 460 °C (cc underneath LSC) and at 450 °C (cc on top of LSC), respectively. Lines are fits to the spectra using an equivalent circuit consisting of a serial offset resistance and an R/CPE element.

Figure 4.9 shows spectra of two different LSC half cells, measured under open circuit conditions in 0.25 mbar at 460 °C (cc underneath LSC) and at 450 °C (cc on top of LSC), respectively. For one half cell, the current collector (cc) was placed on top of the $La_{0.6}Sr_{0.4}CoO_{3-\delta}$ (LSC) thin film, *i.e.* between the LSC film and the ZrO_2 blocking layer. In this case, the current collector was not microstructured. The other spectrum corresponds to a half cell, where the current collector was underneath the LSC film, as it was the case for all other samples in this study. Interestingly, the shoulder at frequencies between 1.6 Hz to 10 mHz (C in Figure 4.9) which is visible for all impedance spectra, is not observed when placing the current collector on top of the LSC film. Hence, we attribute this shoulder to the lateral diffusion of oxygen ions into the parts of the LSC film located on top of the current collector.

The resistive contribution of the low frequency semcircle (D) is much smaller for the sample where the current collector is on top of the LSC working electrode. Supposedly, much more oxygen leaks through the ZrO_2 blocking layer. We thus assume that the ZrO_2 layer does not grow as dense on the Pt current collector as on LSC. The contributions attributed to the ionic transport resistance of YSZ (A) and the interface between the LSC film and the YSZ electrolyte (B), respectively, are smaller for the half cell with the current collector underneath the LSC film, most probably due to a higher temperature of 460 °C compared to 450 °C at which the other half cell was measured.

4.5.2 Galvanostatic Cycling of $La_{0.6}Sr_{0.4}CoO_{3-\delta}$ Half Cells

Figure 4.10 displays charge/discharge curves over several cycles of a LSC half cell measured at 350 °C. In contrast to the measurements conducted at higher temperatures, the curves do not become flatter at high potentials (*i.e.*, $\Phi > 0.05\,\mathrm{V}$ vs. 1 bar O_2) as observed for the measurements conducted at higher temperatures. As discussed in the main text, we assume slow kinetics for the O_2 formation in closed pores of the LSC working electrode. Accordingly, this charge storage mechanism is not observed in terms of a flattening of the corresponding charge or discharge curves. At low potentials (*i.e.*, $<-0.05\,\mathrm{V}$ vs. 1 bar O_2) discharge curves seem to exhibit a lower slope than charge curves.

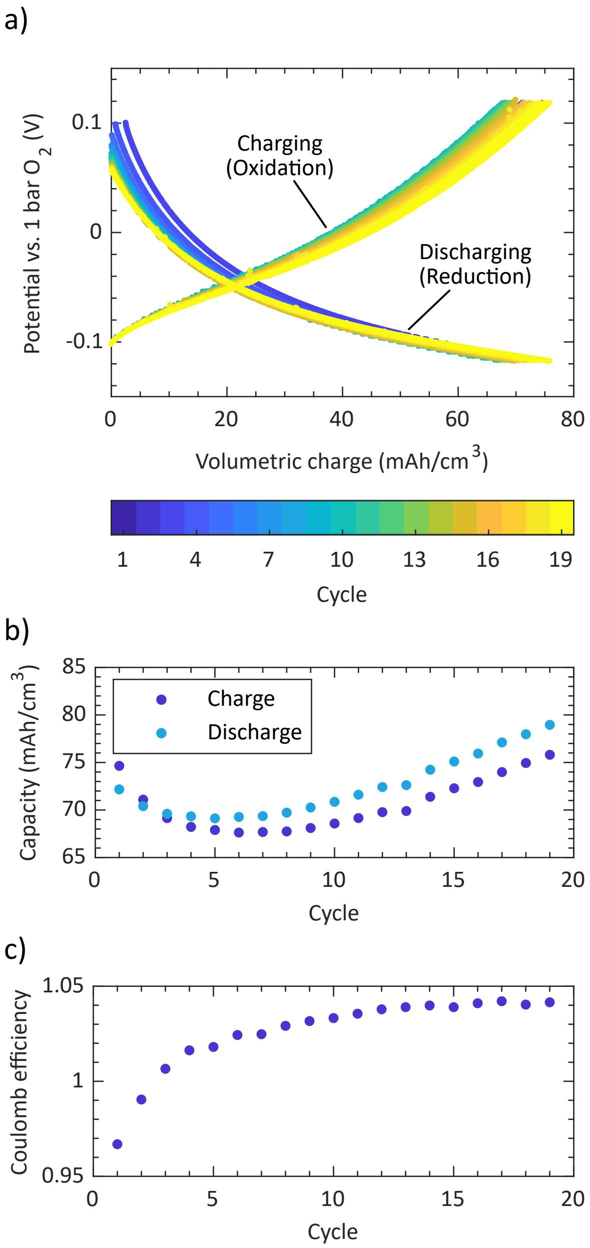

FIGURE 4.10: Charge/voltage curves over several charge/discharge cycles of an LSC half cell measured at 350 °C in 0.25 mbar O_2 with a current of 3 µA/cm^2 (ca. 6 C) between $\Phi = -0.118$ and 0.119 V with respect to 1 bar O_2. The very first cycle is not shown. Corresponding half cell half cell capacity (b) and coulomb efficiency (c).

5 Summary

In this thesis, the electrochemical behavior of anodically polarized $La_{0.6}Sr_{0.4}CoO_{3-\delta}$ (LSC) thin film electrodes was investigated by means of the chemical capacitance, obtained from impedance spectroscopy measurements under varying anodic DC voltages. Such a polarization corresponds to the operating conditions of oxygen electrodes in solid oxide electrolysis cells (SOECs). Thin film LSC electrodes were grown on yttria-stabilized zirconia (YSZ) single crystals by pulsed laser deposition (PLD). By varying the deposition parameters, electrodes with different morphologies and microstructures were fabricated. The chemical capacitance of dense electrodes and electrodes with open pores decreases with increasing anodic overpotential as expected from defect chemical considerations. However, electrodes with intentionally built-in closed pores exhibit a completely different behavior as they show an increase of the chemical capacitance with extremely high peak values in the order of 10^4 F/cm^3 at anodic overpotentials >100 mV. It was demonstrated that prediction of these capacitance peaks requires a real gas equation. A model was developed to calculate the chemical capacitance of O_2 in closed pores by means of the Soave-Redlich-Kwong real gas equation. Due to the good agreement between measured and modeled chemical capacitance curves, it is concluded that high-pressure O_2 formation in closed pores is responsible for the capacitance peaks observed under anodic polarization. The model also showed that gas pressures in the order of 10^4 bar may develop in closed pores of LSC electrodes. Remarkably, these closed pores seem to largely withstand such enormous pressures and are not destructed (*i.e.*, opened), since capacitance peaks were reproducibly found even when one electrode was measured several times. The findings of this study show that analyzing the chemical capacitance might be used as a highly sensitive tool for detecting closed pores and the corresponding O_2 formation in or near oxygen electrodes of SOECs.

This tool was applied to investigate the degradation behavior of dense electrodes and electrodes with open pores or cracks. In their pristine state, such LSC electrodes exhibit the expected chemical capacitance decrease with increasing anodic overpotential. However, different pre-treatments changed the capacitance characteristics of these electrodes. On the one hand, annealing electrodes with open pores or cracks for several hours in synthetic air resulted in very high capacitance peaks in the range of 10^4 F/cm^3. On the other hand, after the application of high anodic bias voltages of ≥750 mV for 1 h, even polycrystalline dense electrodes show a capacitance peak under anodic polarization. These capacitance peaks after the respective pre-treatments of porous and dense LSC electrodes strongly suggest formation of closed pores. Several surface sensitive analytical techniques and TEM measurements support this hypothesis: i) Annealing electrodes for several hours in synthetic air leads to Sr segregation to the surface and the formation of a $SrSO_4$ phase. This secondary phase on the surface closes already existing open pores or cracks. ii) Applying high DC voltages of $\geq$750 mV, corresponding to electrode overpotentials of $\geq$400 mV, induces morphological changes in the bulk of dense LSC films and this also leads to closed pores. Under moderate anodic polarization, all these closed pores get filled with O_2 gas, which leads to the observed chemical capacitance peaks. Model calculations allow to determine the amount of closed porosity with a lower detection limit between 10^{-4} and 10^{-3}. Hence, chemical capacitance measurements may indeed be used as a tool to identify degradation via closed pore formation at an early stage, thus preventing possibly destructive loads during operation of SOECs.

Finally, porous thin film LSC electrodes were used in rechargeable oxygen ion batteries. In order to prevent oxygen exchange with the measurement atmosphere, a dense ZrO_2 blocking layer was deposited on top of such electrodes. Half cells were characterized by means of impedance spectroscopy as well as galvanostatic cycling. Such half cell measurements yielded discharge capacities up to 135 mAh/cm^3 at 460 °C for potentials between −145 and 85 mV with respect to 1 bar O_2. Moreover, repeated charging and discharging without significant capacity loss was demonstrated. Charge/discharge curves were reconstructed from chemical capacitance data and from model calculations. By comparing these curves to galvanostatic measurements, two different storage mechanisms were identified: At rather low potentials (*i.e.*, <50 mV vs. 1 bar O_2), the main capacity originates from the gradual filling of oxygen vacancies, therefore changing the oxygen nonstoichiometry of LSC electrodes. The second charge storage mechanism dominates at higher potentials and includes O_2 formation in pores. Astonishingly high capacity values can be realized via highly compressed O_2 (*i.e.*, >500 bar) at potentials of >100 mV (vs. 1 bar O_2). Also full oxygen ion batteries were tested, which consisted of porous LSC cathodes and dense $La_{0.9}Sr_{0.1}CrO_{3-\delta}$ (LSCr) anodes. These cells exploit the lower reducibility of $La_{1-x}Sr_xCrO_{3-\delta}$ compared to $La_{1-x}Sr_xCoO_{3-\delta}$, resulting in a remarkable cell voltage of 1.2 V as well as in discharge capacities and energy densities up to 100 mAh/cm^3 and 53 mWh/cm^3. This demonstrates that oxygen ion batteries are capable of storing oxygen in two different ways, namely in form of oxygen ions by altering the oxygen nonstoichiometry of mixed conducting oxides and by forming O_2 in pores at potentials of >50 mV with respect to 1 bar O_2.

List of Abbreviations and Symbols

Abbreviation	Meaning
AFM	Atomic Force Microscopy
BF-TEM	Bright Field Electron Microscopy
CPE	Constant Phase Element
EDX	Energy Dispersive X-Ray Spectroscopy
FIB	Focused Ion Beam
GCPL	Galvanostatic Cycling with Potential Limitation
GDC	$Ce_{1-x}Gd_xO_{2-\delta}$
HAADF	High-Angle Annular Dark Field
ICP-MS	Inductively Coupled Plasma Mass Spectroscopy
LIB	Lithium Ion Battery
LSC	$La_{0.6}Sr_{0.4}CoO_{3-\delta}$
LSCF	$La_{1-x}Sr_xCo_yFe_{1-y}O_{3-\delta}$
LSCr	$La_{0.9}Sr_{0.1}Cr_{3-\delta}$
LSM	$La_{1-x}Sr_xMnO_{3-\delta}$
MIEC	Mixed Ionic and Electronic Conductor
NAP-XPS	Near Ambient Pressure X-Ray Photoelectron Spectroscopy
PLD	Pulsed Laser Deposition
ScSZ	Scandia-Stabilized Zirconia
SEM	Scanning Electron Microscopy
SOEC	Solid Oxide Electrolysis Cell
SOFC	Solid Oxide Fuel Cell
SRK	Soave-Redlich-Kwong
STEM	Scanning Transmission Electron Microscopy
TEM	Transmission Electron Microscopy
XRD	X-Ray Diffraction
YSZ	Yttria-Stabilized Zirconia

Greek symbols

Symbol	Meaning
η	overpotential
η_{WE}	overpotential of the working electrode
η_{YSZ}	overpotential of YSZ electrolyte
λ	film porosity
μ_O	chemical potential of oxygen
μ_O^{at}	chemical potential of oxygen in the gas phase
μ_O^{WE}	chemical potential of oxygen in the working electrode
μ_{O_2}	chemical potential of O_2
$\mu_{O_2}^{WE}$	chemical potential of O_2 in the working electrode
$\mu_{O_2}^{0,T}$	chemical potential of oxygen at 1 bar
φ	fugacity coefficient
Φ	potential according to Nernst's equation with respect to 1 bar oxygen
ω_a	acentric factor of O_2

Latin symbols

Symbol	Meaning
C_{chem}	chemical capacitance
$C_{chem}^{gas,ideal}$	chemical capacitance of O_2 formation according to ideal gas behavior
c_{eon}	concentration of electronic defects
c_O	concentration of oxygen
c_{O_2}	concentration of O_2
c_V	concentration of oxygen vacancies
c_V^{at}	atmospheric oxygen vacancy concentration
F	Faraday's constant
f_{O_2}	fugacity of O_2
$f_{O_2}^{WE,eff}$	effective oxygen fugacity in the working electrode
I_{DC}	DC current
N_A	Avogadro constant
p_c	critical pressure of O_2
p_{O_2}	oxygen partial pressure
$p_{O_2}^{at}$	ambient oxygen partial pressure
$p_{O_2}^{pore}$	O_2 pressure in closed pores
$p_{O_2}^{WE,eff}$	effective oxygen partial pressure inside the working electrode
Q_O	volume specific charge of the oxygen gas formation
R	universal gas constant
R_s	oxygen surface exchange resistance
R_{YSZ}	resistance of the YSZ electrolyte
T	absolute temperature
T_c	critical temperature of O_2
U_{DC}	applied DC bias voltage
V	electrode volume
V_{O_2}	molar volume of O_2
Z	compressibility factor
Z_{CPE}	impedance of constant phase element

Bibliography

[1] IPCC, *Climate Change 2022: Impacts, Adaptation and Vulnerability. Contribution of Working Group II to the Sixth Assessment Report of the Intergovernmental Panel on Climate Change*; Summary for Policymakers; Cambridge University Press, pp 3–33.

[2] Pathak, M.; Slade, R.; Shukla, P.; Skea, J.; Pichs-Madruga, R.; Ürge-Vorsatz, D. *Climate Change 2022: Mitigation of Climate Change. Contribution of Working Group III to the Sixth Assessment Report of the Intergovernmental Panel on Climate Change*; Technical Summary; Cambridge University Press.

[3] Romanelli, F. Strategies for the integration of intermittent renewable energy sources in the electrical system. *The European Physical Journal Plus* **2016**, *131*, 1–15.

[4] Mulder, F. M. Implications of diurnal and seasonal variations in renewable energy generation for large scale energy storage. *Journal of Renewable and Sustainable Energy* **2014**, *6*, 033105.

[5] Heide, D.; von Bremen, L.; Greiner, M.; Hoffmann, C.; Speckmann, M.; Bofinger, S. Seasonal optimal mix of wind and solar power in a future, highly renewable Europe. *Renewable Energy* **2010**, *35*, 2483–2489.

[6] Buttler, A.; Dinkel, F.; Franz, S.; Spliethoff, H. Variability of wind and solar power – An assessment of the current situation in the European Union based on the year 2014. *Energy* **2016**, *106*, 147–161.

[7] Ramsebner, J.; Haas, R.; Ajanovic, A.; Wietschel, M. The sector coupling concept: A critical review. *WIREs Energy and Environment* **2021**, *10*, 1–27.

[8] Zsiborács, H.; Baranyai, N. H.; Vincze, A.; Zentkó, L.; Birkner, Z.; Máté, K.; Pintér, G. Intermittent Renewable Energy Sources: The Role of Energy Storage in the European Power System of 2040. *Electronics* **2019**, *8*, 729.

[9] Suberu, M. Y.; Mustafa, M. W.; Bashir, N. Energy storage systems for renewable energy power sector integration and mitigation of intermittency. *Renewable and Sustainable Energy Reviews* **2014**, *35*, 499–514.

[10] Doenitz, W.; Schmidberger, R.; Steinheil, E.; Streicher, R. Hydrogen production by high temperature electrolysis of water vapour. *International Journal of Hydrogen Energy* **1980**, *5*, 55–63.

[11] Buttler, A.; Spliethoff, H. Current status of water electrolysis for energy storage, grid balancing and sector coupling via power-to-gas and power-to-liquids: A review. *Renewable and Sustainable Energy Reviews* **2018**, *82*, 2440–2454.

[12] Wang, Y.; Liu, T.; Lei, L.; Chen, F. High temperature solid oxide H_2O/CO_2 co-electrolysis for syngas production. *Fuel Processing Technology* **2017**, *161*, 248–258.

[13] Chen, L.; Chen, F.; Xia, C. Direct synthesis of methane from CO_2–H_2O co-electrolysis in tubular solid oxide electrolysis cells. *Energy Environ. Sci.* **2014**, *7*, 4018–4022.

[14] Staffell, I.; Scamman, D.; Abad, A. V.; Balcombe, P.; Dodds, P. E.; Ekins, P.; Shah, N.; Ward, K. R. The role of hydrogen and fuel cells in the global energy system. *Energy & Environmental Science* **2019**, *12*, 463–491.

[15] Barthelemy, H.; Weber, M.; Barbier, F. Hydrogen storage: Recent improvements and industrial perspectives. *International Journal of Hydrogen Energy* **2017**, *42*, 7254–7262.

[16] Peters, R.; Deja, R.; Engelbracht, M.; Frank, M.; Nguyen, V. N.; Blum, L.; Stolten, D. Efficiency analysis of a hydrogen-fueled solid oxide fuel cell system with anode off-gas recirculation. *Journal of Power Sources* **2016**, *328*, 105–113.

[17] Peters, R.; Frank, M.; Tiedemann, W.; Hoven, I.; Deja, R.; Nguyen, V. N.; Blum, L.; Stolten, D. Development and Testing of a 5kW-Class Reversible Solid Oxide Cell System. *ECS Transactions* **2019**, *91*, 2495–2506.

[18] Ni, M.; Leung, M.; Leung, D. Technological development of hydrogen production by solid oxide electrolyzer cell (SOEC). *International Journal of Hydrogen Energy* **2008**, *33*, 2337–2354.

[19] Gómez, S. Y.; Hotza, D. Current developments in reversible solid oxide fuel cells. *Renewable and Sustainable Energy Reviews* **2016**, *61*, 155–174.

[20] Laguna-Bercero, M. A. Recent advances in high temperature electrolysis using solid oxide fuel cells: A review. *Journal of Power Sources* **2012**, *203*, 4–16.

[21] Chen, K.; Jiang, S. P. Review - Materials Degradation of Solid Oxide Electrolysis Cells. *Journal of The Electrochemical Society* **2016**, *163*, F3070–F3083.

[22] Wang, Y.; Li, W.; Ma, L.; Li, W.; Liu, X. Degradation of solid oxide electrolysis cells: Phenomena, mechanisms, and emerging mitigation strategies—A review. *Journal of Materials Science & Technology* **2020**, *55*, 35–55.

[23] Ebbesen, S. D.; Jensen, S. H.; Hauch, A.; Mogensen, M. B. High Temperature Electrolysis in Alkaline Cells, Solid Proton Conducting Cells, and Solid Oxide Cells. *Chemical Reviews* **2014**, *114*, 10697–10734.

[24] Jiang, S. P. Sintering behavior of Ni/Y_2O_3-ZrO_2 cermet electrodes of solid oxide fuel cells. *Journal of Materials Science* **2003**, *38*, 3775–3782.

[25] Müller, A. C.; Herbstritt, D.; Ivers-Tiffée, E. Development of a multilayer anode for solid oxide fuel cells. *Solid State Ionics* **2002**, *152-153*, 537–542.

[26] Frey, C. E.; Fang, Q.; Sebold, D.; Blum, L.; Menzler, N. H. A Detailed Post Mortem Analysis of Solid Oxide Electrolyzer Cells after Long-Term Stack Operation. *Journal of The Electrochemical Society* **2018**, *165*, F357–F364.

[27] Hauch, A.; Jensen, S.; Bilde-Sorensen, J.; Mogensen, M. Silica Segregation in the Ni/YSZ Electrode. *Journal of The Electrochemical Society* **2007**, *154*, A619.

[28] Knibbe, R.; Traulsen, M. L.; Hauch, A.; Ebbesen, S. D.; Mogensen, M. Solid Oxide Electrolysis Cells: Degradation at High Current Densities. *Journal of The Electrochemical Society* **2010**, *157*, B1209.

[29] Tao, Y.; Ebbesen, S. D.; Mogensen, M. B. Carbon Deposition in Solid Oxide Cells during Co-Electrolysis of H_2O and CO_2. *Journal of The Electrochemical Society* **2014**, *161*, F337–F343.

[30] Nenning, A.; Holzmann, M.; Fleig, J.; Opitz, A. K. Excellent kinetics of single-phase Gd-doped ceria fuel electrodes in solid oxide cells. *Materials Advances* **2021**, *2*, 5422–5431.

[31] Xing, R.; Wang, Y.; Liu, S.; Jin, C. Preparation and characterization of $(La_{0.75}Sr_{0.25})_{0.95}Cr_{0.5}Mn_{0.5}O_3$ - yttria stabilized zirconia cathode supported solid oxide electrolysis cells for hydrogen generation. *Journal of Power Sources* **2012**, *208*, 276–281.

[32] Tsekouras, G.; Irvine, J. T. S. The role of defect chemistry in strontium titanates utilised for high temperature steam electrolysis. *Journal of Materials Chemistry* **2011**, *21*, 9367.

[33] Khan, M.; Xu, X.; Knibbe, R.; Zhu, Z. Air electrodes and related degradation mechanisms in solid oxide electrolysis and reversible solid oxide cells. *Renewable and Sustainable Energy Reviews* **2021**, *143*, 110918.

[34] Sitte, W., Merkle, R., Eds. *High-Temperature Electrolysis*; IOP Publishing.

[35] Kilner, J.; Brook, R. A study of oxygen ion conductivity in doped non-stoichiometric oxides. *Solid State Ionics* **1982**, *6*, 237–252.

[36] Inaba, H.; Tagawa, H. Ceria-based solid electrolytes. *Solid State Ionics* **1996**, *83*, 1–16.

[37] Zhu, S.; Wang, Y.; Rao, Y.; Zhan, Z.; Xia, C. Chemically-induced mechanical unstability of samaria-doped ceria electrolyte for solid oxide electrolysis cells. *International Journal of Hydrogen Energy* **2014**, *39*, 12440–12447.

[38] Kim, S. J.; Kim, S. W.; Park, Y. M.; Kim, K. J.; Choi, G. M. Effect of Gd-doped ceria interlayer on the stability of solid oxide electrolysis cell. *Solid State Ionics* **2016**, *295*, 25–31.

[39] Stevenson, J. W.; Armstrong, T. R.; McCready, D. E.; Pederson, L. R.; Weber, W. J. Processing and Electrical Properties of Alkaline Earth-Doped Lanthanum Gallate. *Journal of The Electrochemical Society* **1997**, *144*, 3613–3620.

[40] Zhang, X.; Ohara, S.; Maric, R.; Okawa, H.; Fukui, T.; Yoshida, H.; Inagaki, T.; Miura, K. Interface reactions in the NiO–SDC–LSGM system. *Solid State Ionics* **2000**, *133*, 153–160.

[41] Keane, M.; Mahapatra, M. K.; Verma, A.; Singh, P. LSM-YSZ interactions and anode delamination in solid oxide electrolysis cells. *International Journal of Hydrogen Energy* **2012**, *37*, 16776–16785.

[42] Laguna-Bercero, M.; Campana, R.; Larrea, A.; Kilner, J.; Orera, V. Electrolyte degradation in anode supported microtubular yttria stabilized zirconia-based solid oxide steam electrolysis cells at high voltages of operation. *Journal of Power Sources* **2011**, *196*, 8942–8947.

[43] Tietz, F.; Sebold, D.; Brisse, A.; Schefold, J. Degradation phenomena in a solid oxide electrolysis cell after 9000 h of operation. *Journal of Power Sources* **2013**, *223*, 129–135.

[44] Kim, J.; Ji, H.-I.; Dasari, H. P.; Shin, D.; Song, H.; Lee, J.-H.; Kim, B.-K.; Je, H.-J.; Lee, H.-W.; Yoon, K. J. Degradation mechanism of electrolyte and air electrode in solid oxide electrolysis cells operating at high polarization. *International Journal of Hydrogen Energy* **2013**, *38*, 1225–1235.

[45] Hjalmarsson, P.; Sun, X.; Liu, Y.-L.; Chen, M. Influence of the oxygen electrode and inter-diffusion barrier on the degradation of solid oxide electrolysis cells. *Journal of Power Sources* **2013**, *223*, 349–357.

[46] Park, B.-K.; Zhang, Q.; Voorhees, P. W.; Barnett, S. A. Conditions for stable operation of solid oxide electrolysis cells: oxygen electrode effects. *Energy & Environmental Science* **2019**, *12*, 3053–3062.

[47] Chen, K.; Jiang, S. P. Failure mechanism of (La,Sr)MnO_3 oxygen electrodes of solid oxide electrolysis cells. *International Journal of Hydrogen Energy* **2011**, *36*, 10541–10549.

[48] Pan, Z.; Liu, Q.; Ni, M.; Lyu, R.; Li, P.; Chan, S. H. Activation and failure mechanism of $La_{0.6}Sr_{0.4}Co_{0.2}Fe_{0.8}O_{3-\delta}$ air electrode in solid oxide electrolyzer cells under high-current electrolysis. *International Journal of Hydrogen Energy* **2018**, *43*, 5437–5450.

[49] Kim, S. J.; Choi, G. M. Stability of LSCF electrode with GDC interlayer in YSZ-based solid oxide electrolysis cell. *Solid State Ionics* **2014**, *262*, 303–306.

[50] Mawdsley, J. R.; Carter, J. D.; Kropf, A. J.; Yildiz, B.; Maroni, V. A. Post-test evaluation of oxygen electrodes from solid oxide electrolysis stacks. *International Journal of Hydrogen Energy* **2009**, *34*, 4198–4207.

[51] Rashkeev, S. N.; Glazoff, M. V. Atomic-scale mechanisms of oxygen electrode delamination in solid oxide electrolyzer cells. *International Journal of Hydrogen Energy* **2012**, *37*, 1280–1291.

[52] Virkar, A. V. Mechanism of oxygen electrode delamination in solid oxide electrolyzer cells. *International Journal of Hydrogen Energy* **2010**, *35*, 9527–9543.

[53] Jacobsen, T.; Mogensen, M. The Course of Oxygen Partial Pressure and Electric Potentials across an Oxide Electrolyte Cell. *ECS Transactions* **2008**, *13*, 259–273.

[54] Schmid, A.; Rupp, G. M.; Fleig, J. Voltage and partial pressure dependent defect chemistry in (La,Sr)$FeO_{3-\delta}$ thin films investigated by chemical capacitance measurements. *Physical Chemistry Chemical Physics* **2018**, *20*, 12016–12026.

[55] Kawada, T.; Suzuki, J.; Sase, M.; Kaimai, A.; Yashiro, K.; Nigara, Y.; Mizusaki, J.; Kawamura, K.; Yugami, H. Determination of Oxygen Vacancy Concentration in a Thin Film of $La_{0.6}Sr_{0.4}CoO_{3-\delta}$ by an Electrochemical Method. *Journal of The Electrochemical Society* **2002**, *149*, E252.

[56] Baumann, F. S.; Fleig, J.; Habermaier, H.-U.; Maier, J. Impedance spectroscopic study on well-defined (La,Sr)(Co,Fe)$O_{3-\delta}$ model electrodes. *Solid State Ionics* **2006**, *177*, 1071–1081.

[57] Jamnik, J.; Maier, J. Treatment of the Impedance of Mixed Conductors Equivalent Circuit Model and Explicit Approximate Solutions. *Journal of The Electrochemical Society* **1999**, *146*, 4183.

[58] Jamnik, J.; Maier, J. Generalised equivalent circuits for mass and charge transport: chemical capacitance and its implications. *Physical Chemistry Chemical Physics* **2001**, *3*, 1668–1678.

[59] Rupp, G. M.; Limbeck, A.; Kubicek, M.; Penn, A.; Stöger-Pollach, M.; Friedbacher, G.; Fleig, J. Correlating surface cation composition and thin film microstructure with the electrochemical performance of lanthanum strontium cobaltite (LSC) electrodes. *J. Mater. Chem. A* **2014**, *2*, 7099–7108.

[60] Januschewsky, J.; Ahrens, M.; Opitz, A.; Kubel, F.; Fleig, J. Optimized $La_{0.6}Sr_{0.4}CoO_{3-\delta}$ Thin-Film Electrodes with Extremely Fast Oxygen-Reduction Kinetics. *Advanced Functional Materials* **2009**, *19*, 3151–3156.

[61] Kubicek, M.; Huber, T. M.; Welzl, A.; Penn, A.; Rupp, G. M.; Bernardi, J.; Stöger-Pollach, M.; Hutter, H.; Fleig, J. Electrochemical properties of $La_{0.6}Sr_{0.4}CoO_{3-\delta}$ thin films investigated by complementary impedance spectroscopy and isotope exchange depth profiling. *Solid State Ionics* **2014**, *256*, 38–44.

[62] Rupp, G. M.; Téllez, H.; Druce, J.; Limbeck, A.; Ishihara, T.; Kilner, J.; Fleig, J. Surface chemistry of $La_{0.6}Sr_{0.4}CoO_{3-\delta}$ thin films and its impact on the oxygen surface exchange resistance. *J. Mater. Chem. A* **2015**, *3*, 22759–22769.

[63] Limbeck, A.; Rupp, G. M.; Kubicek, M.; Téllez, H.; Druce, J.; Ishihara, T.; Kilner, J. A.; Fleig, J. Dynamic etching of soluble surface layers with on-line inductively coupled plasma mass spectrometry detection – a novel approach for determination of complex metal oxide surface cation stoichiometry. *Journal of Analytical Atomic Spectrometry* **2016**, *31*, 1638–1646.

[64] Cai, Z.; Kubicek, M.; Fleig, J.; Yildiz, B. Chemical Heterogeneities on $La_{0.6}Sr_{0.4}CoO_{3-\delta}$ Thin Films—Correlations to Cathode Surface Activity and Stability. *Chemistry of Materials* **2012**, *24*, 1116–1127.

[65] Opitz, A. K.; Fleig, J. Investigation of O_2 reduction on Pt/YSZ by means of thin film microelectrodes: The geometry dependence of the electrode impedance. *Solid State Ionics* **2010**, *181*, 684–693.

[66] Siebenhofer, M.; Huber, T. M.; Friedbacher, G.; Artner, W.; Fleig, J.; Kubicek, M. Oxygen exchange kinetics and nonstoichiometry of pristine $La_{0.6}Sr_{0.4}CoO_{3-\delta}$ thin films unaltered by degradation. *Journal of Materials Chemistry A* **2020**, *8*, 7968–7979.

[67] Siebenhofer, M.; Riedl, C.; Schmid, A.; Limbeck, A.; Opitz, A. K.; Fleig, J.; Kubicek, M. Investigating oxygen reduction pathways on pristine SOFC cathode surfaces by *in situ* PLD impedance spectroscopy. *Journal of Materials Chemistry A* **2022**, *10*, 2305–2319.

[68] Schmid, A.; Rupp, G. M.; Fleig, J. How To Get Mechanistic Information from Partial Pressure-Dependent Current–Voltage Measurements of Oxygen Exchange on Mixed Conducting Electrodes. *Chemistry of Materials* **2018**, *30*, 4242–4252.

[69] Baumann, F.; Maier, J.; Fleig, J. The polarization resistance of mixed conducting SOFC cathodes: A comparative study using thin film model electrodes. *Solid State Ionics* **2008**, *179*, 1198–1204.

[70] Fleig, J. The grain boundary impedance of random microstructures: numerical simulations and implications for the analysis of experimental data. *Solid State Ionics* **2002**, *150*, 181–193.

[71] Bucher, E.; Sitte, W. Defect Chemical Modeling of (La,Sr)(Co,Fe)$O_{3-\delta}$. *Journal of Electroceramics* **2004**, *13*, 779–784.

[72] Lankhorst, M. H. R. Determination of Oxygen Nonstoichiometry and Diffusivity in Mixed Conducting Oxides by Oxygen Coulometric Titration. *Journal of The Electrochemical Society* **1997**, *144*, 1268.

[73] Mizusaki, J.; Mima, Y.; Yamauchi, S.; Fueki, K.; Tagawa, H. Nonstoichiometry of the perovskite-type oxides $La_{1-x}Sr_xCoO_{3-\delta}$. *Journal of Solid State Chemistry* **1989**, *80*, 102–111.

[74] Mizusaki, J.; Yoshihiro, M.; Yamauchi, S.; Fueki, K. Nonstoichiometry and defect structure of the perovskite-type oxides $La_{1-x}Sr_xFeO_{3-\delta}$. *Journal of Solid State Chemistry* **1985**, *58*, 257–266.

[75] Kuhn, M.; Hashimoto, S.; Sato, K.; Yashiro, K.; Mizusaki, J. Oxygen nonstoichiometry and thermo-chemical stability of $La_{0.6}Sr_{0.4}CoO_{3-\delta}$. *Journal of Solid State Chemistry* **2013**, *197*, 38–45.

[76] Sitte, W.; Bucher, E.; Preis, W. Nonstoichiometry and transport properties of strontium-substituted lanthanum cobaltites. *Solid State Ionics* **2002**, *154-155*, 517–522.

[77] Soave, G. Equilibrium constants from a modified Redlich-Kwong equation of state. *Chemical Engineering Science* **1972**, *27*, 1197–1203.

[78] Kleiber, M.; Joh, R. *Properties of Pure Fluid Substances in VDI Heat Atlas*, 2nd ed.; Springer Berlin Heidelberg, 2010; Chapter Properties of Pure Fluid Substances, pp 301–393.

[79] Risold, D.; Hallstedt, B.; Gauckler, L. J. The strontium-oxygen system. *Calphad* **1996**, *20*, 353–361.

[80] Akahama, Y.; Kawamura, H.; Häusermann, D.; Hanfland, M.; Shimomura, O. New High-Pressure Structural Transition of Oxygen at 96 GPa Associated with Metallization in a Molecular Solid. *Physical Review Letters* **1995**, *74*, 4690–4693.

[81] Krammer, M.; Schmid, A.; Siebenhofer, M.; Bumberger, A. E.; Herzig, C.; Limbeck, A.; Kubicek, M.; Fleig, J. Formation and Detection of High-Pressure Oxygen in Closed Pores of $La_{0.6}Sr_{0.4}CoO_{3-\delta}$ Solid Oxide Electrolysis Anodes. *ACS Applied Energy Materials* **2022**, *5*, 8324–8335.

[82] Huber, T.; Opitz, A.; Kubicek, M.; Hutter, H.; Fleig, J. Temperature gradients in microelectrode measurements: Relevance and solutions for studies of SOFC electrode materials. *Solid State Ionics* **2014**, *268*, 82–93.

[83] Rameshan, R.; Nenning, A.; Raschhofer, J.; Lindenthal, L.; Ruh, T.; Summerer, H.; Opitz, A.; Huber, T. M.; Rameshan, C. Novel Sample-Stage for Combined Near Ambient Pressure X-ray Photoelectron Spectroscopy, Catalytic Characterization and Electrochemical Impedance Spectroscopy. *Crystals* **2020**, *10*, 947.

[84] Scofield, J. H. Hartree-Slater subshell photoionization cross-sections at 1254 and 1487 eV. *Journal of Electron Spectroscopy and Related Phenomena* **1976**, *8*, 129–137.

[85] Lankhorst, M. H.; Bouwmeester, H.; Verweij, H. High-Temperature Coulometric Titration of $La_{1-x}Sr_xCoO_{3-\delta}$: Evidence for the Effect of Electronic Band Structure on Nonstoichiometry Behavior. *Journal of Solid State Chemistry* **1997**, *133*, 555–567.

[86] Guan, Z.; Chen, D.; Chueh, W. C. Analyzing the dependence of oxygen incorporation current density on overpotential and oxygen partial pressure in mixed conducting oxide electrodes. *Physical Chemistry Chemical Physics* **2017**, *19*, 23414–23424.

[87] Kuhn, M.; Hashimoto, S.; Sato, K.; Yashiro, K.; Mizusaki, J. Oxygen nonstoichiometry, thermo-chemical stability and lattice expansion of $La_{0.6}Fe_{0.4}CoO_{3-\delta}$. *Solid State Ionics* **2011**, *195*, 7–15.

[88] Kubicek, M.; Limbeck, A.; Frömling, T.; Hutter, H.; Fleig, J. Relationship between Cation Segregation and the Electrochemical Oxygen Reduction Kinetics of $La_{0.6}Sr_{0.4}CoO_{3-\delta}$ Thin Film Electrodes. *Journal of The Electrochemical Society* **2011**, *158*, B727.

[89] Celikbilek, O.; Cavallaro, A.; Kerherve, G.; Fearn, S.; Chaix-Pluchery, O.; Aguadero, A.; Kilner, J. A.; Skinner, S. J. Surface Restructuring of Thin-Film Electrodes Based on Thermal History and Its Significance for the Catalytic Activity and Stability at the Gas/Solid and Solid/Solid Interfaces. *ACS Applied Materials & Interfaces* **2020**, *12*, 34388–34401.

[90] Feng, Z.; Crumlin, E. J.; Hong, W. T.; Lee, D.; Mutoro, E.; Biegalski, M. D.; Zhou, H.; Bluhm, H.; Christen, H. M.; Shao-Horn, Y. In Situ Studies of the Temperature-Dependent Surface Structure and Chemistry of Single-Crystalline (001)-Oriented $La_{0.8}Sr_{0.2}CoO_{3-\delta}$ Perovskite Thin Films. *The Journal of Physical Chemistry Letters* **2013**, *4*, 1512–1518.

[91] Bucher, E.; Gspan, C.; Sitte, W. Degradation and regeneration of the SOFC cathode material $La_{0.6}Sr_{0.4}CoO_{3-\delta}$ in SO_2-containing atmospheres. *Solid State Ionics* **2015**, *272*, 112–120.

[92] Kushi, T. Effects of sulfur poisoning on degradation phenomena in oxygen electrodes of solid oxide electrolysis cells and solid oxide fuel cells. *International Journal of Hydrogen Energy* **2017**, *42*, 9396–9405.

[93] Bucher, E.; Gspan, C.; Hofer, F.; Sitte, W. Sulphur poisoning of the SOFC cathode material $La_{0.6}Sr_{0.4}CoO_{3-\delta}$. *Solid State Ionics* **2013**, *238*, 15–23.

[94] Siebenhofer, M.; Haselmann, U.; Nenning, A.; Friedbacher, G.; Bumberger, A. E.; Wurster, S.; Artner, W.; Hutter, H.; Zhang, Z.; Fleig, J.; Kubicek, M. Surface Chemistry and Degradation Processes of Dense $La_{0.6}Sr_{0.4}CoO_{3-\delta}$ Thin Film Electrodes. *Journal of The Electrochemical Society* **2022**,

[95] Nenning, A.; Opitz, A. K.; Rameshan, C.; Rameshan, R.; Blume, R.; Hävecker, M.; Knop-Gericke, A.; Rupprechter, G.; Klötzer, B.; Fleig, J. Ambient Pressure XPS Study of Mixed Conducting Perovskite-Type SOFC Cathode and Anode Materials under Well-Defined Electrochemical Polarization. *The Journal of Physical Chemistry C* **2016**, *120*, 1461–1471.

[96] Stoerzinger, K. A.; Hong, W. T.; Crumlin, E. J.; Bluhm, H.; Biegalski, M. D.; Shao-Horn, Y. Water Reactivity on the $LaCoO_3$ (001) Surface: An Ambient Pressure X-ray Photoelectron Spectroscopy Study. *The Journal of Physical Chemistry C* **2014**, *118*, 19733–19741.

[97] Crumlin, E. J.; Mutoro, E.; Hong, W. T.; Biegalski, M. D.; Christen, H. M.; Liu, Z.; Bluhm, H.; Shao-Horn, Y. In Situ Ambient Pressure X-ray Photoelectron Spectroscopy of Cobalt Perovskite Surfaces under Cathodic Polarization at High Temperatures. *The Journal of Physical Chemistry C* **2013**, *117*, 16087–16094.

[98] Schmid, A.; Nenning, A.; Opitz, A.; Kubicek, M.; Fleig, J. High Oxygen Exchange Activity of Pristine $La_{0.6}Sr_{0.4}FeO_{3-\delta}$ Films and Its Degradation. *Journal of The Electrochemical Society* **2020**, *167*, 124509.

[99] Vero, J. C. D.; Yokokawa, H.; Develos-Bagarinao, K.; Liu, S.-S.; Kishimoto, H.; Ishiyama, T.; Yamaji, K.; Horita, T. Influence of electrolyte substrates on the Sr-segregation and $SrSO_4$ formation in $La_{0.6}Sr_{0.4}Co_{0.2}Fe_{0.8}O_{3-\delta}$ thin films. *MRS Communications* **2019**, *9*, 236–244.

[100] Riedl, C.; Siebenhofer, M.; Nenning, A.; Schmid, A.; Weiss, M.; Rameshan, C.; Limbeck, A.; Kubicek, M.; Opitz, A. K.; Fleig, J. *In situ* techniques reveal the true capabilities of SOFC cathode materials and their sudden degradation due to omnipresent sulfur trace impurities. *J. Mater. Chem. A* **2022**, *10*, 14838–14848.

[101] Tripković, Đ.; Wang, J.; Küngas, R.; Mogensen, M. B.; Yildiz, B.; Hendriksen, P. V. Thermally Controlled Activation and Passivation of Surface Chemistry and Oxygen-Exchange Kinetics on a Perovskite Oxide. *Chemistry of Materials* **2022**, *34*, 1722–1736.

[102] Mahmoud, A.; Daroukh, M. A.; Lipinska-Chwalek, M.; Luysberg, M.; Tietz, F.; Hermann, R. P. A Mössbauer spectral study of degradation in $La_{0.58}Sr_{0.4}Fe_{0.5}Co_{0.5}O_{3-x}$ after long-term operation in solid oxide electrolysis cells. *Solid State Ionics* **2017**, *312*, 38–43.

[103] Blomgren, G. E. The Development and Future of Lithium Ion Batteries. *Journal of The Electrochemical Society* **2016**, *164*, A5019–A5025.

[104] Miao, Y.; Hynan, P.; von Jouanne, A.; Yokochi, A. Current Li-Ion Battery Technologies in Electric Vehicles and Opportunities for Advancements. *Energies* **2019**, *12*, 1074.

[105] Houache, M. S. E.; Yim, C.-H.; Karkar, Z.; Abu-Lebdeh, Y. On the Current and Future Outlook of Battery Chemistries for Electric Vehicles—Mini Review. *Batteries* **2022**, *8*, 70.

[106] Valant, C.; Gaustad, G.; Nenadic, N. Characterizing Large-Scale, Electric-Vehicle Lithium Ion Transportation Batteries for Secondary Uses in Grid Applications. *Batteries* **2019**, *5*, 8.

[107] Purvins, A.; Sumner, M. Optimal management of stationary lithium-ion battery system in electricity distribution grids. *Journal of Power Sources* **2013**, *242*, 742–755.

[108] Killer, M.; Farrokhseresht, M.; Paterakis, N. G. Implementation of large-scale Li-ion battery energy storage systems within the EMEA region. *Applied Energy* **2020**, *260*, 114166.

[109] Figgener, J.; Stenzel, P.; Kairies, K.-P.; Linßen, J.; Haberschusz, D.; Wessels, O.; Angenendt, G.; Robinius, M.; Stolten, D.; Sauer, D. U. The development of stationary battery storage systems in Germany – A market review. *Journal of Energy Storage* **2020**, *29*, 101153.

[110] Liu, K.; Liu, Y.; Lin, D.; Pei, A.; Cui, Y. Materials for lithium-ion battery safety. *Science Advances* **2018**, *4*, eaas9820.

[111] Zhao, Y.; Pohl, O.; Bhatt, A. I.; Collis, G. E.; Mahon, P. J.; Rüther, T.; Hollenkamp, A. F. A Review on Battery Market Trends, Second-Life Reuse, and Recycling. *Sustainable Chemistry* **2021**, *2*, 167–205.

[112] Olivetti, E. A.; Ceder, G.; Gaustad, G. G.; Fu, X. Lithium-Ion Battery Supply Chain Considerations: Analysis of Potential Bottlenecks in Critical Metals. *Joule* **2017**, *1*, 229–243.

[113] Xu, C.; Dai, Q.; Gaines, L.; Hu, M.; Tukker, A.; Steubing, B. Future material demand for automotive lithium-based batteries. *Communications Materials* **2020**, *1*, 1–10.

[114] McManus, M. Environmental consequences of the use of batteries in low carbon systems: The impact of battery production. *Applied Energy* **2012**, *93*, 288–295.

[115] Kharbachi, A. E.; Zavorotynska, O.; Latroche, M.; Cuevas, F.; Yartys, V.; Fichtner, M. Exploits, advances and challenges benefiting beyond Li-ion battery technologies. *Journal of Alloys and Compounds* **2020**, *817*, 153261.

[116] Walter, M.; Kovalenko, M. V.; Kravchyk, K. V. Challenges and benefits of post-lithium-ion batteries. *New Journal of Chemistry* **2020**, *44*, 1677–1683.

[117] Dühnen, S.; Betz, J.; Kolek, M.; Schmuch, R.; Winter, M.; Placke, T. Toward Green Battery Cells: Perspective on Materials and Technologies. *Small Methods* **2020**, *4*, 2000039.

[118] Schmid, A.; Krammer, M.; Fleig, J. Rechargeable Oxide Ion Batteries Based on Mixed Conducting Oxide Electrodes. *Advanced Energy Materials* **2023**, 2203789.

[119] Mizusaki, J.; Yamauchi, S.; Fueki, K.; Ishikawa, A. Nonstoichiometry of the perovskite-type oxide $La_{1-x}Sr_xCrO_{3-\delta}$. *Solid State Ionics* **1984**, *12*, 119–124.

[120] Oishi, M.; Yashiro, K.; Sato, K.; Mizusaki, J.; Kawada, T. Oxygen nonstoichiometry and defect structure analysis of B-site mixed perovskite-type oxide $(La,Sr)(Cr,M)O_{3-\delta}$ (M=Ti, Mn and Fe). *Journal of Solid State Chemistry* **2008**, *181*, 3177–3184.

[121] Momma, A.; Kato, T.; Kaga, Y.; Nagata, S. Polarization Behavior of High Temperature Solid Oxide Electrolysis Cells (SOEC). *Journal of the Ceramic Society of Japan* **1997**, *105*, 369–373.

[122] Ahamer, C.; Opitz, A. K.; Rupp, G. M.; Fleig, J. Revisiting the Temperature Dependent Ionic Conductivity of Yttria Stabilized Zirconia (YSZ). *Journal of The Electrochemical Society* **2017**, *164*, F790–F803.

[123] Huang, R.; Carr, C. G.; Gopal, C. B.; Haile, S. M. Broad Applicability of Electrochemical Impedance Spectroscopy to the Measurement of Oxygen Nonstoichiometry in Mixed Ion and Electron Conductors. *ACS Applied Materials & Interfaces* **2022**, *14*, 19629–19643.

[124] Krammer, M.; Schmid, A.; Nenning, A.; Bumberger, A. E.; Siebenhofer, M.; Herzig, C.; Limbeck, A.; Rameshan, C.; Kubicek, M.; Fleig, J. Closed pore formation in solid oxide electrolysis anodes investigated by impedance spectroscopy. *ACS Applied Materials & Interfaces* **2023**, accepted for publication.

[125] Chen, D.; Tuller, H. L. Voltage-Controlled Nonstoichiometry in Oxide Thin Films: $Pr_{0.1}Ce_{0.9}O_{2-\delta}$Case Study. *Advanced Functional Materials* **2014**, *24*, 7638–7644.

[126] Berenov, A.; Atkinson, A.; Kilner, J.; Bucher, E.; Sitte, W. Oxygen tracer diffusion and surface exchange kinetics in $La_{0.6}Sr_{0.4}CoO_{3-\delta}$. *Solid State Ionics* **2010**, *181*, 819–826.

[127] Nakamura, T.; Yashiro, K.; Sato, K.; Mizusaki, J. Oxygen nonstoichiometry and defect equilibrium in $La_{2-x}Sr_xNiO_{4+\delta}$. *Solid State Ionics* **2009**, *180*, 368–376.

List of Figures

Danksagung

Die letzten Zeilen meiner Dissertation zu verfassen, fühlt sich zugegebenermaßen schon sehr surreal an. Nach drei Jahren Doktorat, vier Jahren im Forschungsbereich Technische Elektrochemie und insgesamt achteinhalb Jahren an der TU Wien endet nun meine Reise an dieser Universität. Dabei empfinde ich neben der Freude über den baldigen Abschluss auch eine gewisse Wehmut, war es doch eine sehr spannende, lehrreiche, mitunter herausfordernde, aber vor allem eine wunderschöne Reise, die ich niemals vergessen werde. Dass es überhaupt zu diesem Moment gekommen ist, verdanke ich jenen Menschen, die mich in dieser Zeit begleitet und unterstützt haben. Ihnen möchte ich die folgenden Zeilen widmen.

Zuallererst möchte ich hier meine Betreuer nennen. Danke Jürgen, für die Möglichkeit in dieser tollen Forschungsgruppe den Weg von einer Projektarbeit, über die Diplomarbeit bis hin zur Dissertation gehen zu dürfen. Ich bin euch, Jürgen und Markus, sehr dankbar für eure Unterstützung in den letzten drei Jahren! Danke, für die vielen anregenden fachlichen Diskussionen, für eure stets offenen Ohren und Türen, für euer Vertrauen, eure ermutigenden Worte und für die Freiheit vielen eigenen Ideen nachgehen zu können! Hier möchte ich auch den Betreuer meiner Diplomarbeit, Alex S., nennen. Danke Alex, für deine Einführung in die Welt der Festkörperionik, für das oftmalige gemeinsame Diskutieren und für eine sehr spannende gemeinsame Woche am Synchrotron in Grenoble. Du warst immer ein hervorragender Mentor für mich! Euch verdanke ich es, dass ich ein wissenschaftliches Zuhause gefunden habe.

Besonders bedanken möchte ich mich außerdem bei dir, Matthäus, für die AFM-Bilder und die Unterstützung bei XRD-Messungen – aber auch für eine sehr lustige Woche in Berlin mit Prof. Lasagne und dem Conferencer! Du hast gemeinsam mit dem Alex V. und dem Harald auch sehr viel dazu beigetragen, dass ich mich von Anfang an in der Forschungsgruppe gut aufgenommen und wohl gefühlt habe – danke euch dafür! Ich möchte mich auch bei euch beiden bedanken, Christin und Andi, für die AFM-, XRD- bzw. TEM-Messungen – vor allem aber auch für die vielen gemeinsamen Mittagessen und den entspannten, anregenden und manchmal auch ausschweifenden Gesprächen währenddessen. Außerdem danke ich euch beiden für eine unvergessliche Zeit in Boston auf der SSI! Hier möchte ich auch den besten aller Reiseleiter nicht unerwähnt lassen – danke Christoph für die Zeit in Boston, viele interessante sowie auch erheiternde Gespräche mit den heißesten News am Institut und natürlich dafür, mit dir das Gasversorgungsteam bilden zu dürfen! Danke Joseph für deinen Humor und deine Unbekümmertheit, die immer wieder für Auflockerung sorgen. Danke Tobi, für deine Unterstützung beim TGA-Aufbau und allen möglichen Basteleien! Bedanken möchte ich mich auch bei Andi N. und Christopher für die XPS bzw. ICP-MS-Messungen! Danke Andi N. und Alex O. für viele anregende fachliche und nicht-fachliche Gespräche! Vielen Dank auch an meine Bürokollegen, Philip und Max, für das hervorragende Büroklima und willkommene Ablenkungen zwischendurch! Ich möchte mich bei allen Personen aus der Forschungsgruppe und generell bei allen die im Erdgeschoß „BC" sesshaft sind für das tolle und freundliche Arbeitsklima bedanken. Das Arbeiten mit euch hat mir viel Freude bereitet und ich werde diese Zeit immer in guter Erinnerung behalten!

Ein großer Dank gilt auch all meinen Freunden für die Unterstützung und erholsame Ablenkung in all den Jahren! Besonders erwähnen möchte ich hier die „Experten für eh ois" – danke euch für unvergessliche Treffen, Ausflüge und Urlaube!

Der größte Dank gebührt meiner Familie, speziell meinen Eltern, Margit und Erwin, die mir es ermöglich haben zu studieren. Danke euch für die Unterstützung und den Rückhalt in all den Jahren! Besonders bedanken möchte ich mich auch bei meinem Bruder und bestem Freund, Stefan, auf den ich immer zählen kann! Danke für die vielen unvergesslichen Erlebnisse, das gemeinsame Blödeln und die vielen Gespräche – besonders in stressigen Zeiten war all das unverzichtbar! Zu guter Letzt, danke ich dir, Claudia, für deine nie endende Unterstützung, dein Aufmuntern und Ermutigen und dein Verständnis, wenn ich an so manchem Abend wieder einmal „noch kurz nach hinten ins Büro" musste. Danke einfach für alles in den letzten Jahren! Ich kann nicht in Worte fassen wie viel Dankbarkeit und Glück ich empfinde, euch in meinem Leben zu haben!